Spring 2015

A three constituent mixture theory model of cutaneous and subcutaneous tissue in the context of neonatal pressure ulcer etiology and prevention

Anne Dye Zakrajsek
Purdue University

Graduate School Form 30
Updated 1/15/2015

PURDUE UNIVERSITY
GRADUATE SCHOOL
Thesis/Dissertation Acceptance

This is to certify that the thesis/dissertation prepared

By Anne D. Zakrajsek

Entitled

A THREE CONSTITUENT MIXTURE THEORY MODEL OF CUTANEOUS AND SUBCUTANEOUS TISSUE IN THE CONTEXT OF NEONATAL PRESSURE ULCER ETIOLOGY AND PREVENTION

For the degree of Doctor of Philosophy

Is approved by the final examining committee:

Dr. Eric Nauman
Chair

Dr. Charles Krousgrill

Dr. Darryl Dickerson

Dr. Lynetta Freeman

To the best of my knowledge and as understood by the student in the Thesis/Dissertation Agreement, Publication Delay, and Certification Disclaimer (Graduate School Form 32), this thesis/dissertation adheres to the provisions of Purdue University's "Policy of Integrity in Research" and the use of copyright material.

Approved by Major Professor(s): Dr. Eric Nauman

Approved by: Dr. Ganesh Subbarayan 4/14/2015

Head of the Departmental Graduate Program Date

A THREE CONSTITUENT MIXTURE THEORY MODEL OF CUTANEOUS AND SUBCUTANEOUS TISSUE IN THE CONTEXT OF NEONATAL PRESSURE ULCER ETIOLOGY AND PREVENTION

A Dissertation

Submitted to the Faculty

of

Purdue University

by

Anne D. Zakrajsek

In Partial Fulfillment of the

Requirements for the Degree

of

Doctor of Philosophy

May 2015

Purdue University

West Lafayette, Indiana

To James, Marilynn, Shamrock and those yet to join our family. You can do anything you set your mind to do! I love you, Mom!

ACKNOWLEDGEMENTS

I would first like to thank my advisor Dr. Eric Nauman for his continued support, guidance, and encouragement throughout my undergraduate and graduate studies. It seems like just yesterday that it was Spring 2007 semester, and I was a Freshman in your SVAT EPICS section. Eight years, three lab spaces, two degrees, one patent, one marriage, two kids, and countless "good stuffs" later, and I'm finally flying the H.I.R.R.T. lab coop. Needless to say, I am very, very grateful to have you as my advisor. I would also like to thank my committee members, Dr. Charles Krousgrill, Dr. Lynetta Freeman, and Dr. Darryl Dickerson for your support in this process.

Wait...Dr. Darryl Dickerson? Who is he? We were both students in the lab not long ago, so I feel like I have to doubly acknowledge you as a lab member as well. Thank you for your patiently delivered advice and encouragement throughout the years – your listening ear has saved me from many a panic attack. Thank you also for leaving extra button down shirts, suit jackets, red beans and rice, contracts, and porcine bone in your desk for me to find when I inherited it. I still believe that my laptop is ridden with bone fragments. Finally, thank you for your leadership with Adapt-IF Technologies, a vision that we share. I'm very excited to see what the future holds for the non-profit.

I would also like to thank former H.I.R.R.T. lab members for being a great support system throughout this process. Thank you Mary Schuff, Kent Butz, and

especially Monica Susilo. Monica, your mentorship throughout my graduate studies has been imperative to my success. You have taught me so much about the process of research from derivation to trouble shooting to analysis. I feel so much more confident in my capabilities because of your mentorship, and for that I am very grateful. You are going to be a phenomenal faculty member, and your students are going to be so lucky to have you as a teacher!

Last but not least, I would like to thank my husband, Andrew, for putting up with me these past few months. I could not have accomplished this without you by my side. Thanks for making dinners, doing laundry, cleaning, grocery shopping, getting up early with James, and generally picking up my slack. You are truly selfless. Thank you for always being my biggest supporter! We did it!

TABLE OF CONTENTS

` Page

Page

Page

LIST OF TABLES

Table Page

LIST OF FIGURES

Figure Page

Figure Page

Figure Page

Figure Page

Figure Page

Figure Page

ABSTRACT

Zakrajsek, Anne D. Ph.D., Purdue University, May 2015. A Three Constituent Mixture Theory Model of Cutaneous and Subcutaneous Tissue in the Context of Neonatal Pressure Ulcer Etiology and Prevention. Major Professor: Eric Nauman, School of Mechanical Engineering.

Localized ischemia, impaired interstitial fluid flow, and sustained mechanical loading of cells have all been hypothesized as mechanisms of pressure ulcer (PrU) etiology. Time-varying loading has experimentally been shown to increase fluid flow in human skin *in vivo*. Towards the design of prophylactic protocols and treatment modalities for PrU management there is a need for an analytical model to investigate the local fluid flow characteristics of skin tissue under time-varying loading. In this study, a triphasic mixture theory model with constituents of extracellular matrix, interstitial fluid, and blood was calibrated and validated and used to investigate stress and fluid velocity under quasi-static and time-varying loading conditions, respectively. Four input strain profiles were considered, including uniform, geometric circular segment, Gaussian, and Hertz-type strain profiles. Calibrated bulk and shear modulus (κ=227.7kPa, μ=1.04kPa) were on the same order of magnitude as literature. Fluid velocities were investigated for apparent strain amplitudes of 100-700$\mu\varepsilon$ and frequencies of 10-80Hz. At the lowest amplitude and frequency, interstitial fluid velocities were on the same order of magnitude as literature values, $1\frac{\mu m}{s}$ and $1\frac{mm}{s}$, respectively. Interstitial fluid and blood velocity both

experienced significant increases with increasing amplitude and frequency. The study demonstrated the ability to analytically predict quasi-static stress profiles as well as predict fluid velocity increases in cyclically loaded soft tissues by employing quasi-static mechanics and mixture theory models. Consequently, this study builds a strong foundation for use in the development of vibrational support surfaces for use in prophylactic protocols and adjunctive treatment modalities for PrU management.

CHAPTER 1. INTRODUCTION

According to recent literature disseminated by the National Pressure Ulcer Advisory Panel (NPUAP), an independent not-for-profit professional organization, 1 to 3 million people develop pressure ulcers (PrUs), also known as pressure sores, bed sores, or decubitus ulcers, each year in the United States [1]. The NPUAP defines a PrU as "localized injury to the skin and/or underlying tissue usually over a bony prominence as a result of pressure, or pressure in combination with shear," ranging in severity from minor (Stage I) to severe (Stage IV) [2]. PrUs appear superficially on the skin or develop at the bone-tissue interface manifesting as deep tissue injury (DTI) [3,4]. PrUs may occur in any person experiencing prolonged mechanical loading, but are commonly associated with those who are bedridden, wheelchair bound, or wearing a prosthetic, orthotic, or other medical device [3].

Statistics regarding PrUs distinguish between *incidence* and *prevalence*. NPUAP defines *incidence*, which represents nosocomial PrUs, as the number of persons who develop PrUs within a given time period [5]. *Prevalence* is defined by NPUAP as 'a cross-sectional count of the number of cases at a specific point in time, or the number of persons with PrUs who exist in a patient population at a given point in time.' Reports

from the Agency for Healthcare Research and Quality (AHRQ) estimate a PrU *incidence* of .4-38% in acute care, 2.2-23.9% in long term care, and 0-17% in in-home care settings [6]. Likewise, PrU *prevalence* estimates report 10-18% in acute care, 2.3-28% in long term care, and 0-29% in in-home care settings [5]. Estimates vary widely for many reasons, including miscalculation of prevalence versus incidence statistics, failure to consistently stage PrUs, inaccurate assessment and documentation of PrU upon admission, and financial disincentives for hospital-acquired conditions and readmissions [7-9].

PrUs cost an estimated $8.5-11 billion dollars per year in medical care [7,10]. More than 90% of PrUs are considered medical errors which amount to an estimated $3.3-3.8 billion dollars per year ranking them consistently as both one of the most common and most costly medical errors [11]. These figures have become increasingly important, as 2008 changes to the Centers for Medicare and Medicaid Services (CMS) regulations classified PrUs as a "never event" which means that treatment prescribed for hospital-acquired pressure ulcers (HAPUs) is no longer reimbursed [12].

Beyond the financial ramifications, PrUs carry great physical, emotional, and psychological burden for both patients and their families. PrUs lead to higher healthcare costs, longer hospital stays, limited activities, increased morbidity and co-morbidities, increased mortality, emotional distress, and a decreased overall health-related quality of life (HRQL) [13-15]. Adjunctive therapies often required for late stage PrU treatment,

such as pulsed electromagnetic treatment, electrical stimulation, and negative pressure wound therapy, further detract from HRQL [14,16,17].

Several factors are hypothesized to contribute to PrU etiology, the relative importance of each is not yet well understood [2]. At a fundamental level, sustained pressure is believed to be a primary mechanism of PrU etiology [3,18,19]. Other common hypotheses of PrU etiology include ischemia, hyperemia, cyclic ischemia-reperfusion injury, lymphatic deficiencies, friction, shear, malnutrition, and neuropathy [3,4].

Treatment modalities for PrUs range from topical to adjunctive therapies, and in severe cases, surgical debridement and reconstruction [20,21]. Treatment modalities include regimented repositioning, wound cleansers, vitamin and mineral supplementation, enteral (delivered through a feeding tube) and parenteral (delivered intravenously) feeding, ultrasound therapy, specialized support surfaces, and negative pressure suction therapy [1,21-25]. Recent studies show that one modality has not proven superior to the others and thus further research is necessary to mitigate the effects of mechanically-induced PrU formation [20].

Populations at risk for PrU development are those that withstand prolonged periods of mechanical loading, such as those who are in wheelchairs, bedridden, or wearing a prosthetic, orthotic, or other medical device. These situations often result from risk factors and co-morbidities, such as acute injury, functional limitations, perfusion deficiencies (diabetes, vascular disease, etc.), moisture status (incontinence), nutritional

deficiencies, and age [26,27]. An estimated 80% of all persons with spinal cord injuries (SCIs) will develop a PrU within their lifetime, while 30% of those with SCIs have a PrU at any given time [28-30]. More than 70% of all PrUs occur in those age 70 or greater [31]. Furthermore, greater than 90% of adult PrUs occur over bony prominences, including the sacrum, heels, and elbows [32,33].

Once thought to be insignificant among the pediatric population, recent studies have uncovered incidence rates ranging from 0.8% to 53% [33-37]. A 2003 national survey reported a 4% average prevalence rate for stage III and stage IV PrUs in pediatric hospitals [38]. As with adult PrUs, accurate statistics are increasingly important as pediatric HAPUs are no longer reimbursed by Medicaid as of July 2012 [39].

Pediatric PrUs result in prolonged hospital stays, increased risk for infection, and emotional distress for both the patient and families. Distinctly different than adult PrUs, a large proportion of pediatric PrUs are medical device related. Multiple studies have reported that 50% to 69% of pediatric intensive care unit (PICU) PrUs are device-related [35,39]. Neonatal intensive care unit (NICU) PrUs, although not widely documented, have reported that up to 90% of PrUs are medical device related [39]. Common medical devices associated with PrUs are noninvasive positive pressure ventilation (NIPPV) facemasks, tracheostomy tubes and ties, pulse oximeters, and extracorporeal membrane oxygenation (ECMO) cannulas [39].

Towards the design or redesign of device(s) that prevent and treat PrUs, specifically pediatric PrUs, this research attempts to better understand the etiology of PrUs overall. With a greater understanding of the primary factors in PrU development, design parameters for prevention and treatment devices can be properly developed. Therefore, the long-term goal of this research is to uncover the primary mechanisms of PrU etiology with an emphasis on fluid flow and fluid flow maintenance in vulnerable and compromised tissue. As a step towards uncovering the complex etiology of PrUs, a biofidelic model of cutaneous and subcutaneous tissue will be developed and implemented to investigate stress and fluid flow mechanics under clinical boundary conditions. As such, the following specific aims will be addressed.

1. Calibrate and validate a mixture theory based analytical model of skin tissue *in vivo*. Stress-strain relationships for *in vivo* human skin tissue were acquired from literature and used to calibrate three different models for the solid constituent: incompressible linear elastic (ILE), incompressible Neo-Hookean (INH), compressible Neo-Hookean with uniform strain input (CNH-U), and compressible Neo-Hookean with Hertzian-type strain input (CNH-Hertz). Model parameters were estimated by minimizing the root mean squared error (RMSE). The CNH-Hertz model proved to have the best predictive capabilities, and therefore, model parameters were taken to be those of the CNH-Hertz model calibration.
2. Predict tissue stress state under varying clinically relevant scenarios. The compressible, Neo-Hookean model was further validated by examining the predictive capabilities of the model with varying strain input. Two different Hertzian strain input forms were considered, namely elastic contact between a

sphere and a half-space and elastic contact between a cylinder lying on a half-space. The form of the strain inputs were selected to simulate the occiput of a neonate in supine lying position and an oxygen cannula lying on the tissue surface of a neonate.

3. To develop a time dependent mixture theory based analytical model of skin tissue *in vivo* to investigate the effect of vibration on the maintenance of fluid transport.

   A three constituent mixture theory was developed with constituents of solid extracellular matrix (ECM), interstitial fluid, and blood. Using a compressible, Neo-hookean model previously calibrated and validated for the solid constituent, the interstitial fluid and blood velocities were predicted for various time-varying loading scenarios. The apparent strain magnitude and frequency were varied from 100-700με and 10-80 Hz, respectively.

CHAPTER 2. BACKGROUND

2.1 Anatomy and Physiology of Skin

Skin is the largest organ of the integumentary system and the body. It accounts for approximately 15% of total adult body weight. The skin has many important functions, including providing protection from physical, chemical, and biological aggressors, excretion of waste products, temperature regulation, and vitamin D synthesis and storage. Skin is mainly collagen and elastin in a gel continuum of mucopolysaccharides with a principle mass of collagen [40]. The skin is divided into three layers called (from superior to inferior) the epidermis, dermis, and hypodermis (Figure 1) [41].

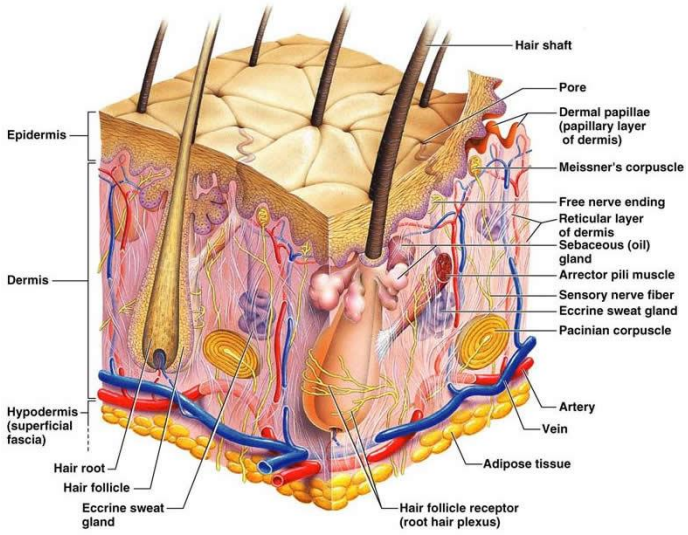

Figure 1. An isometric view of a cross section of human skin tissue depicts the three prominent layers (from superior to inferior), including the epidermis, dermis, and hypodermis [42].

The epidermis has an average thickness of 100 μm and is a non-vascular tissue composed mainly of keratinocytes in several layers, namely (from inferior to superior) the basal layer, stratum spinosum, granular layer, stratum lucidum (in the palmoplantar region only), and stratum corneum (SC). The epidermis contains two structure units, the sweat glands and hair follicles [41].

The stratum corneum (Figure 2) is well established as the least permeable layer of skin, creating a barrier to transepidermal water lass (TEWL) and to percutaneous absorption [43-45]. As such, the primary role of the SC is barrier function. The SC is typically 10-20μm thick with a structural appearance of bricks (corneocyte proteins) and mortar (lamellar lipids) [45,46].

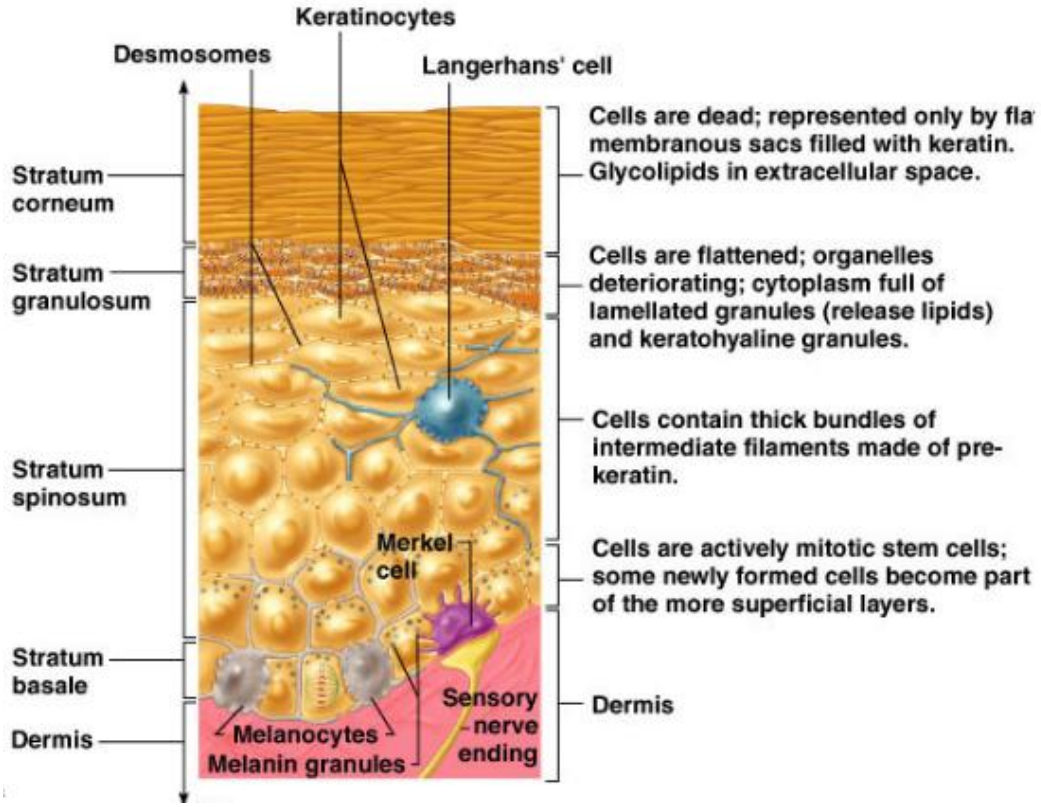

Figure 2. The epidermis is a complex tissue layer and is broken down into sublayers, including the stratum corneum, stratum granulosum, stratum spinosum, and stratum basale. The dermal epidermal junction connects the epidermal and dermal layers [42].

Between the epidermis and dermis lies the dermal-epidermal junction (DEJ). The DEJ is composed of basal keratinocytes and dermal fibroblasts. Not only does the DEJ provide mechanical support for the adhesion of the epidermis to the dermis, it regulates transport between the two layers. This is critical for necessary immunologic and inflammatory processes required for wound healing [41].

The dermis is composed of cells (fibroblasts, dermal dendrocytes, fibrous molecules, and a ground substance (glycoproteins and proteoglycans), with thickness varying greatly with anatomic location. It is subdivided into the papillary (superficial) and reticular (deep) layers and therefore its structure is inhomogeneous depending on depth. The papillary

layer forms finger-like projections that lock into the epidermis creating adhesion between the layers. The majority of dermal fibers are composed of types I and III interstitial collagen arranged in loose papillary bundles and thick reticular bundles. The dermis contains cutaneous vessels from the arterial, venous, and lymphatic systems, and afferent (touch, pressure, vibration, etc.) and efferent (sweat) innervation [41].

The hypodermis is the deepest part of the skin composed of adipose tissue (adipocytes) with thickness varying greatly with anatomic location, age, and gender. Primary roles of the hypodermis are temperature regulation, insulation, and nutritional storage. Structure components contained in the hypodermis include the deepest part of sweat glands, vessels, and nerves [41].

2.2 Mechanical Properties of Skin

The elastic and viscoelastic mechanical properties of skin have been studied *in vivo* and *in vitro* in animals and humans under mulitple loading conditions, such as uniaxial compression, uniaxial and biaxial tension, and torsion using various methods, such as mechanical experiments, ultrasound, and MRI [47-57]. Despite numerous studies examining skin properties, there still exists a wide range of values, as the properties of skin are largely dependent on age, gender, anatomical site, microclimate and overall tissue health (hydration, nutrition, disease, etc.) [58]. Both aggregate (Table 1.) and individual tissue layer (Table 2.) properties are summarized in order to understand the depth dependent characteristics of skin.

Table 1. Mechanical properties of aggregate human skin tissue.

Young's Modulus (kPa)	Shear Modulus (kPa)	Reference
8.5 ± 1.74	3.3 ± 0.46	[49]
8.3 ± 2. 1	2.8 ± 0.8	[49]
4.36 ± 1.05(2.8-5.96)	-	[48]
8.82 ± 3.77 (6.04-13.74)	-	[48]
28.6±4	-	[55]
24±3.8	-	[55]
13.7±5.3	-	[55]
11.2±2.8	-	[55]
18± 4	-	[50]
8.8	-	[49]
5.2	-	[49]
3.44± 0.8	-	[53]
1.46± 0.26	-	[53]

Table 2. Mechanical properties of the stratum corneum (wet and dry), viable epidermis, dermis, and hypodermis.

	Young's Modulus (kPa)	Shear Modulus (kPa)	Reference(s)
Stratum Corneum	500 (3.5-1000)	-	[50,53,54]
	0.04-10E6	30 (dry)	[53]
	30 (10-50)	-	[50,53,54]
	6-10E4	10 (wet)	[53]
Viable Epidermis	-	30 (dry)	[53]
	-	10 (wet)	[53]
	1.5	-	[50,52,53]
Dermis	0.02 (8-35E-3)	-	[49,50,52,56]
Hypodermis	2.00E-03	-	[56]

2.3 Classification of Pressure Ulcers

At the most basic level, PrUs are a form of tissue breakdown as a result of applied pressure, frictional force, and/or shear. While the exact etiology of PrUs is not well understood, various mechanisms related to applied mechanical loading have been hypothesized, including tissue hydrostatic pressure, impaired microcirculation, hypoxia, reperfusion injury compromised interstitial transport, and impeded lymphatic return [59-67].

NPUAP classifies PrUs into four stages and two categories. Stages I-IV classify superficial tissue injury. The remaining categories distinguish unstageable/unclassified PrUs and DTI [2]. It is important to note that PrUs occurring on mucosal membranes, such as device-related PrUs caused by endotrachial tubes or oxygen cannulas, cannot be classified using NPUAP's system due to histological differences in the tissues.

2.3.1 Stage I PrUs

Stage I PrUs are identified by non-blanchable erythema of otherwise intact skin. The area is generally different than the adjacent tissues in color, feel, and temperature, and may be painful. Stage I PrUs have the highest incidence and prevalence rates, with 55-61% of all hospital acquired PrUs being Stage I PrUs and an overall prevalence of approximately 40% [68]. The incremental cost of Stage II PrUs is approximately $2000 [69].

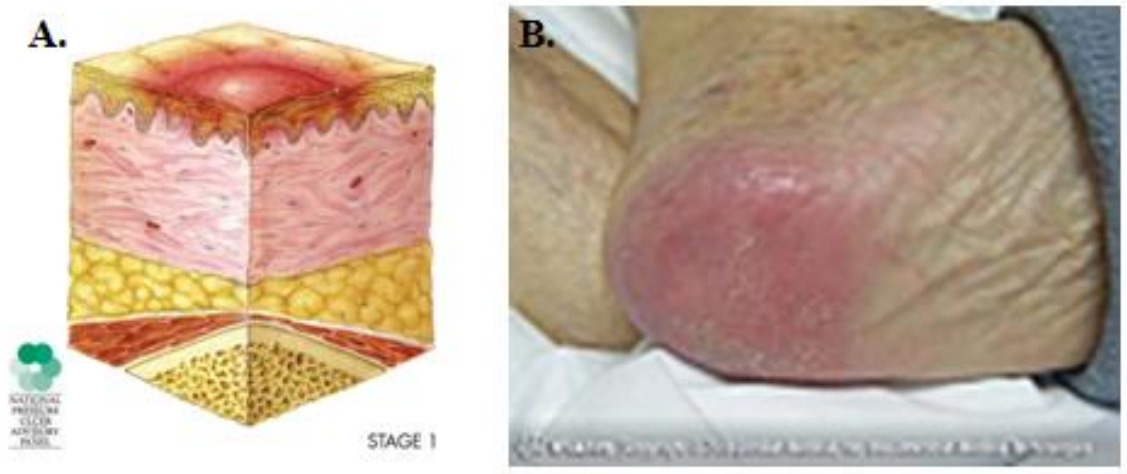

Figure 3. A.) Stage I PrU characterized by non-blanchable erythema. The affected tissue may be painful and present in different color, feel, and temperature than adjacent tissue B.) Stage I heel PrU. Images courtesy of NPUAP.

2.3.2 Stage II PrUs

Stage II PrUs are characterized by partial thickness loss of dermis. This may present as a shallow, red-pink open ulcer or an intact or ruptured serum or sero-sanguinous filled blister. Stage II PrUs have the second highest incidence and prevalence rates, with 34-37% of all hospital acquired PrUs being Stage II PrUs and an overall prevalence of 34-37% [68]. The incremental cost of Stage II PrUs is approximately $3,000-$10,000 [69].

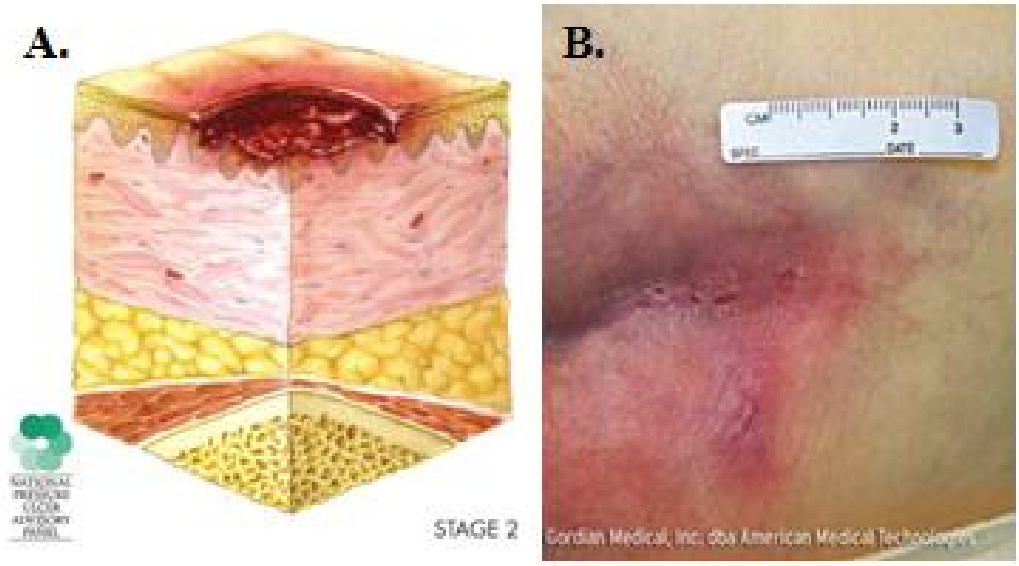

Figure 4. A.) Stage II PrU characterized by partial thickness loss of dermis. The affected tissue may present as a shallow red-pink open ulcer or an intact or ruptured serum or sero-sanguinous filled blister. B.) Sacrococcygeal Stage II PrU. Images courtesy of NPUAP.

2.3.3 Stage III PrUs

Stage III PrUs are characterized by full thickness skin loss with exposed adipose tissue only. Bone, tendon, and muscle should not be exposed in a Stage III PrU. Slough may or may not be present. Stage III PrUs are more common in critical care scenarios, such as in intensive care units, where Stage III incidence rates of up to 30% have been reported [70]. The incremental cost of Stage III PrUs is approximately $5,900-$14,840 [69].

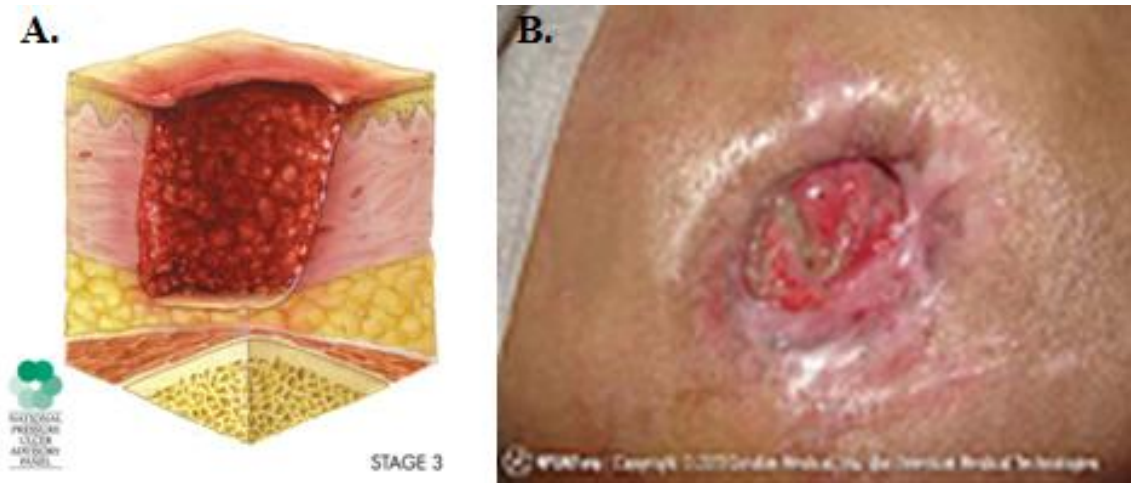

Figure 5. A.) Stage III PrU characterized by full thickness skin loss. Tissue breakdown of the epidermal and dermal layers leaves the adipose tissue exposed. B.) Stage III hip PrU. Images courtesy of NPUAP.

2.3.4 Stage IV PrUs

Stage IV PrUs are characterized by full thickness tissue loss with exposed, palpable or visible bone, tendon, and muscle. Slough may or may not be present. Incidence and prevalence rates for Stage IV PrUs are not accessible in literature, however, the incremental cost of Stage IV PrUs ranges from $18,730-$21,410 [69].

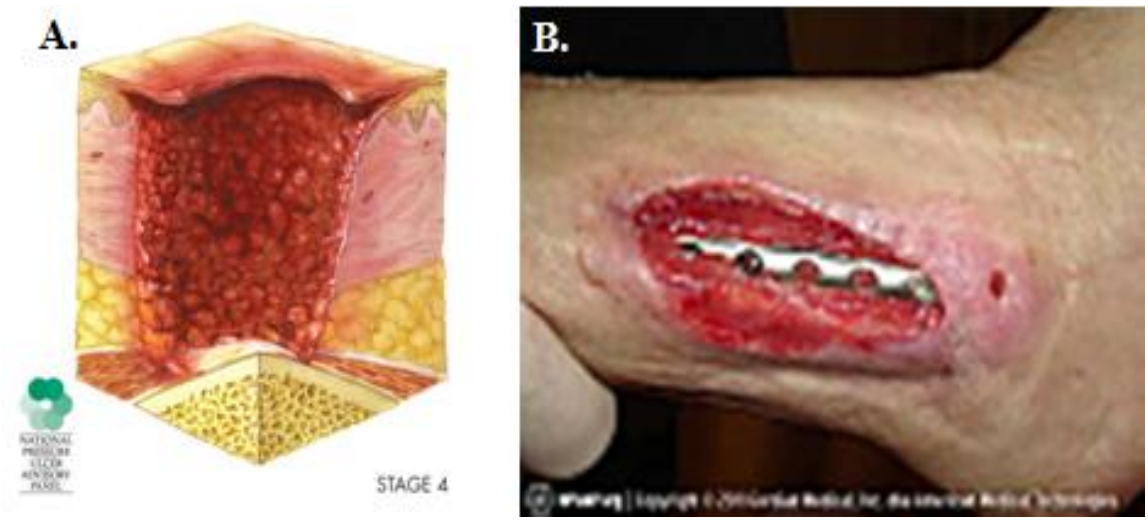

Figure 6. A.) Stage IV PrU characterized by full thickness tissue loss with bone, tendon, or muscle exposure. B.) Stage IV ankle PrU with exposed metal fixation device. Image courtesy of NPUAP.

2.3.5 Unstageable/Unclassified

Unstageable/Unclassified PrUs are characterized by full thickness tissue loss for which the depth of the PrU is unknown due to the presence of slough and/or eschar. The wounds are likely Stage III or IV PrUs and will be distinguished as such once enough slough and/or eschar is removed via debriedment.

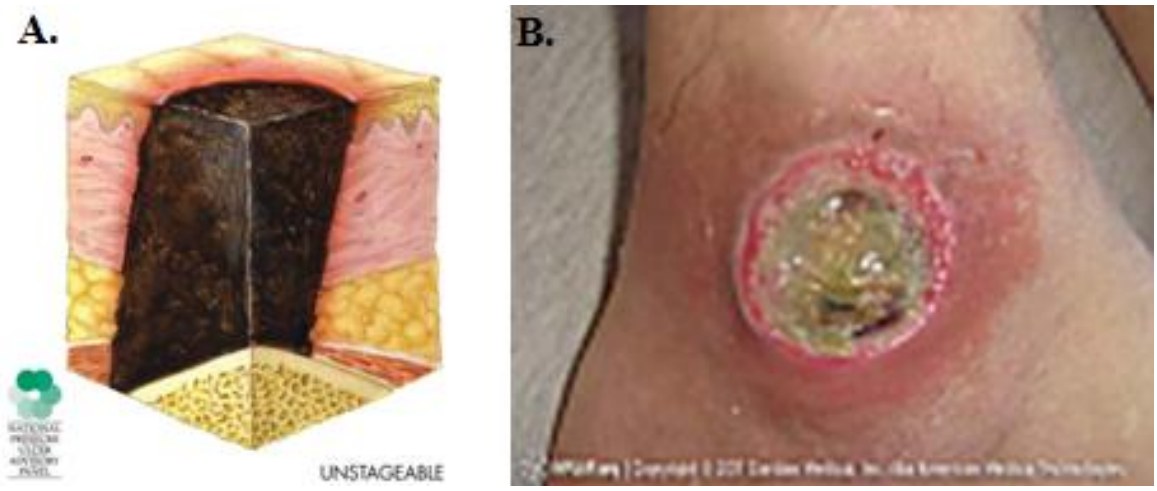

Figure 7. A.) Unstageable/Unclassified PrU characterized by full thickness tissue loss the depth of which is obstructed by slough and/or eschar. B.) Unstageable/Unclassified ankle PrU. Image courtesy of NPUAP.

2.3.6 Suspected DTI

Suspected DTI is characterized by a localized area of purple, maroon discolored skin or a sanguineous blister. The area is generally different than the adjacent tissues in color, feel, and temperature, and may be painful.

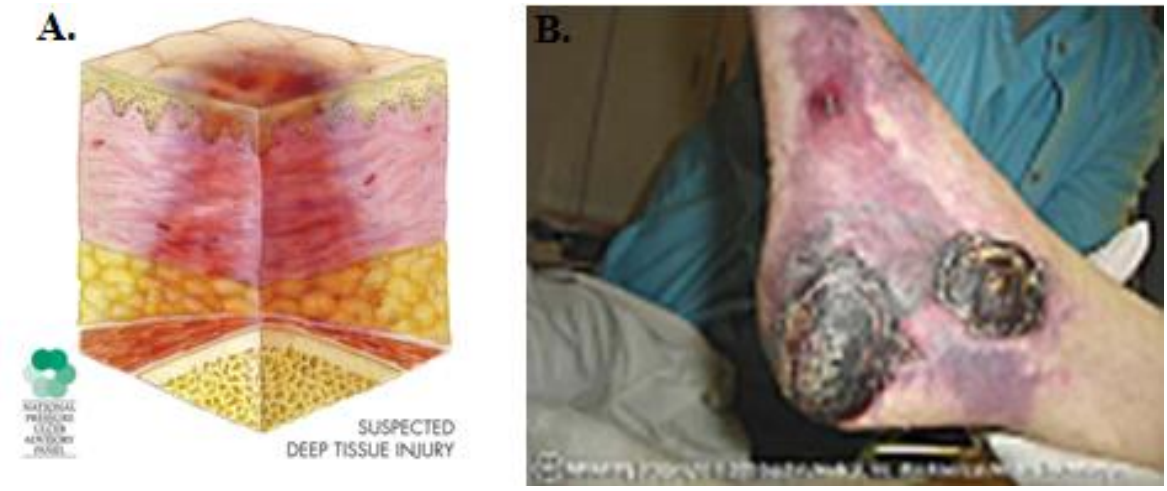

Figure 8. A.) Suspected DTI is characterized by a localized area of purple, maroon discolored skin or a sanguineous blister. B.) Stage IV PrU in combination with DTI located on the heel and ankle. Image courtesy of NPUAP.

2.4 Prophylactic Treatment

Prophylactic treatment measures are non-pharmacological treatments that typically target populations with impaired mobility, impaired nutrition, or impaired skin health [10].

2.4.1 Impaired Mobility

The most basic prophylactic treatment for impaired mobility is the use of a specialized support surface. Support surfaces are defined by NPUAP as

> "A specialized device for pressure redistribution designed for management of tissue loads, micro-climate, and/or other therapeutic functions (i.e. any mattresses, integrated bed system, mattress replacement, overlay, or seat cushion, or seat cushion overlay)" [71].

There are seven categories of support surfaces, including reactive (alters load distribution with a change in pressure), active (alters load distribution with or without change in pressure), integrated bed system, non-powered, powered, overlay, and mattress. Any such support surfaces may be composed of one of more of the following components: air, cell/bladder, viscoelastic foam, elastic foam, closed cell foam, open cell foam, gel, pad, viscous fluid, elastomer, solid, or water. Support surfaces may have special features, such as air fluidization (silicone-coated beads that liquefy when air passes through), alternating pressure (cyclic loading and unloading), lateral rotation (rotation about longitudinal axis), low air loss (provides air flow to manage heat and humidity), zone redistribution, or multi-zoned surface [10,71]. Generally speaking, dynamic (powered) support surfaces

are more expensive than static support surfaces (overlays), with air-fluidized beds being the most expensive [10].

Several studies have analyzed the effectiveness of support surfaces. When used in operating theaters, visco-elastic foam mattresses were shown to decrease the incidence of postoperative PrUs [72]. Other studies have demonstrated specialized foam and sheep skin to be superior in PrU incidence reduction than standard hospital mattresses in multiple settings [73-81]. Further studies have shown that gel in combination with foam overlays is superior to plain foam itself [79,82].

The large majority (79%) of studies comparing static and dynamic support surfaces have found no difference in PrU incidence reduction between the two [10,83]. However, both static and dynamic support surfaces are superior to standard surfaces [84].

Aside from support surfaces, repositioning at 2 hour intervals (Q2H) is a standard protocol for the prophylactic treatment of PrUs that was initiated in the 1960s [85,86] and validated by the classic pressure-time threshold curve developed by Reswick and Rogers [18] (Figure 9). A Q2H turning regime is both costly to the nursing staff and the patients, as the nursing staff spends approximately 15 days out of 365 patient-days per year on turning and the patients are disturbed every 2 hours including throughout the night [87]. Recent studies show that repositioning at 4 hour intervals in combination with a visco-elastic foam overlay may be more effective [87,88].

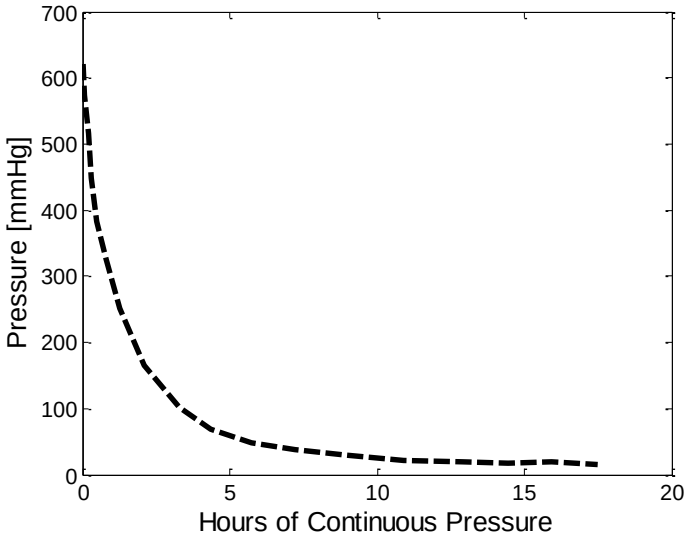

Figure 9. The classically referenced pressure-time threshold curve developed by Reswick and Rogers [18] provides guidelines for the allowable pressure versus time of application for tissue under a bony prominence. Pressures that fall below the curve are acceptable and above the curve are unacceptable.

2.4.2 Impaired Nutrition

The role of nutrition in the prevention of PrUs has been assumed, but is not supported with strong evidence [10]. One study compared patients over the age of 65 who ate a regular diet to those who supplemented a regular diet with two nutritional supplements per day. The control group was approximately 1.5 times more likely to get a pressure ulcer [89]. Other studies have found that the incidence and severity of PrUs increases with poor nutrition that results in decreased calorie intake, dehydration, and low serum albumin levels [89-91]. These factors all contribute to a lower tolerance of skin to mechanical loading [10].

Serum albumin levels are roughly indicative of the amount of protein available in blood for healing purposes. Several studies suggest a correlation between protein-deficit nutrition (protein energy malnutrition) and increased incidence of PrUs [92-94]. In order

to prevent low serum albumin levels, patients at a high risk for PrUs with impaired nutrition are put on protein-rich nutritional supplements. The supplements may be enteral or parenteral, the most effective administration of which has yet to be determined [95].

Although evidence is lacking, nutrition is generally believed to play a critical role in pressure ulcer prevention, as most PrU risk analysis tools include nutrition as a risk factor [96-98]. Furthermore, NPUAP as well as the European Pressure Ulcer Advisory Panel (EPUAP) also consider nutrition as a risk factor for PrU in their guidelines [99,100].

2.4.3 Impaired Skin Health

Populations with impaired skin health are at an obvious risk for PrUs. Topical treatments, such as lotions and specialty lotions, are the primary prophylactic intervention. Topical agents reduce the coefficient of friction between the skin tissue and support surface, prevent hyperproliferative skin growth, and maintain skin hydration [10,101]. Studies have shown that essential fatty acids (EFAs), such as linoleic and linolenic acids, are the most effective topical agents for PrU prevention [102,103].

2.5 Acute/Chronic Treatment

Acute/chronic treatment of PrUs includes managing the primary and secondary contributing factors, wound care (pharmacological, topical treatments), and adjunctive therapies typically in that order [20,104]. Management of primary and secondary contributing factors is likely the most important treatment and should therefore receive the most attention [104].

2.5.1 Managing Contributing Factors

Managing the contributing factors of PrU formation begins with repositioning as well as the same support surfaces used for PrU prevention, including specialty foam overlays, powered and unpowered mattresses, low air loss mattresses, alternating pressure mattresses, fluid mattress overlays, and any combinations of such support surfaces [20].

Conflicting studies suggest that more research is necessary to elucidate whether powered support surfaces are superior to unpowered support surfaces for repositioning purposes in the treatment of PrUs [105-110]. Similarly, conflicting evidence exists for powered mattresses as well. While some studies find no difference between PrU healing between powered mattresses, Allman et al. found that air fluidized mattresses decreased PrU surface area while alternating pressure mattresses increased PrU surface area [106,111,112].

Nutritional supplementation is also considered both a preventative measure and a treatment for PrUs. Nutritional treatment may include protein, vitamin C, arginine, zinc, and antioxidant supplementation, all of which help to facilitate healthy tissue growth [20,113]. Most studies have found that protein supplementation increases PrU healing rates [20,114]. Conflicting evidence suggest additional research is necessary to understand the role of vitamin C in PrU healing rates [115,116]. Arginine, a dietary conditionally essential amino acid that functions as a substrate for protein synthesis, collagen deposition, and cell proliferation among other things, has been shown to significantly enhance collagen production and increase wound healing [113,117-120].

Zinc and antioxidant-rich supplements have also shown to mediate wound healing [20,113,120].

2.5.2 Wound Care

Wound care involves applying a topical agent and/or dressing the wound. There are many options for wound dressings that can be categorized as debriding, hydrating, absorbent, and antimicrobial products. The majority of such wound dressings are basic emollients, hydrogels (hydrophilic polymer network), and hydrocolloids (cross linked adhesive matrix containing gelatin, pectin, and other polymers).

When comparing collagenase versus fibrinolysin or deoxyribonuclease, collagenase versus hydrocolloid and/or alginate and phenytoin solution versus normal saline, no difference in wound healing was found [20]. Mean wound surface area reduction per week was found to be higher in wounds treated with calcium alginate [121]. And finally, compared to lanolin or pertrolatum, oxyquinoline facilitated wound healing [122].

Topical agents for PrU treatment can be categorized as wound environment modulators, skin substitutes, platelet-derived growth factors, and other growth factors [20]. Treatment with platelet-derived growth factors and nerve growth factors have shown to have higher complete healing rates than a placebo [123,124].

2.5.3 Adjunctive Therapies

Adjunctive therapies for PrU treatment include vacuum, electric current, ultrasound, electromagnetic, laser, light, and hydrotherapy.

Vacuum therapy, also called negative pressure therapy (NPT), topical negative pressure (TNP), or vacuum assisted closure (VAC), is the application of negative pressure across a wound to assist in healing [125]. Increase in blood flow, induction of cell proliferation and angionenesis, and reduction of wound surface area are attributed to TNP [126].

Chronic wounds are commonly treated with electric current or electric stimulation (ES) therapy. ES is based on the body's endogenous bioelectric system which signals bone remodeling for fracture healing and regeneration for soft-tissue wounds. ES mimics natural bioelectric currents when the body fails to do so [127]. Ultrasound therapy for PrU involves using low intensity oscillating sound pressure waves to induce blood flow [128]. Electromagnetic therapy (EMT) delivers a pulsed electromagnetic field that induces a field effect in the radio frequency band, commonly 27.12 MHz. The short, on-off pulses used in EMT are thought to encourage cell proliferation by facilitating the migration of electrically charged cells to the wound bed, although the exact mechanism is not well understood [129].

Low-level laser therapy (LLLT), although not well studied *in vivo*, has been thought to influence the rate of wound healing. LLLT accelerates inflammatory phase of wound healing, enhances prostaglandin concentration (cell growth), enhanced ATP synthesis, enhanced collagen synthesis, fibroblast proliferation, and immune system activation [130]. The application of light therapy, or phototherapy, is thought to stimulate the regenerative process in a similar manner. Phototherapy accelerates production of ADP in mitochondria, restores cell membrane potential, and stimulates fibroblast and collagen proliferation [131].

Two common modalities of hydrotherapy are whirlpool and pulsatile lavage. Whirlpool therapy is common, but is expensive, inconvenient, and poses cross-contamination risks as the patient must be immersed in a tub that gets used by all others in whirlpool therapy. Pulsatile lavage provides localized hydrotherapy by supplying a pulsing, pressurized stream of standard saline via an inexpensive, single-use device [132]. The mechanism of healing provided by hydrotherapy is not well understood, but assumed to heavily rely on debridement properties [132].

Several studies have shown electric current, laser, and ultrasound treatments to have no significant affect on PrU healing [115,133,134]. Two studies found that electromagnetic therapy improved wound healing [135,136]. Similarly, light therapy has been shown to have insubstantial healing improvement [137].

CHAPTER 3. SPECIAL CONSIDERATIONS FOR THE NEONATAL POPULATION

3.1 Introduction

Skin health is especially important for neonates adjusting from an aquatic to an aerobic environment [40]. Not only do neonates have a disproportionately large head, greater body surface area, and an inadequate epidermal barrier, they are also at increased risk of skin breakdown due to electrolyte imbalance, fluid imbalance, and thermal instability [138,139]. The importance of neonatal skin is emphasized by the fact that skin makes up for approximately 13% of a neonate's total body weight as opposed to 3% in adults [140]. Just as with adults, the skin offers protection from physical, chemical, and biological aggressors, with barrier function nearly entirely at the stratum corneum level [141].

3.2 Neonatal Skin Anatomy and Physiology

As with adults, neonatal skin tissue is composed of epidermal, dermal, and hypodermal layers, the thickness and composition of which, however, may be very different. The differences in composition are especially dependent on the gestational age at birth and lead to vulnerabilities not common in adult skin tissue.

While adults and full term babies typically have 10-20 layers of stratum corneum, premature babies lack sufficient stratum corneum, appearing gelatinous without healthy

coloring from missing keratinocytes [40]. Premature neonates less than 30 weeks gestational age have 2-3 layers of stratum corneum and micro premature neonates less than 24 weeks gestational age have no stratum corneum. This is especially concerning given that the stratum corneum protects very vulnerable neonates from evaporative heat loss and transepidermal water loss (TEWL). Neonates born at less than 30 weeks gestational age have been shown to experience TEWL at rates fifteen times greater than that of adults [40]. Despite the lack of stratum corneum at birth, however, adult levels of stratum corneum are reached within a few weeks of birth. Conflicting evidence exists for the exact postconception or postnatal age at which the stratum corneum matures [142-144]. Generally, neonatal skin is said to be in a state of flux as the neonate adjusts to extrauterine life [145].

Another skin vulnerability in infants lies at the dermal-epidermal junction. The junction between the dermis and epidermis is underdeveloped with very few fibrils in the basal layer. A lack of fibrils leads to compromised cohesion between the two layers. This often leads to epidermal stripping, in which the epidermal layer is stripped off of the skin as adhesive tape is removed (Figure 10) [40,138,139].

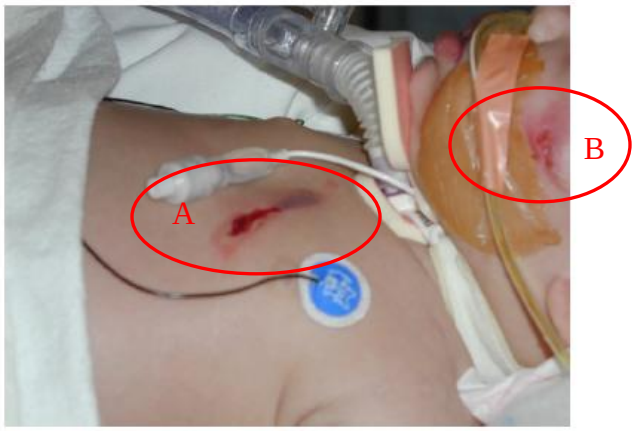

Figure 10. A. Medical-device related DTI from prone positioning on the pilot ballon of tracheostomy tube and B. epidermal stripping from adhesive tape [146].

Neonates often have diminished amounts, if any, of adipose between the dermis and deep tissues [139]. While not well studied, this could have significant implications in the development of neonatal PrUs.

3.3 Neonatal Pressure Ulcer Prevention and Treatment

Similar to adult PrUs, neonatal PrUs result from prolonged mechanical loading (pressure, friction, and/or shear); however, the source of loading is not only pressure over a bony prominence, but is often due to life-sustaining medical devices [40]. While adults can generally tolerate low levels of mechanical loading for a given amount of time according to Reswick and Rogers pressure-time curve, pediatric patients and neonates have developed PrUs in less than one hour of admission [18,139,147]. The widely accepted safe level of pressure in adults is between 28 mmHG and 38 mmHG, with ischemia often resulting at 32 mmHG. In neonates, this has not been well studied.

The top three PrU inducing medical devices in descending order are O_2 saturation probe, non-invasive ventilation mask, and orthotics [146]. Some other common PrU inducing medical devices are vascular access devices, positioning agents, gastronomy tubes, endotracheal tubes, trachesotomy related, continuous positive airway pressure machines (CPAP), bi-level positive airway pressure machines (BiPAP), extracorporeal membrane oxygen (ECMO), oxygen cannulas, pulse oximeters, wires, and adhesives [39,40,146,148]. Common anatomical locations for neonatal PrUs are areas of the head, especially the occiput, seat, and foot [38,40,149,150].

Prevention and treatment for neonatal PrUs follows the same pathway as in adults, including management of contributing factors, wound care, and adjunctive therapies. As with adults, management of contributing factors includes the use of support surfaces, frequent 2-4 hour repositioning, frequent diaper changes for incontinence, and, in the case of EFA, zinc, or arginine deficiencies or failure-to-thrive, enteral or parenteral nutritional supplementation [40,139,151].

In the NICU, there are several different types of support surfaces, including soft flannelette or silk sheets, sheep skin, a standard crib mattress, low air loss beds, foam overlays, gel filled pillows, water pillows and any combination of these [38,152-154]. The majority of such support surfaces are designed for the adult population, likely due to the larger population of adult PrUs. Low air loss beds must be artificially weighed down so that pediatric patients artificially meet the minimum weight the control systems can accommodate [38]. Similarly, water pillows are not purchased, but hand made by the nursing staff using adapted irrigation or ice bags, with no standardization for construction

or volume [152]. Several studies have found that interface pressure is minimized with the combined use of foam and gel overlay and foam overlays alone [38,152,153].

As with adult wound care, neonatal wound care focuses on maintaining a moist wound bed to facilitate cell migration; therefore, the wound bed is dressed with transparent adhesive, hydrogels, and hydrocolloids (adhesive matrix with a dispersion of gelatin, pectin and carboxy-methylcellulose that absorbs wound exudates). Petroleum based emollients, such as Vasoline® or Aquaphor®, are the preferred oinments in order to minimize exposure to harsh chemicals. Antibiotic ointments are minimized to polysporin, bacitracin, and bactroban, as infants may become sensitized to ingredients in other formulations [40].

Adjunctive therapies have not been well studied in the pediatric population, especially outside of anecdotal case studies. Recently NPT, was shown to be an effective wound healing accelerator in neonatal and pediatric populations with several benefits, such as fewer dressing changes, less pain, and a secure (not easily dislodged) dressing [155].

3.4 Neonatal Occipital PrUs

One of the most common places that neonates develop PrUs is on the posterior skull near the occiput [38]. Current supine sleeping recommendations from the American Academcy of Pediatrics Back to Sleep program exacerbate the tendency of PrU formation on the occiput [152]. Important to the understanding of neonatal occipital PrUs is the variance in neonatal head shape. The shape of a neonate’s head can be changed via fetal head molding due to forces of labor in the birth canal or head shaping due to positional

preferences (e.g. supine lying, preference for one side of the head, prolonged inclined lying in infant swings, etc.) [156,157]. Depending on the severity of head molding and shaping, the geometry may alter a neonate's vulnerability to PrU development.

The cephalic index (CI) is a standard measure used to quantify head shape in neonates. The CI is a percentage of head width to length and is therefore given by

$$CI = \frac{width}{length} \tag{3.1}$$

where the width is the distance between the furthest projections on the side of the head (biparietal eminences) and the length is the distance from the glabella to the furthest projection of the posterior skull (eyebrows to the occiput) [158,159].

Cohen's classification creates four categories of neonatal head shape, namely dolichocephaly (CI<75.9), mesocephaly (76>CI>80.9), brachycephaly (81>CI>85.4), and hyperbrachycephaly (CI >85.5) [160]. Dolichocephaly (Figure 11) , more commonly found in pre-term infants, is characterized by a narrow width and elongation in the anterior-posterior direction, persists after discharge from the NICU, and is associated with adverse neurodevelopment [161]. Mesocephaly is a head shape having average width and length.

Figure 11. Decreased biparietal width and elongation in the anterior-posterior direction characteristic of dolicocephaly [162].

Brachycephaly and hyperbrachycephaly (Figure 12) are characterized by widened biparietal distance and shortened anterior-posterior distance and is most frequently caused by continuous supine positioning [163].

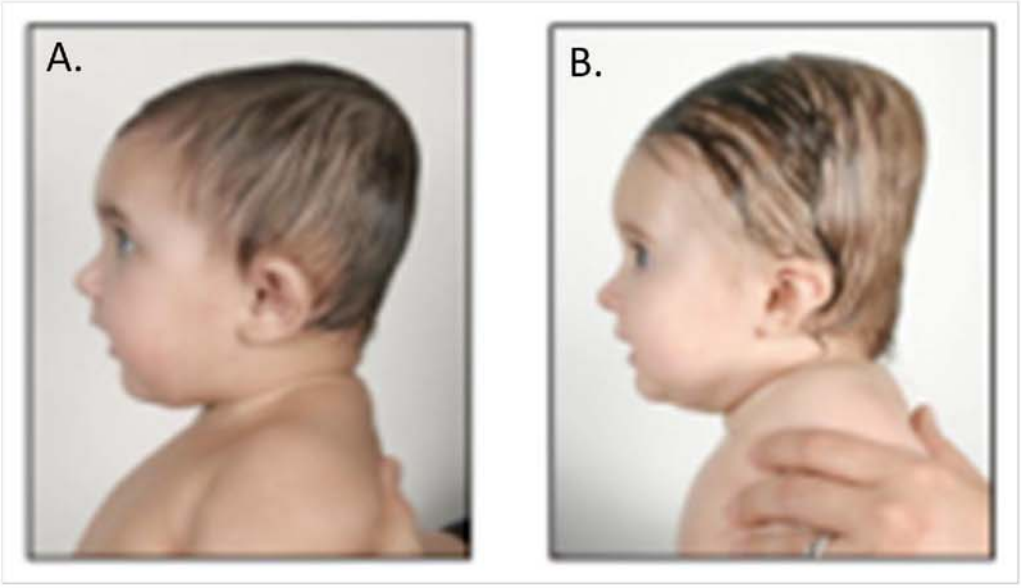

Figure 12. Increased biparietal width and shortened anterior-posterior distance characteristic of an infant with a.) brachycephaly (81>CI>85.4) and b.) hyperbrachycephaly (CI>85.5) [164].

Neonatal PrU literature does not address the affects of head shape on PrU development. However, head shape may be a valuable indicator for PrU development as it affects the distribution of pressure on the posterior skull.

3.5 Static Analysis of the Neonatal Skull

A static analysis of a neonatal in supine-lying position can inform future complex models of sustained interface pressure levels. The following analysis considers the neonatal head as mass (H) and neck as pin joint (N) at the C2-C3 cervical spine joint [165]. The point of contact between the head and the support surface is denoted by point A, the linear distance from the center of gravity of the head to the pin joint N is denoted as L_1, and the linear distance from the point of contact A to the pin joint N is denoted as L_2. The center of the mass of the head is taken to be at the approximate mean, 0.4 cm anterior and 2.3 cm superior from the superior margin of the auditory meatus. Reaction moments at the neck are assumed zero due to the lack of muscle tone characteristic of neonates.

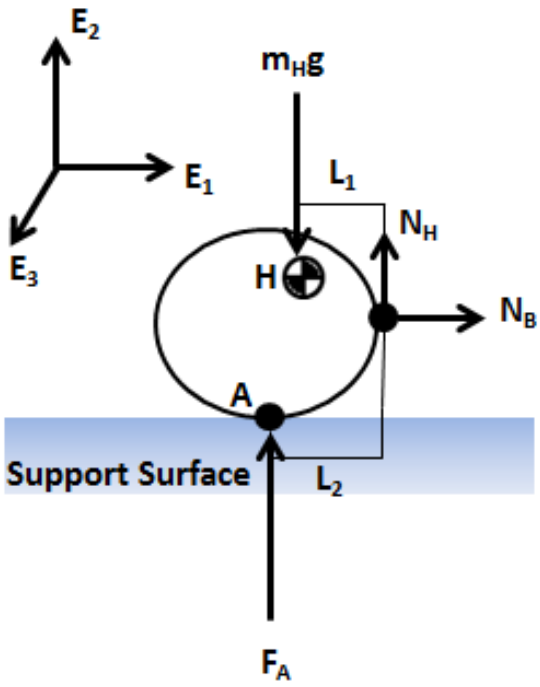

Figure 13. The static analysis of supine-lying neonatal occipital interface pressure includes the head as mass *H* and the neck as pin joint *N*. Contact at the support surface is at point *A*. Reaction forces at the neck are assumed zero due to the lack of neck muscle tone characteristic of neonates.

Assuming static loading and using Newton's second law of motion in the $\boldsymbol{E_2}$ direction results in the following

$$\sum \underline{F} = F_A \underline{E_2} - m_H g \underline{E_2} + N_H \underline{E_2} = 0 \tag{3.2}$$

$$\sum \underline{M}_{/A} = L_1 m_H g \underline{E_3} - L_2 F_A \underline{E_3} = 0 \tag{3.3}$$

Solving for the contact force at point *A* results in the following reduced form,

$$F_A = \frac{L_1}{L_2} m_H g. \tag{3.4}$$

The force at point *A* is used to calculate interface pressure,

$$P_A = \frac{1}{A}\left(\frac{L_1}{L_2} m_H g\right) \tag{3.5}$$

where A is the surface area of contact between the head and the support surface.

3.6 Sensitivity Analysis

A Cotter's sensitivity analysis was used to determine the sensitivity of the pressure function to each input by considering the functional relationship and range of each parameter. Cotter's method, also called the systemic fractional replicate design method is a two level factorial design that requires $2n_p + 2$ simulations to analyze n_p factors of interest. The range for each parameter of interest is used to assign the maximum and minimum values as the upper (+1) and lower (-1) values respectively. The $2n_p + 2$ trials consist of (i) one trial with all factors at the lower level, (ii) n_p trials with each factor in turn raised to its upper lever while the others remain low, (iii) n_p trials with each factor in turn decreased to its lower level while the others remain high, and (iv) one trial with all factors at the upper level [166-168].

Table 3. Example of trials required for a Cotter's analysis with $n_p = 4$.

Trial Number	**1**	**2**	**3**	**4**	**5**	**6**	**7**	**8**	**9**	**10**
Output	y_1	y_2	y_3	y_4	y_5	y_6	y_7	y_8	y_9	y_{10}
x_1	-1	+1	-1	-1	-1	-1	+1	+1	+1	+1
x_2	-1	-1	+1	-1	-1	+1	-1	+1	+1	+1
x_3	-1	-1	-1	+1	-1	+1	+1	-1	+1	+1
x_4	-1	-1	-1	-1	+1	+1	+1	+1	-1	+1

Using the output of each trial, the contrasts for estimating the effects of the j^{th} (j=1,2,…,n_p) parameter on the output y_i are defined as

$$C_0(j) = \frac{1}{4}\left[\left(y_{(2n_p+2)} - y_{(j+n_p+1)}\right) + \left(y_{(j+1)} - y_{(1)}\right)\right] \quad (3.6)$$

$$C_e(j) = \frac{1}{4}\left[\left(y_{(2n_p+2)} - y_{(j+n_p+1)}\right) - \left(y_{(j+1)} - y_{(1)}\right)\right] \quad (3.7)$$

The parameters are ordered using the measure, defined by,

$$M(j) = |C_0(j)| + |C_e(j)| \quad (3.8)$$

and normalized to the Cotter's sensitivity indices.

$$S(j) = \frac{M(j)}{\sum_{j=1}^{n_p} M(j)} \quad (3.9)$$

3.7 Results and Discussion

The derived relationship for occipital-support surface interface pressure is a function of contact area, head mass, and the ratios of center of gravity to C2-C3 and the point of contact A to C2-C3. The neonatal population was subdivided into term neonates (>37 weeks gestational age (GA)), premature neonates (24-36 weeks GA), and micropremature neonates (<24 weeks GA). A sensitivity analysis with four parameters of interest (Table 4) was completed for each subdivision (Figure 14, Figure 15, and Figure 16) [169-175].

Table 4. Ranges for each parameter of interest within each GA subdivision.

	Parameter of Interest	Low	High	References
micro-Premature (<24 weeks GA)	m (kg)	0.09	0.18	[187-192]
	L_1 (m)	0.006	0.008	--
	L_2 (m)	0.009	0.015	--
	A (m^2)	1.86E-07	7.65E-07	[193]
Premature (24-36 weeks GA)	m (kg)	0.09	0.84	[187-192]
	L_1 (m)	0.01	0.04	--
	L_2 (m)	0.01	0.07	--
	A (m^2)	2.00E-07	3.70E-06	[193]
Full Term (>37 weeks GA)	m (kg)	0.49	1.1	[187-192]
	L_1 (m)	0.03	0.05	--
	L_2 (m)	0.05	0.1	--
	A (m^2)	1.00E-06	5.00E-06	[193]

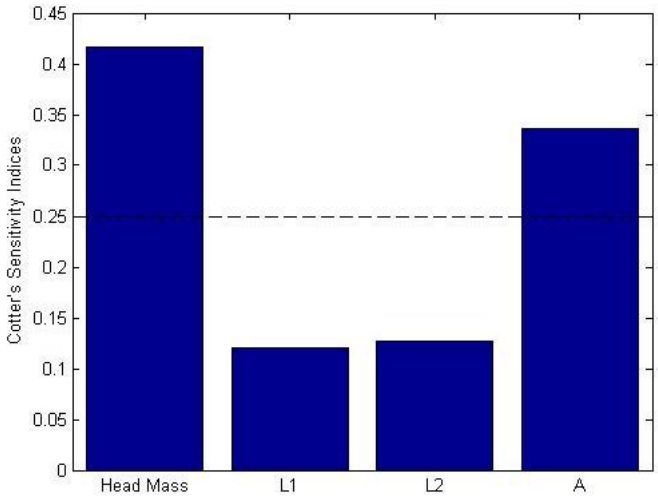

Figure 14. Cotter's sensitivity indices for occipital interface pressure of micro premature (<24 weeks GA) neonates. Head mass followed by contact area are the sensitive parameters.

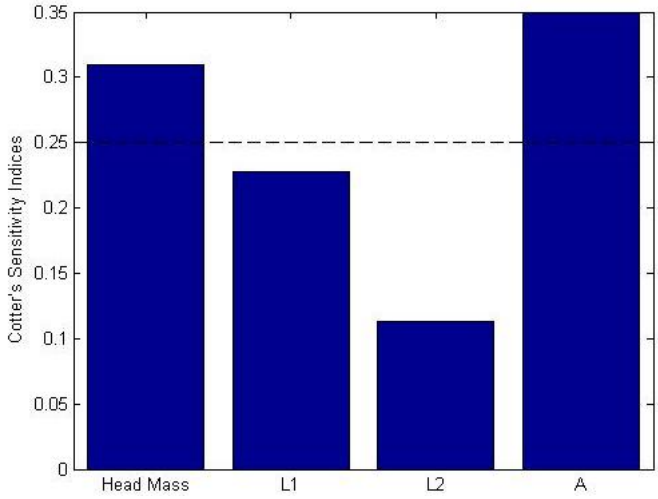

Figure 15. Cotter's sensitivity indices for occipital interface pressure of premature (24-36 weeks GA) neonates. Contact area followed by head mass are the most sensitive parameters.

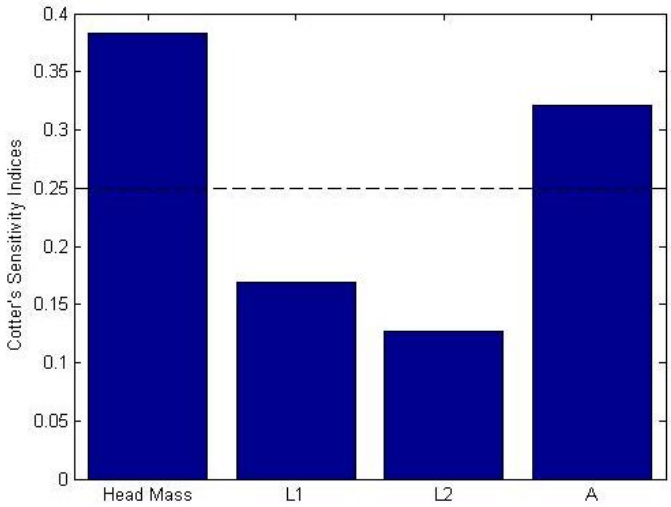

Figure 16. Cotter's sensitivity indices for occipital interface pressure of term (>37 weeks GA) neonates. Head mass followed by contact area are the most sensitive parameters.

Head mass and contact area were sensitive parameters for neonates of each GA group. There are no significant differences in parameter sensitivity between the groups. Head mass and contact area are both parameters that may be addressed in the design of protocols and devices to prevent neonatal PrUs. While the issue of head mass cannot be

directly addressed, it may be addressed indirectly by inclining the neonate to reduce the normal force, although this type of positioning may induce shear stresses. The contact area will vary greatly depending on both GA and the head shape (quantified by CI) of the neonate. For example, a dolichocephalic neonate might experience much higher normal stresses due to the decreased contact area of the head elongated in the anterior-posterior direction; whereas, a brachycephalic neonate might have greatly reduced stresses as the flattened posterior skull distributes more load. Moreover, a better understanding of neonatal head shape and geometry via patient-specific imaging may inform the design of a support surface or positioning that optimally reduces interface pressure.

Finally, although L_1 and L_2 are not sensitive parameters, the ratio of L_1 and L_2 could potentially be a mechanism for assessing PrU risk in neonates similar to the CI. For example, a brachycephalic neonate with elongation of the biparietal breadth and shortening in the anterior-posterior direction. This implies that L_2 is shortened, thus increasing the interface pressure. There is potential for the development of acceptable ranges of $\frac{L_1}{L_2}$ such that PrU risk may be efficiently assessed.

CHAPTER 4. QUASI-STATIC MIXTURE THEORY

4.1 Introduction

Modeling has been a critical component in the efforts to fully understand PrU etiology. Decades of PrU modeling have resulted in simulations that have evolved with state-of-the-art computing methods from highly simplified linear mathematical models to dimensional analysis to mixture theory, and finally to finite element and agent-based modeling [18,19,59,63,176-187].

PrU modeling has focused on different aspects of PrU etiology over time, including tissue hydrostatic pressure, shear stresses, impaired microcirculation, hypoxia, reperfusion injury, compromised interstitial transport processes, and compromised lymphatic return [59]. Some of the most basic models qualitatively address these factors using pressure-time threshold curves, such as those developed by Reswick and Rogers [18] and Kosiak [188]. Likewise, Sacks [19] developed a theoretical prediction of a pressure-time threshold curve using dimensional analysis, resulting in an exponential relationship between pressure (p) and time (t), $p \; \alpha \; t^{-\frac{4}{3}}$.

While interface skin-support surface pressure measurements have often been used in an attempt understand pressure-time thresholds, PrU may or may not begin at this interface but deep within the cutaneous and subcutaneous tissues. For this reason, both the form and significance of the hydrostatic pressure term have often been debated. The

relationship between externally applied pressure and interstitial fluid pressure has been shown to be non-linear. The magnitude of interstitial fluid pressure is generally less than the externally applied pressure [63,189,190].

Two- and three-dimensional estimations of stress distributions have been obtained using finite element models. These models are often used to inform support surface design. Chow and Odell (1978) developed a 3D finite element model of the buttocks that both demonstrated the importance of interface shear on pressure and showed that tissue distortion was greatest internally as opposed to superficially, suggesting a different tolerance to pressures in skin, fat, and muscle tissue [176,191]. Reger et al. (1990) estimated tissue deformation and stiffness using MRI images of the buttocks of paraplegics and non-paraplegics noting a significant difference [192]. Makhsous (2007) developed a 3D buttock model that derives geometry from patient-specific MRIs [183]. Shaked (2013) studied microclimate effects, specifically moisture-content-related coefficient of friction changes and its effect on interface pressure using a 2D finite element model [184].

Despite the fact that many contributing factors of PrU etiology are transport related, few models address fluid flow. Mak *et al*. [59] developed a biphasic poroelastic model of skin and subcutaneous tissues that studied the biomechanical response of such tissues to tissue fluid flows under varying loading conditions. Key results showed hydrostatic pressure build-up in the tissue along with tissue compaction as fluid gradually moves away from the compacted area [59]. Shilo and Gefen [193] studied the collapse of straight, U-shaped, and bifurcated capillaries using an inverse finite element method. It was determined that low capillary blood pressure increased the likelihood of capillary

collapse, especially when combined with external loading. These results offer some insight into the compressive strain at which capillary occlusion occurs.

Mixture theory has successfully been applied to many biological tissues, including articular cartilage, aortic tissues, intervertebral disks, cortical bone, and ventricular tissues [59,178,179,194-197]. PrU mixture theory modeling often draws on foundational models of articular cartilage developed by van Mow [178]. Oomens developed an incompressible, biphasic model for the mechanics of skin using non-linear material models [179]. Mak *et al* developed an incompressible, biphasic poroelastic model of skin and subcutaneous tissue using linear elastic materials to observe fluid flow and tissue compaction [59].

Although the individual constituents may be assumed incompressible because they are structures at the microscale, the cutaneous and subcutaneous tissues as a whole are allowed to undergo changes in volume via the exudation of fluids. Skin tissue deformation is largely regarded as non-linear. Therefore, incompressible models relying on linear elastic materials may be limited in predictive capability. To demonstrate, both linear elastic and hyperelastic neo-hookean incompressible models were developed under quasi-static loading conditions and calibrated using *in vivo* compression data.

4.1.1 Linear Elastic Materials

For a biphasic, homogeneous mixture composed of a solid constituent (*s*) extracellular matrix and a fluid constituent (*f*) interstitial fluid, the solid constituent is defined by the position of a solid particle, x_i, at time t in terms of the reference configuration of the particle, X_i, as follows

$$\begin{cases} x_1 = \lambda_1 X_1 \\ x_2 = \lambda_2 X_2 \\ x_3 = \lambda_3 X_3 \end{cases} \quad (4.1\text{-}4.3)$$

Assuming unconfined compression, $\lambda_1 = \lambda_2 = 1$, and the solid deformation gradient reduces to

$$\underline{F}^s = \begin{bmatrix} 1 & 0 & 0 \\ 0 & 1 & 0 \\ 0 & 0 & \lambda_3 \end{bmatrix}. \quad (4.4)$$

The Cauchy stresses, $\underline{T}^\alpha$, are defined as

$$\begin{cases} \underline{T}^s = -\varphi^s p + \varphi^s(\lambda + 2\mu)\varepsilon \\ \underline{T}^f = -\varphi^f p \\ \underline{T}^T = \underline{T}^s + \underline{T}^f \end{cases} \quad (4.5\text{-}4.7)$$

where ε is the tissue strain, the solid constituent volume fraction, φ^s, is determined by

$$\varphi^s = \frac{\varphi_0^s}{J^s} \quad (4.8)$$

and the mixture is subject to the constraint $\sum_\alpha \varphi^\alpha = 1$. Enforcing a zero stress state and considering $(\lambda + 2\mu)$ to be an aggregate modulus, H_A, the final form of solid Cauchy stress is

$$\underline{T}^s = \frac{\varphi_0^s}{\lambda} H_A \varepsilon. \quad (4.9)$$

Calibration with *in vivo* experimental data collected by Bader [48] via plane-ended cylindrical indention tests of the anterior forearm on a fixed surface (Appendix A) results in a root mean squared error (RMSE) of 3.09kPa and an aggregate modulus of 31.65kPa.

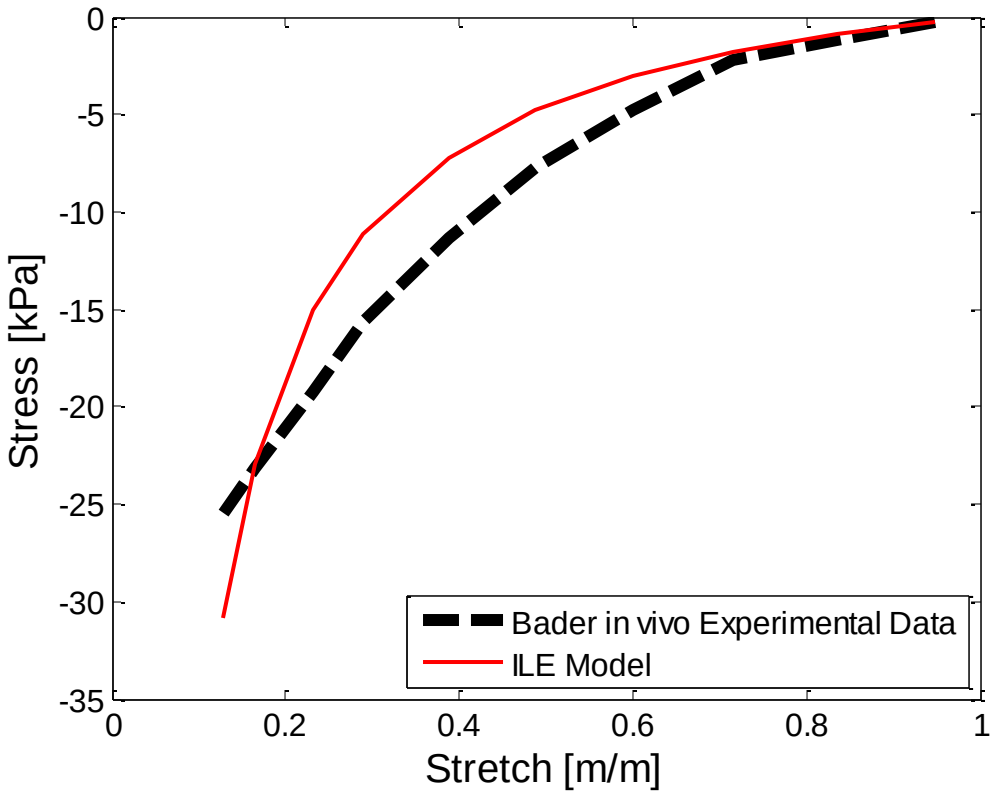

Figure 17. Calibration of the biphasic mixture model with incompressible linear elastic (ILE) solid constituent resulted in an $RMSE = 3.09kPa$ and an aggregate modulus, $H_A = 31.65kPa$. The linear elastic model is limited in predictive capabilities to the linear, low strain region.

4.1.2 Hyperelastic, Neo-Hookean Materials

For a biphasic, homogeneous mixture composed of a solid constituent (*s*) extracellular matrix and a fluid constituent (*f*) interstitial fluid, the hyperelastic, neo-hookean solid constituent is defined by the position of a solid particle, x_i, at time *t* in terms of the reference configuration of the particle, X_i, as follows

$$\begin{cases} x_1 = \lambda_1 X_1 \\ x_2 = \lambda_2 X_2 \\ x_3 = \lambda_3 X_3 \end{cases} \quad (4.10\text{-}4.12)$$

Assuming unconfined compression, $\lambda_1 = \lambda_2 = 1$, and the solid deformation gradient reduces to

$$\underline{F}^s = \begin{bmatrix} 1 & 0 & 0 \\ 0 & 1 & 0 \\ 0 & 0 & \lambda_3 \end{bmatrix}. \tag{4.13}$$

The Cauchy stress is defined as

$$\begin{cases} \underline{T}^s = -\varphi^s p + \varphi^s G \underline{B}^s \\ \underline{T}^f = -\varphi^f p \\ \underline{T}^T = \underline{T}^s + \underline{T}^f \end{cases} \tag{4.14-4.16}$$

where $G$is tissue shear modulus, the solid constituent volume fraction, φ^s, is determined y the initial constituent volume fraction and the Jacobian, $\varphi^s = \frac{\varphi_0^s}{J^s}$ and $J^s = \det(\underline{F}^s) = \boldsymbol{\lambda_3}$, and the left Cauchy-Green tensor is

$$\underline{B}^s = \underline{F}\underline{F}^T = \begin{bmatrix} 1 & 0 & 0 \\ 0 & 1 & 0 \\ 0 & 0 & \lambda_3^2 \end{bmatrix} \tag{4.17}$$

Enforcing a zero stress state condition requires that hydrostatic pressure is set to a constant, $\varphi^s G$, resulting in the following form for Cauchy stress

$$\underline{T}^s = -\varphi^s G + \varphi^s G \lambda_3^2. \tag{4.18}$$

Calibration with *in vivo* experimental data collected by Bader [48] via plane-ended cylindrical indention tests of the anterior forearm on a fixed surface results in an RMSE of 5.91kPa and a shear modulus of 3.83kPa.

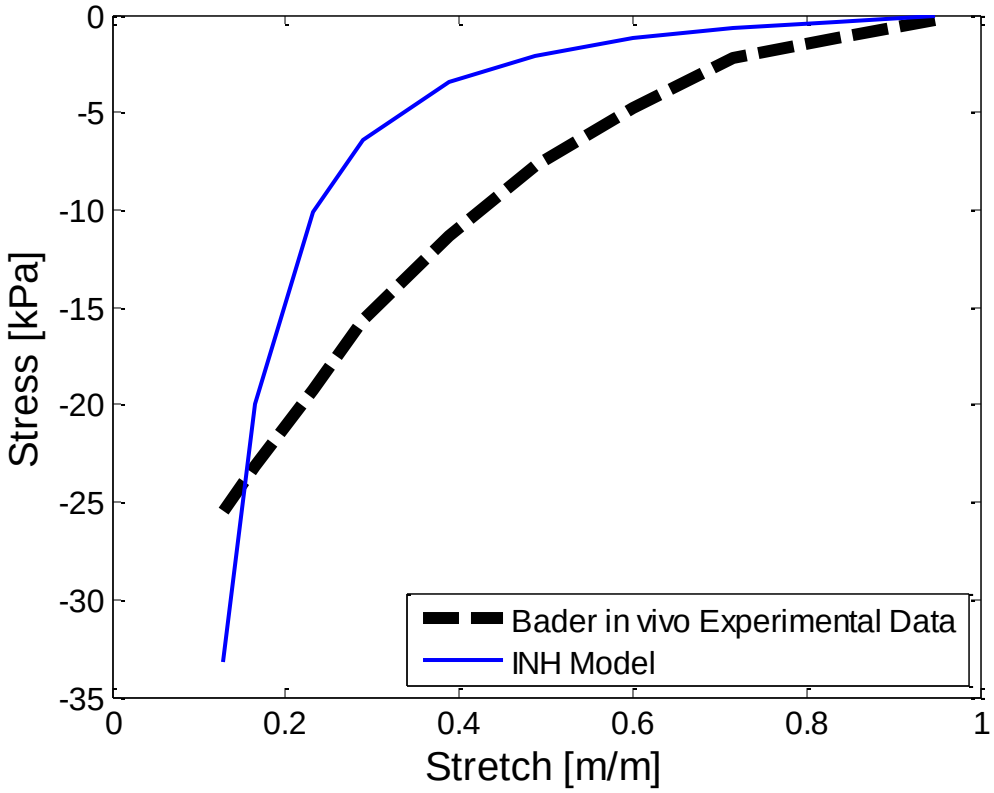

Figure 18. Calibration of the biphasic mixture model with an incompressible hyperelastic neo-hookean (INH) solid constituent resulted in an $RMSE = 5.91kPa$ and a shear modulus, G= $3.83kPa$. The incompressible, hyper elastic model cannot alone accurate predict *in vivo* tissue deformation.

While the incompressible linear elastic model provides very limited predictive capabilities within low strains, the incompressible Neo-Hookean model fails to predict the *in vivo* tissue deformation all together. Although skin tissue has often been treated as incompressible, as a whole the continuum is allowed to undergo volume changes via the exudation of fluids, including interstitial fluid and blood.

Despite the fact that capillary occlusion is widely regarded as a primary factor in PrU etiology, a model has yet to be developed that isolates blood as a constituent. This

study introduces a compressible, triphasic, quasi-static mixture theory model of cutaneous and subcutaneous tissues towards a better model of tissue stress state and fluid flow in load bearing tissues.

Table 5. Foundational models of PrU etiology. * Denotes models of articular cartilage that, although not directly related to PrUs, are heavily cited within PrU modeling literature.

Foundations of Pressure Ulcer Modeling								
Author (Year)	**Model Type**	**Material Model(s)**	**Anatomical Location**	**Geometry**	**Major Assumptions**	**Input(s)**	**Output(s)**	**Results/Findings**
Chow & Odell (1978)	Finite Element	Linear Elastic	Buttocks	100mm radius hemisphere of soft tissue with rigid core	axisymmetric, fixed tissue-core interface	Surface pressure loadings	von Mises stress	3D stress state in the buttocks that can be determined for different loading conditions or deformation, tissue distrotion is more severe internally and interface shear is the predominant factor in pressure distribution
***Lanir (1990)**	Structural Model	Non-linear, Viscoelastic	Fibrous connective tissue	3D tissue body	isothermal adiabatic anisotropic homogeneous & non-homogeneous	Material properties or experiental data	strain energy	A structural approach to modeling constitutive equations of fibrous tissue
Mak (1994)	Biphasic Mixture	Linear Elastic	Skin over bony substratum	2D tissue layer	Incompressible Homogeneous completely adhered interface free-to-slip interface	cosine indentor - step and cyclic flat-ended indentor - step	displacement pore pressure (hydrostatic pressure) tissue compaction reaction force	Material, geometric, and loading paramters effect of transient biomechanical response, hydrostatic pressure build up and subsequent tissue compaction
***Mow (1980)**	Biphasic Mixture	Linear elastic	Articule cartilage	Cylindrical tissue	incompressible linear deformation	material properties or experiental data	deformation	Predominate mechanism for creep and stress relaxation is diffusional drag between interstitial fluid wrt solid matrix
Oomens (1987)	Biphasic Mixture	Non-linear	Skin		Incompressible	Displacement heat flux	Pressure	numerical method for solution of non-linear field equations describing mixture
Reddy (1981)	Mathematical Model	Linear	Skin	Circular cylindar of tissue	Linear, homogeneous	hydraulic conductivity IFGS volume fraction tissue radius initial volume external pressure	Tme	Inverse relationship between the intensity and duration of external pressure required for the interstitial fluid volume in the pressurized region to reach a given portion of its initial volume
Reswick & Rogers (1976)	Experiemental Curve	NA	Skin over bony prominence	NA	NA	NA	NA	Pressure-time guideline for PrU formation
Sacks (1989)	Dimensional Analysis	NA	None	None	homogeneous	tissue denisty local blood flow elastic modulus time	pressure-time threshold	a method for predicting effects of tissue density, local blood flow, elastic modulus, and time

Table 6. Current state of PrU modeling. ** Denotes a layered skin model developed for the animation industry.

Current State of Pressure Ulcer Modeling								
Author (Year)	**Model Type**	**Material Model(s)**	**Anatomical Location**	**Geometry**	**Major Assumptions**	**Input(s)**	**Output(s)**	**Results/Findings**
Agam (2008)	Hertz Contact Theory	Linear elastic	Buttocks	4mm cylindrical radius	homogeneous, isotropic, elastic, frictionless contact	patient-specific ultra sound/MRI, material properties	stress level	portabale patient-specific real time pressure monitoring
Gefen (2011)	Linear Analytical	NA	Weight-bearing body site	small contact region	steady state microclimate	temperature humidity pressure shear	Dimensionless time for skin breakdown	increase in skin temp, ambient temp, relative humidity, contact pressurs, and decrease in permeability decrease skins tolerance to PrUs
Hung (2009)**	3D Finite Element	Mooney-Rivlin, incompressible, isotropic	Skin	four layers	isotropic, non-linear, large deformation, homogeneous	calcium concentration (muscle contraction)	Deformation	aged skin wrinkled more easily, large adipose layers prohibited wrinkling, wrinkle density is higher on thin skin, and inhomogeneity should be considered
Makhsous (2007)	3D Finite Element	Mooney-Rivlin, incompressible	Buttock-thigh	MRI	Axisymmetric	Seated position	von Mises stress displacement	validated, 3D buttock model with realistic boundary and loading conditions
Shaked (2013)	2D Finite Element	Linear elastic	Weight-bearing bony prominence	60 mm length of tissue layer	isotropic, incompressible	material properties, loading condition	Effective stress, shear stress	stress increases as moisture-content-related COF between skin and support surface increases and become more prominent in stiff skin
Solovyev (2013)	Hybrid Equation (ODE) - Agent Based Model	epithelial cells, macrophages, blood vessels, pro-inflammatory cytokine agent, anti-inflammatory cytokine, oxygen	Skin	NA	NA	Cyclic Pressure	epithelial cells, macrophages, blood vessels, pro-inflammatory cytokine agent, anti-inflammatory cytokine, oxygen	predicted higher propensity for PrU in SCI patients than in the control group
Stern (2013)	Agent Based Model	neutrophils macrophages epithelial cells blood vessels	Skin	NA	NA	Pressure	neutrophils macrophages epithelial cells blood vessels	tissue-realistic mechanistic models of PrU formation with the potential to be used as diagnostic tool
Ziraldo (2013)	Agent Based Model	blood vessels macrophages tissue cells	Skin	NA	NA	Pressure	blood vessels macrophages tissue cells	control points to reduce stress determined for SCI and control group patients

4.2 Theory

In order to describe the mechano-physiological processes of load-bearing human cutaneous and subcutaneous tissue, a mixture theory based model is developed and interfaced with uniform and modified Hertzian contact mechanics input. Human skin tissue is a complex system, composed of several distinct layers (epidermis, dermis, and hypodermis) and structures (follicles, vasculature, sebaceous glands, etc.). Each layer contains many different components including collagen and elastin in a gel continuum of mucopolysaccharides with a principle mass of collagen [40]. Previous models of load-bearing skin tissue typically consider biphasic continua with a single solid and single fluid component, such that all fluids are lumped into the fluid constituent [59]. For the purposes of this study, along with the solid extracellular matrix (ECM) constituent, two fluids will be considered, interstitial fluid (IF) and blood. Therefore, the three constituents of the triphasic mixture are extracellular matrix (s), interstitial fluid (f), and blood (b). The tissue is assumed to be compressible, homogeneous, and isotropic and is subjected to quasi-static loading.

Each constituent is regarded as a continuum having its own properties, kinematics, and balance laws. As such, each constituent has its own mass, volume, apparent, and true density, M^α, V^α, ρ^α and ρ_T^α, where $\alpha = s, f, b$. Apparent density and true density are related by the volume fraction, φ^α such that $\rho^\alpha = \varphi^\alpha \rho_T^\alpha$. The volume fraction of each constituent is given by $\varphi^\alpha = V^\alpha / V$ such that at any given time $\sum_\alpha \varphi^\alpha = 1$.

The governing equations for mixture theory are the balance of mass and the conservation of linear momentum. The general form of the balance of mass is

$$\frac{D^{\alpha}\rho^{\alpha}}{Dt} + \rho^{\alpha}\nabla \cdot \underline{v}^{\alpha} = \hat{q}^{\alpha} \tag{4.19}$$

where $\frac{D^{\alpha}h}{Dt} = \frac{\partial h}{\partial t} + \frac{\partial h}{\partial x_i} v_i^{\alpha}$ is the material derivative, $\underline{\boldsymbol{v}}^{\alpha}$ is the velocity of the α-constituent and $\hat{q}^{\alpha} = \rho_T^{\alpha}\hat{r}^{\alpha}$ is the rate of mass production per unit volume. The general form of the conservation of linear momentum is

$$\rho^{\alpha}\frac{D^{\alpha}\boldsymbol{v}^{\alpha}}{Dt} = \nabla \cdot \underline{T}^{\alpha} + \rho^{\alpha}\underline{b}^{\alpha} + \underline{\pi}^{\alpha} \tag{4.20}$$

where $\underline{T}^{\alpha}$ is the Cauchy stress tensor, $\underline{b}^{\alpha}$s body force, and $\underline{\pi}^{\alpha}$ is the inter-constituent interaction term.

Assuming quasi-static deformation, zero mass production, and zero body forces the balance of mass and conservation of linear momentum become

$$\nabla\rho^{\alpha} \cdot \underline{v}^{\alpha} + \rho^{\alpha}\nabla \cdot \underline{v}^{\alpha} = 0 \tag{4.21}$$

and

$$\rho^{\alpha}\nabla\underline{v}^{\alpha} \cdot \underline{v}^{\alpha} = \nabla \cdot \underline{T}^{\alpha} + \underline{\pi}^{\alpha} \tag{4.22}$$

The general forms for the balance of mass and conservation of linear momentum of the three constituent mixture are therefore

$$\nabla\rho^{s} \cdot \underline{v}^{s} + \rho^{s}\nabla \cdot \underline{v}^{s} + \nabla\rho^{f} \cdot \underline{v}^{f} + \rho^{f}\nabla \cdot \underline{v}^{f} + \nabla\rho^{b} \cdot \underline{v}^{b} + \rho^{b}\nabla \cdot \underline{v}^{b} = 0 \tag{4.23}$$

$$\begin{cases} \rho^{s}\nabla\underline{v}^{s} \cdot \underline{v}^{s} = \nabla \cdot \underline{T}^{s} + \underline{\pi}^{s} \\ \rho^{f}\nabla\underline{v}^{f} \cdot \underline{v}^{f} = \nabla \cdot \underline{T}^{f} + \underline{\pi}^{f} \\ \rho^{b}\nabla\underline{v}^{b} \cdot \underline{v}^{b} = \nabla \cdot \underline{T}^{b} + \underline{\pi}^{b} \end{cases} \tag{4.24-4.26}$$

4.2.1 Geometry and Quasi-Static Deformation

Consistent with existing models of load-bearing skin, the skin and all of its layers and structures are considered together in a lumped model including the epidermis, dermis, and hypodermis. The epidermal layer, bounded by the superior stratum corneum layer, is considered impervious and the muscle layer is assumed to be the fixed inferior base. The reference coordinate system is placed at the surface of the muscle tissue (Fig 23).

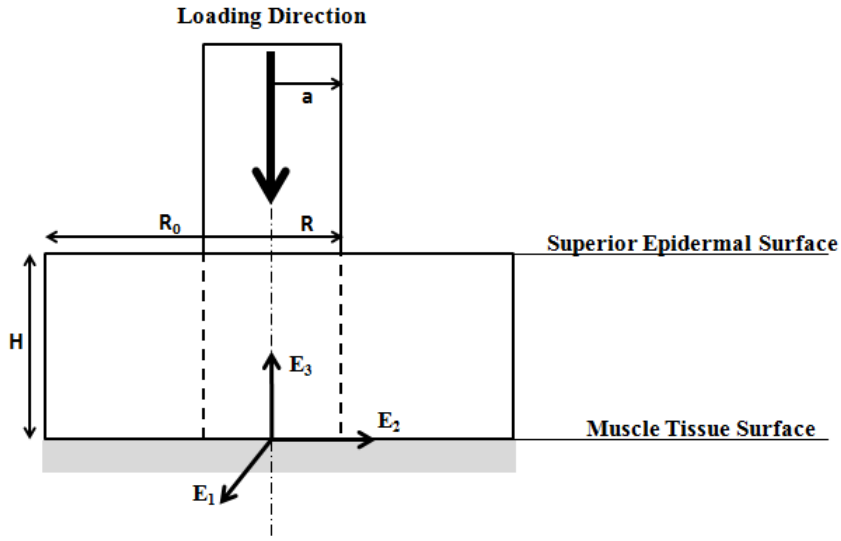

Figure 19. Cross section of cutaneous and subcutaneous tissue with the reference coordinate system at the superior surface of the fixed muscle tissue. Loading is assumed to be primarily in the inferior $\mathbf{E_3}$ direction.

For loading in the superior-inferior $\boldsymbol{E_3}$ direction, the deformation of the solid constituent is derived as follows

$$\begin{cases} {x_1}^s = {X_1}^s - \eta\varepsilon_3 {X_1}^s \\ {x_2}^s = {X_2}^s - \eta\varepsilon_3 {X_2}^s \\ {x_3}^s = {X_3}^s + \varepsilon_3 {X_3}^s \end{cases} \qquad (4.27\text{-}4.29)$$

where ${X_i}^s$ describes the reference configuration and ${x_i}^s$ describes the current configuration. The expansion ratio, η, accounts for Poisson-like effects in the $\boldsymbol{E_1}$ and $\boldsymbol{E_2}$ directions. The macroscopic strain, ε_3 (ε_Z), is prescribed.

For an axisymmetric analysis, a coordinate transformation from cartesian to cylindrical coordinates is necessary. The transformation results in the following form for solid deformation

$$\begin{cases} r^s = R^s(1-\eta\varepsilon_Z) \\ \theta^s = \Theta^s \\ z^s = Z^s(1+\varepsilon_Z) \end{cases} \tag{4.30-4.32}$$

where $[R^s, \Theta^s, Z^s]$ describe the reference configuration and $[r^s, \theta^s, z^s]$ describe the current configuration of the solid constituent. The resultant deformation gradient in terms of displacement, u_i, is dependent on the prescribed strain [198]

$$\underline{\underline{F^s}} = \underline{\underline{I}} + \nabla u = \begin{bmatrix} 1+\frac{\partial u_R}{\partial R} & 0 & \frac{\partial u_R}{\partial Z} \\ 0 & 1+\frac{u_R}{R} & 0 \\ \frac{\partial u_Z}{\partial R} & 0 & 1+\frac{\partial u_Z}{\partial Z} \end{bmatrix} \tag{4.33}$$

where the displacement is defined by

$$u_R = r^s - R^s = -\eta\varepsilon_Z R^s \tag{4.34}$$

$$u_z = z^s - Z^s = \varepsilon_Z Z^s \tag{4.35}$$

The Cauchy stress tensors for each constituent are described as follows

$$\begin{cases} \underline{\underline{T^s}} = -\varphi^s p\underline{\underline{I}} + \varphi^s\underline{\underline{\hat{T}^s}} \\ \underline{\underline{T^f}} = -\varphi^f p\underline{\underline{I}} \\ \underline{\underline{T^b}} = -\varphi^b p\underline{\underline{I}} \end{cases} \tag{4.36-4.38}$$

where p is the hydrostatic tissue pressure, $\underline{\underline{\hat{T}^s}}$ is the compressible neo-hookean solid constitutive equation

$$\underline{\hat{T}}^s = \kappa J^s(J^s - 1)\underline{I} + \frac{\mu}{J^{s^{2/3}}} dev(\underline{B}^s) \tag{4.39}$$

and the total Cauchy stress is

$$\underline{T}^T = \underline{T}^s + \underline{T}^f + \underline{T}^b = -p\underline{I} + \varphi^s \underline{\hat{T}}^s. \tag{4.40}$$

In the equations above, κ is the tissue bulk modulus, μ is the tissue shear modulus, $\underline{B}^s$ is the left Cauchy-Green deformation tensor, and the deviatoric component of $\underline{B}^s$is

$$\underline{B}^s = \underline{F}\underline{F}^T = \begin{bmatrix} \left(1 + \frac{\partial u_R}{\partial R}\right)^2 & 0 & \left(1 + \frac{\partial u_R}{\partial R}\right)\left(\frac{\partial u_Z}{\partial R}\right) \\ 0 & \left(1 + \frac{u_R}{R}\right)^2 & 0 \\ \left(\frac{\partial u_Z}{\partial R}\right)\left(1 + \frac{\partial u_R}{\partial R}\right) & 0 & \left(\frac{\partial u_Z}{\partial R}\right)^2 + \left(1 + \frac{\partial u_Z}{\partial Z}\right)^2 \end{bmatrix} \tag{4.41}$$

$$dev\left(\underline{B}^s\right) = \underline{B}^s - \frac{1}{3} I_1\left(\underline{B}^s\right)\underline{I} \tag{4.42}$$

The resulting form of the Cauchy stress tensor in the loading direction, $\mathbf{E_{ZZ}}$, can be derived as such

$$\underline{T}_{ZZ} = -p\underline{I} + \varphi^s \kappa J^s(J^s - 1)\underline{I} + \frac{\varphi^s \mu}{J^{s^{2/3}}}\left\{\left(\frac{\partial u_Z}{\partial R}\right)^2 + \left(1 + \frac{\partial u_Z}{\partial Z}\right)^2 - \frac{1}{3}\left[\left(1 + \frac{\partial u_R}{\partial R}\right)^2 + \left(1 + \frac{u_R}{R}\right)^2 + \left(\frac{\partial u_Z}{\partial R}\right)^2 + \left(1 + \frac{\partial u_Z}{\partial Z}\right)^2\right]\right\}. \tag{4.43}$$

Two different strain inputs were considered for the purposes of calibration, uniform strain and the Hertzian form of contact between a rigid, flat-ended cylinder indenter with an elastic half space. The final form for the Cauchy stress is dependent on the strain input.

4.2.1.1 Uniform Strain Input

Assuming the strain beneath the indenter is uniform, a strain in the $\mathbf{E_Z}$ direction of the form $\varepsilon_Z = -\gamma$ is considered. The resulting deformation gradient in the form of Equation (4.24) above is

$$\underline{F^s} = \underline{I} + \nabla u = \begin{bmatrix} 1-\eta\varepsilon_Z & 0 & 0 \\ 0 & 1-\eta\varepsilon_Z & 0 \\ 0 & 0 & 1+\varepsilon_Z \end{bmatrix} \tag{4.44}$$

where the Jacobian, $J^s = \det(\underline{F^s}) = (1+\varepsilon_Z)(1-\eta\varepsilon_Z)^2$. The total Cauchy stress is therefore given by

$$T_{ZZ}^T = -p_0 + \varphi^s \kappa J^s (J^s - 1) + \frac{\varphi^s \mu}{J^{s^{2}/_3}} \left\{ (1+\varepsilon_Z)^2 - \frac{1}{3}[2(1-\eta\varepsilon_Z)^2 + (1+\varepsilon_Z)^2] \right\}. \tag{4.45}$$

4.2.1.2 Hertzian Contact

The strain profile beneath the indenter is assumed to be similar to the pressure profile characteristic of Hertz theory contact between a rigid, flat-ended cylindrical indenter and an elastic half-space. This results in a strain profile in the $\mathbf{E_Z}$ direction of the form $\varepsilon_Z = -\gamma \left(1 - \frac{R^2}{a^2}\right)^{-\frac{1}{2}}$. The resulting deformation gradient in the form of Equation (4.24) above is

$$\underline{F^s} = \underline{I} + \nabla u = \begin{bmatrix} 1-\eta\varepsilon_Z & 0 & 0 \\ 0 & 1-\eta\varepsilon_Z & 0 \\ \frac{-Z\gamma R}{a^2}\left(1-\frac{R^2}{a^2}\right)^{-\frac{3}{2}} & 0 & 1+\varepsilon_Z \end{bmatrix} \tag{4.46}$$

where the Jacobian, $J^s = \det(\underline{F^s}) = \left(1 - \eta\varepsilon_Z + \frac{\eta\gamma R^2}{a^2}\left(1-\frac{R^2}{a^2}\right)^{-\frac{3}{2}}\right)(1-\eta\varepsilon_Z)(1+\varepsilon_Z)$.

The total Cauchy stress is therefore given by

$$T_{ZZ}^{T} = -p_0 + \varphi^s \kappa J^s (J^s - 1) + \frac{\varphi^s \mu}{J^{s\,2/3}} \left\{ (1 + \varepsilon_Z)^2 - \frac{1}{3} [2(1 - \eta \varepsilon_Z)^2 + (1 + \varepsilon_Z)^2] \right\}. \quad (4.47)$$

4.2.1.3 Derivation of Hydrostatic Pressure

The hydrostatic pressure term may be derived by applying a boundary condition modified from Reddy [63] on the transverse Cauchy stress. It may be assumed that the total Cauchy stress in the $\mathbf{E_{RR}}$ direction at a distance R_o away from the axis of the indenter is equal to hydrostatic interstitial fluid pressure, p_0,

$$T_{RR}^{T} = -p_0 \quad (4.48)$$

and

$$T_{RR}^{T} = -p\underline{I} + \varphi^s \kappa J^s (J^s - 1)\underline{I} + \frac{\varphi^s \mu}{J^{s\,2/3}} \left\{ \left(1 + \frac{\partial u_R}{\partial R}\right)^2 - \frac{1}{3} \left[\left(1 + \frac{\partial u_R}{\partial R}\right)^2 + \left(1 + \frac{u_R}{R}\right)^2 + \left(1 + \frac{\partial u_Z}{\partial Z}\right)^2 \right] \right\}. \quad (4.49)$$

At $R = R_0$, the tissue is underformed ($J^s = 1$ and $\varepsilon_Z = 0$) and substituting Equation (4.48) into (4.49) reduces to $p = p_0$. The hydrostatic pressure is shown to be equal to the initial hydrostatic interstitial fluid pressure of the tissue for quasi-static loading conditions.

4.3 Methodology

4.3.1 Model Calibration

Both forms of strain input, uniform strain and Hertz theory type strain, were calibrated using *in vivo*, adult human experimental data published by Bader et. al [48] (Appendix A).

Two model parameters require calibration, the tissue bulk modulus, κ, and shear modulus, μ. Inputs parameters to the calibration include hydrostatic interstitial fluid pressure (p_0), initial tissue solid volume fraction (φ^s), expansion ratio ($\boldsymbol{\eta}$), and tissue thickness (H). Ranges for hydrostatic fluid pressure and initial tissue solid volume fraction were found in literature (Table 7). The expansion ratio was allowed to vary from 0-0.5, as is consistent with other pressure ulcer models that take into consideration the Poisson-like effect [59].

Table 7. Mean (range) tissue parameters required for model calibration.

Parameter	Mean (Range)	Reference
Dermal Thickness [mm]	1.1 (0.9-1.3) 1.2 (0.625-1.69)	[199] [200]
Hypodermal Thickness [mm]	3.7 (1.4-8.9) 5.1 (3.55-6.66)	[201] [202]
Interstitial Fluid Pressure [Pa]	-40 -120 (-266-266)	[203] [204] [205]
Initial Solid Volume Fraction	(0.096-0.166) 0.17	[206] [207]

4.3.2 Sensitivity Analysis

A Cotter's sensitivity analysis was used to determine the relative sensitivity of the model output (shear modulus) to respective inputs. The methodology followed that of section 3.6.

4.4 Results

4.4.1 Model Calibration

Two compressible models were calibrated: one with a uniform strain input (CNH-U) and a second with strain of the form of Hertz contact for a rigid, cylindrical indenter and an elastic half-space (CNH-Hertz). In the case of the Hertz contact form, the strain profile at the tissue surface was assumed to be equivalent to the pressure profile for elastic Hertz contact. For comparison, the previously calibrated incompressible linear elastic (ILE) and incompressible neo-hookean (INH) models are also included.

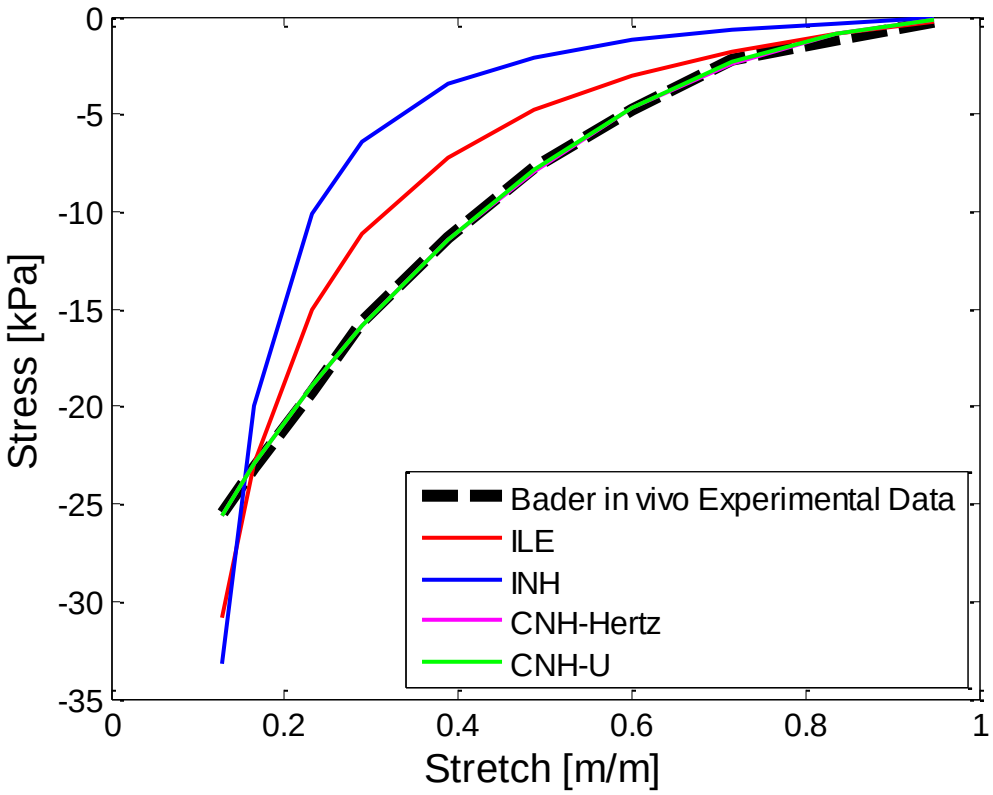

Figure 20. Calibrated models demonstrate a distinct difference between the predictive capabilities of incompressible versus compressible models of *in vivo* tissue deformation. ILE provides limited predictive capabilities at low strains, while INH fails to predict deformation all together. CNH-U and CNH-Hertz predict the deformation well, although RMSE was minimized slightly more with CNH-Hertz (0.209) than CNH-U (0.210).

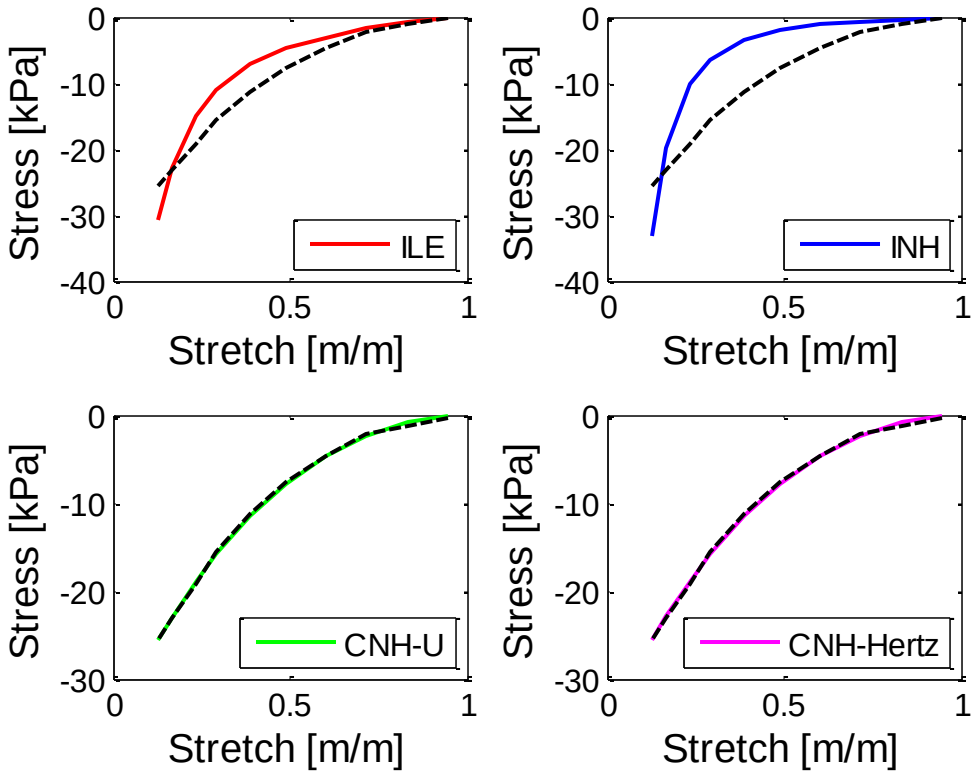

Figure 21. Calibrated models demonstrate a distinct difference between the predictive capabilities of incompressible versus compressible models of *in vivo* tissue deformation. ILE provides limited predictive capabilities at low strains, while INH fails to predict deformation all together. CNH-U and CNH-Hertz predict the deformation well, although RMSE was minimized slightly more with CNH-Hertz (0.209) than CNH-U (0.210).

Table 8. Calibration results for incompressible linear elastic (ILE), incompressible neo-hookean (INH), compressible neo-hookean with uniform strain (CNH-U), and compressible neo-hookean with Hertzian-type strain (CNH-Hertz).

Parameter	ILE	INH	CNH-U	CNH-Hertz
Expansion Ratio	NA	NA	0.5	0.5
Aggregate Modulus [kPa]	31.65	--	--	--
Bulk Modulus [kPa]	--	--	230	227.7
Shear Modulus [kPa]	--	3.83	0.66	1.04
RMSE [kPa]	3.091	5.910	0.210	0.209

4.4.2 Sensitivity Analysis

The expansion ratio (η) was found to be the most sensitive input parameter for each different strain profile model. For the CNU-Hertz model, the tissue thickness (H), an input unique to this model, was nearly a sensitive parameter.

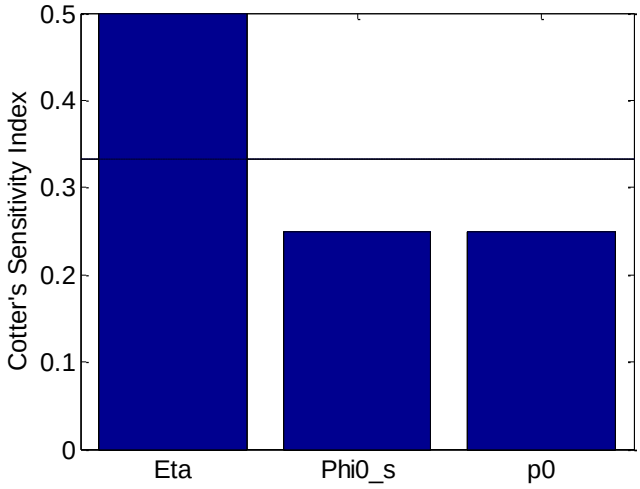

Figure 22. Cotter's sensitivity indices for the CNU-U calibration model with shear modulus (μ) as the output parameter. The dashed line represent $1/n_p$ and any sensitivity index that falls above this line is considered a sensitive parameter. Expansion ratio ($\boldsymbol{\eta}$) is the only sensitive parameter.

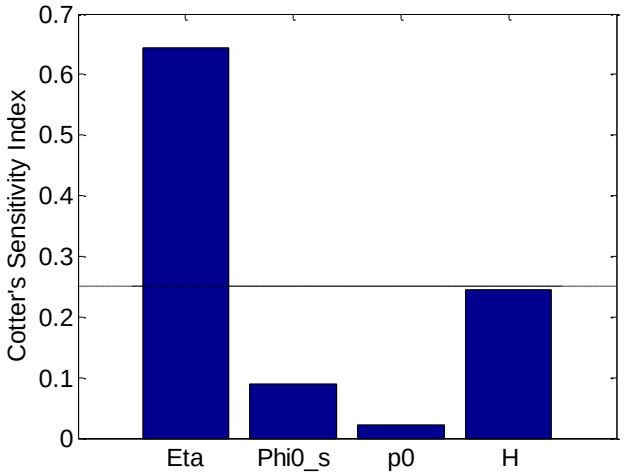

Figure 23. Cotter's sensitivity indices for the CNU-Hertz calibration model with shear modulus (μ) as the output parameter. The dashed line represent $1/n_p$ and any sensitivity index that falls above this line is considered a sensitive parameter. Expansion ratio ($\boldsymbol{\eta}$) is the only sensitive parameter; however, the skin thickness (H), an input unique to the Hertz model, is nearly a sensitive parameter.

4.5 Discussion

The CNU-Hertz model calibration results for shear modulus were on the same order of magnitude as in literature; whereas, the CNU-U fell just one order of magnitude below literature values. The calibrated bulk modulus was much greater than the shear modulus, which is expected for highly deformable soft tissue [176].

The expansion ratio ($\boldsymbol{\eta}$), which models Poisson-like effects in the tissue, is the most sensitive parameter in both models. Poisson ratio is the ratio of transverse to axial strain for small, linear elastic deformations. Poisson ratios are typically between 0-0.5, with a perfectly incompressible material having a Poisson ratio of 0.5. Soft tissues characteristically exhibit large, non-linear deformations. Therefore, the expansion ratio ($\boldsymbol{\eta}$) is incorporated to model Poisson-like effects during large, non-linear tissue deformation. Neither Poisson ratio nor expansion ratio are well understood for skin tissue. However, Poisson ratios between 0.25-0.85 have been reported despite skin deformation failing outside of the small, linear deformation requirement of Poisson [208]. Due to both the CNU-U and CNU-Hertz sensitivity to expansion ratio, additional experimental data would be ideal to better elicit the value for the expansion ratio characteristic of large, non-linear soft tissue deformations.

Unique to the CNU-Hertz model is dependence on and apparent sensitivity to skin tissue thickness (H). Skinfold thickness is extremely age, gender, and site specific [58]. Skinfold measurements can be taken many different ways, including via calipers, x-ray imaging, or ultrasound imaging. The most easily accessible and referenced skinfold measurement is taken via Harpenden calipers, in which an assumed uniform pressure is applied as the calipers grip a skinfold. The resulting measurement is halved to yield

skinfold thickness that includes epidermal, dermal, and hypodermal layers. Harpenden calipers offer a non-invasive, economical measurement of skin tissue thickness. But given the sensitivity of the model to skin thickness and the site, age, and gender dependence of skin thickness, measurements acquired via imaging analysis at the PrU location might be preferred. Moreover, with stress held constant, strain is underestimated with a thicker tissue. Inaccuracies in the tissue thickness parameter could lead to direct inaccuracies in stress-strain estimations.

Data for the bulk modulus and shear modulus of neonatal human tissue is non-existent within literature. This is a setback in predictive modeling of neonatal tissues which could benefit not only inform models of neonatal PrUs, but also modeling of neonatal transepidermal water loss and skin barrier function, another critical issue in neonatal care. It is difficult to estimate a range for the neonatal bulk and shear modulus since the models were calibrated with adult tissue experimental data. However, it is known that the initial solid volume fraction (φ_0^s) of neonates is lower than adults [206]. Likewise, at birth, neonates have three times more interstitial fluid than adults resulting in higher hydrostatic pressure (p_0) than the adult population [209]. When the models are re-calibrated using the low value for (φ_0^s) and the high value for intitial interstitial fluid pressure (p_0), the bulk modulus increases and the shear modulus decreases. Therefore, the calibrated tissue properties reported in this chapter represent the high value of bulk and shear modulus within the neonatal population.

The assumption that muscle is a rigid boundary to adipose tissue is a limitation of the model. Although muscle stiffness is much greater than adipose, it is still undergoing some level of tissue deformation. Further iterations of this model would benefit from the inclusion of muscle in the tissue thickness parameter.

CHAPTER 5. PREDICTIVE CAPABILITIES FOR THE NEONATAL POPULATION

5.1 Introduction

Accurately determining the stress profile within cutaneous and subcutaneous tissue plays an important role in understanding PrU etiology. Given an appropriate set of input parameters, a known stress distribution may be used to analytically estimate the local tissue deformation (strain). Several investigators have isolated tissue deformation as a critical factor in PrU etiology [3,176,210-212]. Tissue deformation contributes to cell deformation and death, capillary occlusion, and an inhibition of interstitial fluid flow (impaired nutrient transport and lymph drainage), among other factors.

Tissue deformation has been determined using different methods. Reddy [213] experimentally estimated linearized, 2D tissue deformation in the buttocks using a PVC gel (skin) covering a wooden sphere (ischium bone). Similarly, Sacks [66] experimentally estimated skin deformation under a rigid, cylindrical flat ended indenter. More recently, tissue deformation has typically been investigated using expensive MRI-based experiments in conjunction with complex FEA models [180,183,192,214,215]. In this chapter a two dimensional, hyperelastic, compressible analytical model is developed for the prediction of tissue stress profiles and ultimately tissue strain.

5.2 Theory

In order to predict the mechano-physiological processes of load-bearing human cutaneous and subcutaneous tissue, the mixture theory based model developed in Chapter 4 is utilized. The model assumes the tissue to be compressible, homogeneous, and isotropic. The tissue is subjected to non-homogeneous loading of two forms, namely axisymmetric spherical loading (occipital PrU model) and plane strain cylindrical loading (oxygen cannula PrU) (Figure 24).

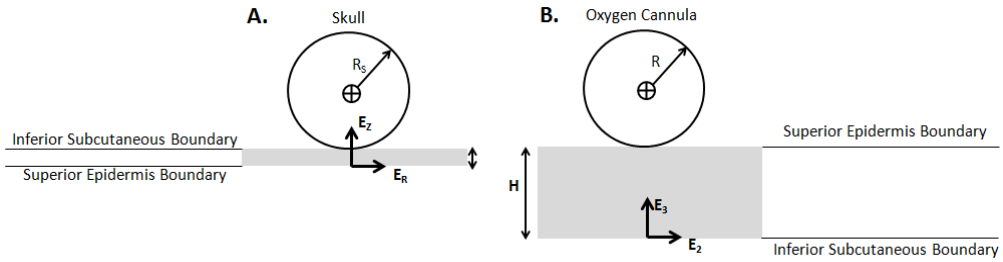

Figure 24. Schematic of PrU prediction case studies. A.) Occipital PrUs modeled by an axisymmetric sphere in contact with an elastic half-space of cutaneous and subcutaneous tissue. B.) Oxygen cannula PrUs modeled by a plan strain cylinder parallel to an elastic half space of cutaneous and subcutaneous tissue. Notice the change in skin orientation required for modeling Case A versus Case B.

5.2.1 Axisymmetric Spherical Loading

For a case study of neonatal occipital PrUs, the occiput was modeled as an axisymmetric, rigid spherical indenter lying on an elastic half-space of tissue. The contact area radius was presumed to be small enough that the radius of curvature of the skin on the skull is negligible. The strain profile at the loading surface was described using three different models, a geometrical circular segment, Gaussian, and Hertz – type profile.

The solid particle position, x_i^s, can be described in terms of the reference configuration, X_i^s, such that

$$\begin{cases} {x_1}^s = {X_1}^s - \eta\varepsilon_3 {X_1}^s \\ {x_2}^s = {X_2}^s - \eta\varepsilon_3 {X_2}^s \\ {x_3}^s = {X_3}^s + \varepsilon_3 {X_3}^s \end{cases} \quad (5.1\text{-}5.3)$$

where $\boldsymbol{\eta}$ is the expansion ratio and ε_3 is the strain profile. Applying a coordinate transformation for the axisymmetric assumption results in a solid particle position described by

$$\begin{cases} r^s = R^s - \eta\varepsilon_Z R^s \\ \theta^s = \Theta^s \\ z^s = Z^s + \varepsilon_Z Z^s \end{cases} . \quad (5.4\text{-}5.6)$$

The rate of deformation tensor in cylindrical coordinates is then given by

$$\underline{F}^s = \underline{I} + \nabla u = \begin{bmatrix} 1 + \frac{\partial u_R}{\partial R} & 0 & \frac{\partial u_R}{\partial Z} \\ 0 & 1 + \frac{U_R}{R} & 0 \\ \frac{\partial u_Z}{\partial R} & 0 & 1 + \frac{\partial u_Z}{\partial Z} \end{bmatrix} \quad (5.7)$$

resulting in the following equation for Cauchy stress in the loading direction

$$T_{ZZ}^T = -p + \varphi^s \kappa J^s (J^s - 1) + \frac{\varphi^s \mu}{J^s} \left\{ \left[(1 + \frac{\partial u_Z}{\partial Z})^2 + (\frac{\partial u_Z}{\partial R})^2 \right] - \frac{1}{3} \left[(1 + \frac{\partial u_R}{\partial R})^2 + (1 + \frac{U_R}{R})^2 + (\frac{\partial u_Z}{\partial R})^2 + (1 + \frac{\partial u_Z}{\partial Z})^2 \right] \right\}. \quad (5.8)$$

The final form of the equation depends on the selected format for the strain profile.

5.2.1.1 Geometrical Circular Segment Strain Profile

The strain profile induced by the occiput on the surface of the skin was modeled using the axisymmetric geometric equations for the arc of circular segment.

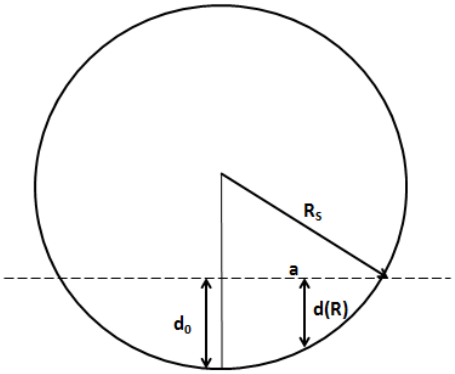

Figure 25. Geometric relations for tissue deformation d(R) due to the arc of a circular segment.

The derived strain profile is a function of tissue thickness (*H*), radius of the sphere (R_S), position in *R*, and maximum deformation (d_0) such that

$$\varepsilon_Z = -\frac{d(R)}{H} \tag{5.9}$$

$$d(R) = \sqrt{R_S^2 - R^2} - \sqrt{R_S^2 - a^2} \tag{5.10}$$

$$a^2 = R_S^2 - (R_s - d_0)^2 \tag{5.11}$$

$$d_0 = d(R = 0). \tag{5.12}$$

5.2.1.2 Gaussian Strain Profile

The strain profile on the surface of the skin was also modeled using a Gaussian distribution, such that

$$\varepsilon_Z = -\gamma e^{(\frac{-R^2}{2\sigma^2})} \tag{5.13}$$

$$\gamma = -\varepsilon_Z(R = 0). \tag{5.14}$$

The spread of the Gaussian distribution (σ) was determined by a curve fit with the preceeding circular segment strain profile.

5.2.1.3 Hertzian – Type Strain Profile

The strain profile on the surface of the skin was finally modeled using a Hertz – type profile. As such, the strain profile at the surface was assumed to have same profile as Hertz theory pressure of the form

$$\varepsilon_Z = -\gamma\sqrt{(1-\frac{R^2}{a^2})} \tag{5.15}$$

$$\gamma = -\varepsilon_Z(R=0) \tag{5.16}$$

where the contact area radius is described by

$$a^2 = R_s^2 - (R_s - \gamma H)^2. \tag{5.17}$$

5.2.2 Plan Strain Cylindrical Loading

For a case study of neonatal oxygen cannula PrUs, the oxygen cannula was modeled as rigid cylinder lying on an elastic half-space of tissue in plane strain. The deformation of the cannula itself was assumed negligible. The strain profile at the loading surface was described using three different models, a geometrical circular segment, Gaussian, and Hertz – type profile.

The solid particle position, x_i^s, can be described in terms of the reference configuration, X_i^s, such that

$$\begin{cases} {x_1}^s = {X_1}^s \\ {x_2}^s = {X_2}^s - \eta\varepsilon_3{X_2}^s \\ {x_3}^s = {X_3}^s + \varepsilon_3{X_3}^s \end{cases} \tag{5.18-5.20}$$

where $\boldsymbol{\eta}$ is the expansion ratio and ε_3 is the strain profile. The rate of deformation tensor is then given by

$$\underline{F}^s = \frac{x_i^s}{X_A^s} = \begin{bmatrix} 1 & 0 & 0 \\ 0 & \frac{x_2^s}{X_2^s} & 0 \\ 0 & \frac{x_3^s}{X_2^s} & \frac{x_3^s}{X_3^s} \end{bmatrix} \tag{5.21}$$

resulting in the following equation for Cauchy stress in the loading direction

$$T_{33}^T = -p + \varphi^s \kappa J^s (J^s - 1) + \frac{\varphi^s \mu}{J^s}\left\{\left[\left(\frac{x_3^s}{X_2^s}\right)^2 + \left(\frac{x_3^s}{X_3^s}\right)^2\right] - \frac{1}{3}\left[1 + \left(\frac{x_2^s}{X_2^s}\right)^2 + \left(\frac{x_3^s}{X_2^s}\right)^2 + \left(\frac{x_3^s}{X_3^s}\right)^2\right]\right\}. \tag{5.22}$$

The final form of the equation depends on the selected format for the strain profile.

5.2.2.1 Geometrical Circular Segment Strain Profile

The strain profile induced by an oxygen cannula on the surface of the skin was modeled using the plane strain geometric equations for the arc of circular segment.

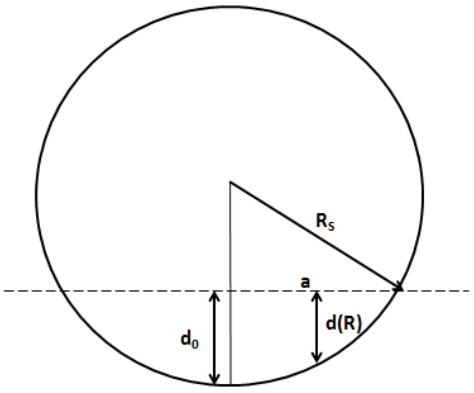

Figure 26. The geometric relationships between sphere radius (R_s), contact radius (a), and maximum indentation (d_o) are used to develop the geometric circular segment strain profile function.

The derived strain profile is a function of tissue thickness (H), radius of the sphere (R_s), position in X_2, and maximum deformation (d_0) such that

$$\varepsilon_3 = -\frac{d(X_2)}{H} \tag{5.23}$$

$$d(X_2) = \sqrt{R_S^2 - X_2^2} - \sqrt{R_S^2 - a^2} \tag{5.24}$$

$$a^2 = R_S^2 - (R_s - d_0)^2 \tag{5.25}$$

$$d_0 = d(X_2 = 0). \tag{5.26}$$

5.2.2.2 Gaussian Strain Profile

The strain profile induced by an oxygen cannula on the surface of the skin was also modeled using a Gaussian distribution, such that

$$\varepsilon_3 = -\gamma e^{(\frac{-X_2^2}{2\sigma^2})} \tag{5.27}$$

$$\gamma = -\varepsilon_3(X_2 = 0). \tag{5.28}$$

The spread of the Gaussian distribution (σ) was determined by a curve fit with the preceeding circular segment strain profile.

5.2.2.3 Hertzian – Type Strain Profile

The strain profile induced by an oxygen cannula on the surface of the skin was finally modeled using a Hertz – type profile. As such, the strain profile at the surface was assumed to have same profile as Hertz theory pressure of the form

$$\varepsilon_3 = -\gamma\sqrt{(1 - \frac{X_2^2}{a^2})} \tag{5.29}$$

$$\gamma = -\varepsilon_3(X_2 = 0) \tag{5.30}$$

where the contact area radius is described by

$$a^2 = R_s^2 - (R_s - \gamma H)^2. \tag{5.31}$$

Table 9. Four different functions were used to model the strain profile of the skin tissue at the loading surface, including a uniform strain profile, an arc of a circular segment strain profile, a Gaussian distribution strain profile, and a Hertz-type contact profile in which the strain profile at the tissue surface was assumed to be similar to the pressure profile in Hertz contact between a rigid body and an elastic half space.

Strain Profile	Function
Uniform	$\varepsilon_Z = -\gamma$
Arc of a Circular Segment	$\varepsilon_z = -\frac{\sqrt{R_S^2 - R^2} - \sqrt{R_S^2 - a^2}}{H}$
Gaussian Distribution	$\varepsilon_Z = -\gamma e^{\left(\frac{-R^2}{2\sigma^2}\right)}$
Hertz Contact	$\varepsilon_z = -\gamma\sqrt{\left(1 - \frac{R^2}{a^2}\right)}$

5.3 Methods

5.3.1 Predictive Models of Occipital PrUs

Stress profile predictions for occipital PrUs (O-PrUs) were made using single point support surface – occiput interface pressure data measurements acquired from literature for pre-term and term neonate groups (Table 10). The single point stress measurement is approximated as the maximum stress value corresponding to the center axis of deformation ($R_s = 0$). Input parameters required for the prediction are tissue thickness (H), sphere radius (R_s), bulk modulus (κ), shear modulus (μ), and initial solid volume fraction (φ_0^s). Average skin thickness for pre-term and term neonates was pulled directly from literature (Table 10). Average sphere radius was approximated from occipital frontal circumference data for pre-term and term neonates (Table 12). Bulk

modulus and shear modulus were acquired from the CNH-Hertz calibration results. Average initial solid volume fraction was assumed to be the same between each group.

Table 10. Mean (range) support surface - occiput interface pressure for pre-term and term neonates.

GA (wks)	Mean (Range) Interface Pressure [mmHg]	Support Surface Type	Ref
Pre-Term (GA <37 wks)	31	Standard crib mattress + foam overlay	[152]
	37.5	Standard crib mattress + gel donut	[152]
	49.8	Standard crib mattress + gel overlay	[152]
	50.1	Standard crib mattress + water pillow	[152]
	86.9	Standard crib mattress	[152]
	15	Powered mattress	[175]
Term (GA > 37 wks)	32 (22-58)	Gel-E-Donut Pillow	[216]
	59	2-4 inch convoluted foam	[153]
	26 (13-44)	Delta foam overlay + Gel-E-Donut pillow	[216]
	61 (36-91)	Standard crib mattress	[216]
	32 (13-59)	Efica low-air-loss bed	[216]

Table 11. Mean (range) skin fold thickness measurements for pre-term and term neonates. Skin fold measurements include epidermis, dermis, and hypodermis.

GA (wks)	Anatomical Location	Gender	Mean (Range) Skin Fold Thickness [mm]	Ref
Pre-Term (GA < 37wks)	Upper Arm	Male	4.08	[217]
	Upper Arm	Female	3.99	[217]
	Tricep	Male	4.5	[218]
	Tricep	Female	4.39	[218]
	Subscapula	Male	4.53	[218]
	Subscapula	Female	4.81	[218]
Term (37 wks > GA > 40 wks)	Subscapula	Male	4.26(2.41-6.11)	[219]
	Subscapula	Female	4.59(2.69-6.51)	[219]
	Tricep	Male	4.12(2.47-5.75)	[219]
	Tricep	Female	4.35(2.76-5.93)	[219]
	Upper Arm	Male	(3.98-4.63)	[217]
	Upper Arm	Female	(4.82-4.98)	[217]
	Tricep	Male	4.68	[218]
	Tricep	Female	4.9	[218]
	Subscapula	Male	4.96	[218]l
	Subscapula	Female	5.53	[218]
	Tricep	Both	4.03(2.44-5.78)	[220]
	Subscapula	Both	4.24(2.33-6.12)	[220]

Table 12. Mean (range) occipital frontal circumference of pre-term and term neonates used to determine approximate skull radius.

GA (wks)	Mean (Range) Occipital Frontal Circumference [cm]	Ref.
Pre-Term (<37 wks)	20.7 (18.3-23.1)	[170]
	20.9 (18.5-23.3)	[170]
	21.1 (18.7-23.5)	[170]
	21.3 (18.9-23.7)	[170]
	(19.0-34.7)	[170]
	(19.2-35.0)	[170]
	(19.4-35.3)	[170]
	(19.6-35.6)	[170]
Term (>37 wks)	(30.3-36.5)	[170]
	(30.7-36.7)	[170]
	(31.0-37.1)	[170]
	(31.3-37.4)	[170]
	35.6 (34.4-36.8)	[172]
	35.7 (34.4-37)	[172]
	34.6 (32.7-37)	[173]
	35.7 (33-37.9)	[173]

Using the inputs described, stress distributions for O-PrUs were investigated for each of the strain profile models (Figure 27). Outputs from the models were stress distribution across both tissue radius (width) and depth as well as maximum strain.

5.3.2 Predictive Oxygen Cannula PrU Models

Unlike O-PrU models, skin surface – oxygen cannula interface pressure is not readily available. However, a large majority of OC-PrUs occur due to prolonged prone positioning on a cannula. Therefore, the maximum stress may be estimated as the force

(neonatal weight) per area (neonatal body surface area). Neonatal body surface area is estimated using the standardized neonatal body surface area equation

$$BSA = (W^{0.5378})x(L^{0.3964})x(0.024265) \quad (5.32)$$

where W is weight in kilograms, L is length in centimeters, and BSA is body surface area in m^2 [221,222]. Averages for weight and length for both pre-term and term neonates are readily available in literature (Table 13). Input parameters required for the prediction are tissue thickness (H), cannula radius (R_s), bulk modulus (κ), shear modulus (μ), and initial solid volume fraction (φ_0^s). Average skin thickness for pre-term and term neonates was pulled directly from literature (Table 10). Cannula diameters (R_s) were taken to be 3mm for pre-term neonates and 3.7mm for term neonates [223,224]. Bulk modulus and shear modulus were acquired from the CNH-Hertz calibration results. Average initial solid volume fraction was assumed to be the same between each group.

Table 13. Mean (range) birth mass and height for pre-term and term neonates.

GA (wks)	Mean (Range) Birth Mass (kg)	Mean (Range) Birth Height (cm)	Ref.
Pre-Term (<37 wks)	(340-3.371) (1.75-2.7)	(25.2-50.2)	[170] [171]
Term (>37 wks)	(1.979-4.140) (3.0-3.65) (4.055-4.068) 3.453	(43.3-53.2) (44.7-57.1) 52.9	[170] [171] [172] [174]

Using the inputs previously described, Stress distributions for O-PrUs were investigated for each of the strain profile models (Figure 27). Outputs from the models

were stress distribution across both tissue radius (width) and depth as well as maximum strain.

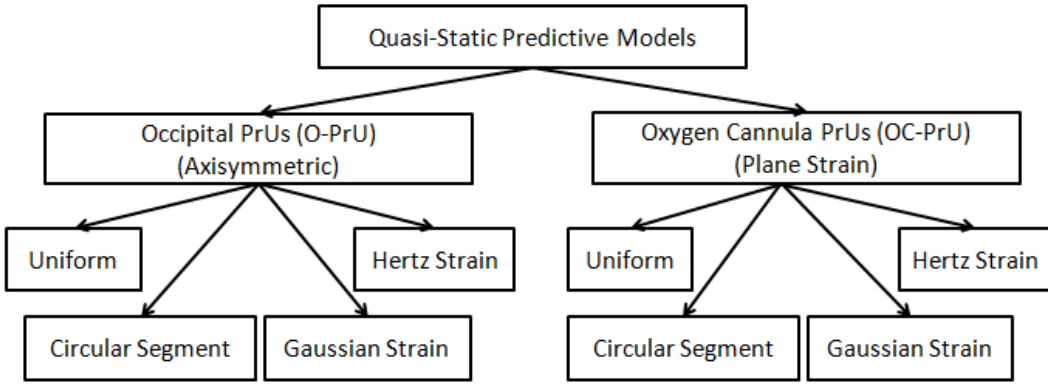

Figure 27. Quasi-static predictive model progression. The same model progression was completed for both pre-term and term neonates.

5.3.3 Capillary Occlusion Analysis

Capillary occlusion was investigated by observing blood volume fractions changes across the range of interface pressure data available for the case of O-PrUs.

5.3.4 Sensitivity Analysis

A Cotter's sensitivity analysis was used to determine the relative sensitivity of the model output (maximum stress) to respective inputs. The methodology followed that of section 3.6.

5.4 Results

5.4.1 Prediction of Occipital Interface Pressure Distribution

The geometric circular segment, Gaussian, and Hertz strain input models predicted the maximum stress within 0.2% for both pre-term and term groups. In both

pre-term and term groups, the Gaussian model predicted stress with the least error at 0% and 0.02%, respectively. Based on the minimized error, the Gaussian model is taken to be the most accurate prediction of maximum strain. Therefore, the maximum strain in the pre-term and term groups was predicted as 0.4788 m/m and 0.4835 m/m, respectively.

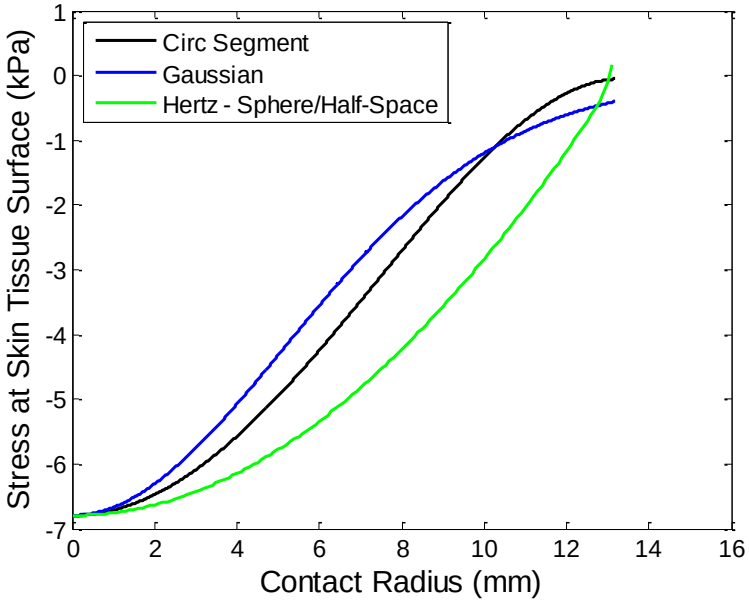

Figure 28. Comparison of predicted stress profile at the support surface- occiput interface for pre-term neonates in supine lying position.

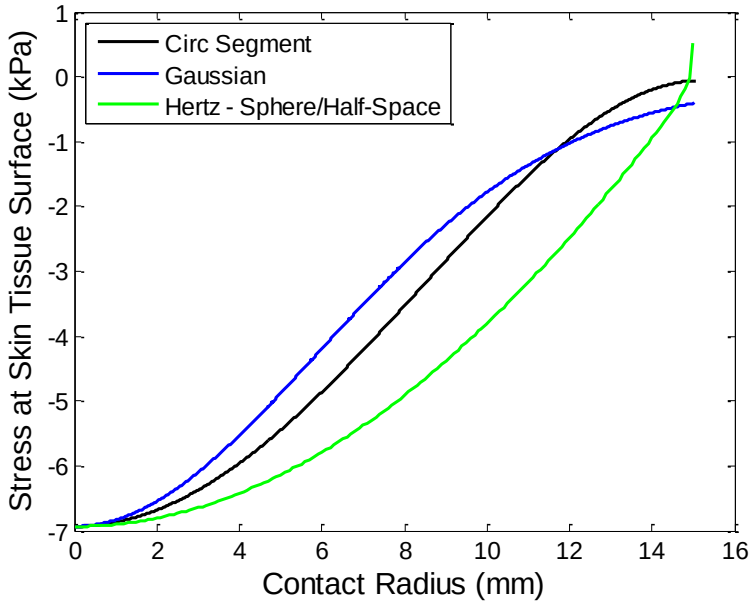

Figure 29. Comparison of predicted stress profile at the support surface- occiput interface for term neonates in supine lying position.

Since the compressible form of the solid constitutive equation used in these models is dependent on the deviatoric component of the left Cauchy-Green tensor, which in turn is dependent on the F_{ZR} component of the deformation gradient, the stress profile throughout the depth of the tissue may also be computed. Variations in stress throughout tissue depth are subtle, but present. Since the pre-term and term models are similar in shape, the term models are presented as representative of all O-PrU models.

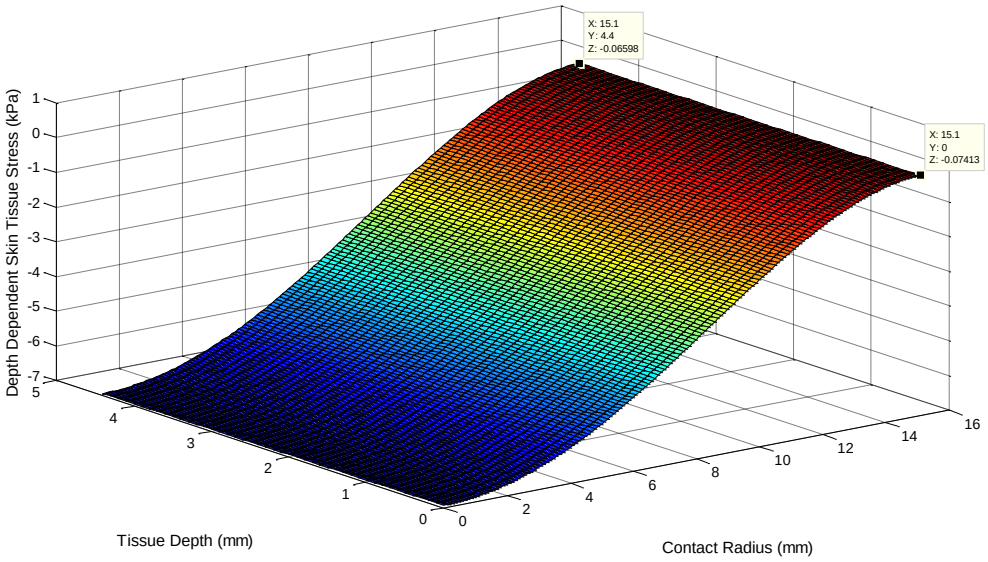

Figure 30. Tissue stress variation with radius and tissue thickness in term neonates using a geometrical circular segment strain distribution. At a tissue depth of Z = 0 and radius R = contact radius, T_{ZZ} = -74.13 Pa. At a tissue depth of Z = H and radius R = contact radius, T_{ZZ} = -65.98 Pa.

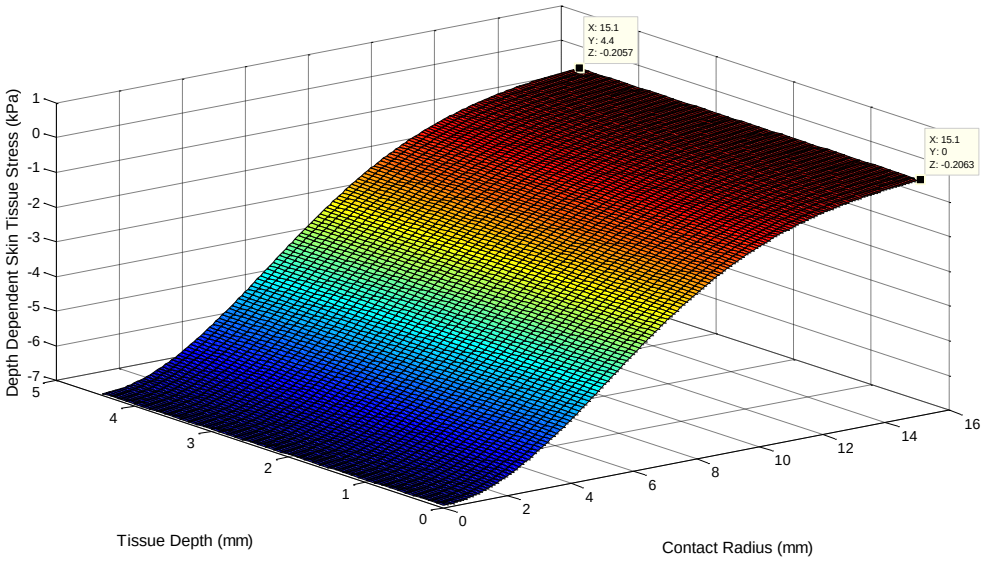

Figure 31. Tissue stress variation with radius and tissue thickness in term neonates using a Gaussian strain distribution. At a tissue depth of Z = 0 and radius R = contact radius, T_{ZZ} = -206.3 Pa. At a tissue depth of Z = H and radius R = contact radius, T_{ZZ} = -205.7 Pa.

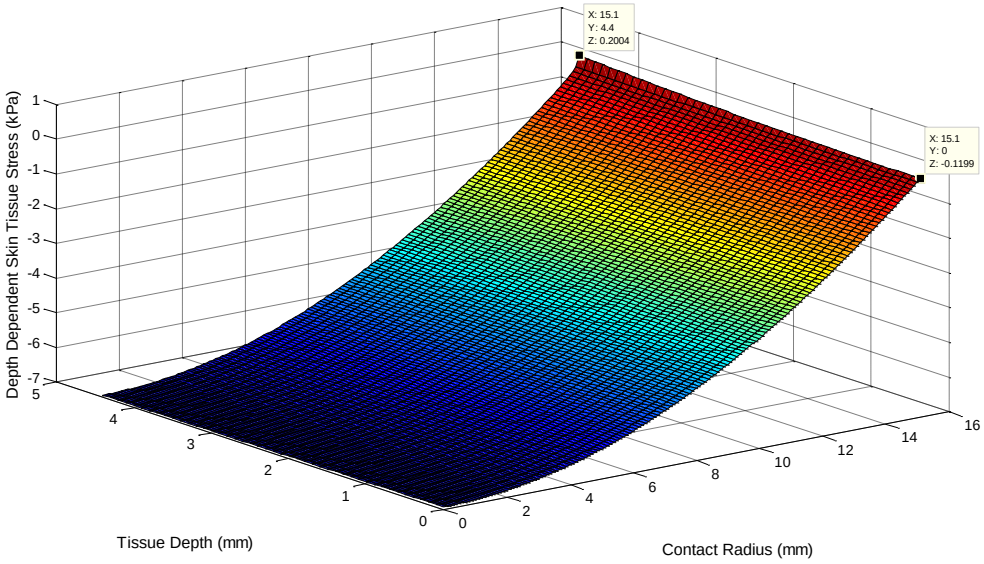

Figure 32. Tissue stress variation with radius and tissue thickness in term neonates using a Hertz strain distribution. At a tissue depth of Z = 0 and radius R = contact radius, T_{ZZ} = -119.9 Pa. At a tissue depth of Z = H and radius R = contact radius, T_{ZZ} = -200.4 Pa. Higher tissue stress at Z = H demonstrates the singularity contained within the flawed model that will be discussed in a later section.

5.4.2 Prediction Oxygen Cannula Interface Pressure Distribution

The geometric circular segment, Gaussian, and Hertz strain input models predicted the maximum stress within 4.0% for both pre-term and term groups. In both pre-term and term groups, the Gaussian model predicted stress with the least error at 0.69% and 0.38%, respectively. Based on the minimized error, the Gaussian model is taken to be the most accurate prediction of maximum strain. Therefore, the maximum strain in the pre-term and term groups was predicted as 0.0023 m/m and 0.0030 m/m, respectively.

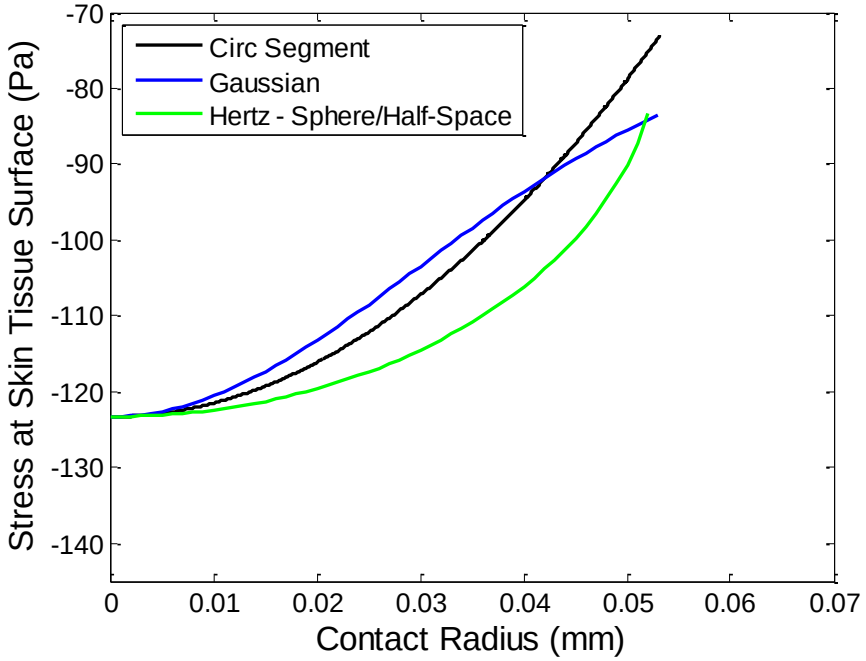

Figure 33. Comparison of predicted stress profile at the tissue surface-oxygen cannula interface for pre-term neonates in supine lying position.

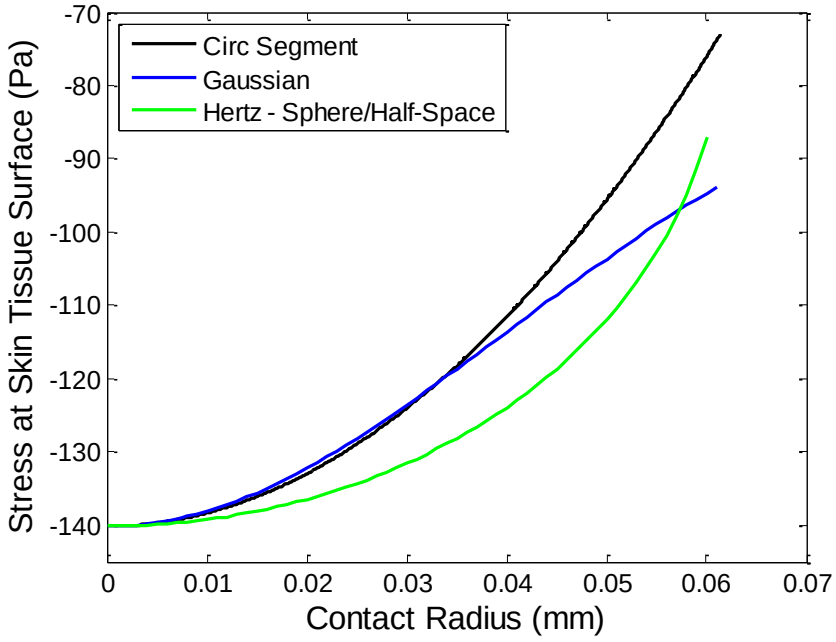

Figure 34. Comparison of predicted stress profile at the tissue surface-oxygen cannula interface for term neonates in supine lying position.

As with the O-PrU models, since the compressible form of the solid constitutive equation used in these models is dependent on the deviatoric component of the left Cauchy-Green tensor, which in turn is dependent on the F_{32} component of the deformation gradient, the stress profile throughout the depth of the tissue may also be computed. Variations in stress throughout tissue depth are subtle, but present. Since the pre-term and term models are similar in shape, the term models are presented as representative of all OC-PrU models.

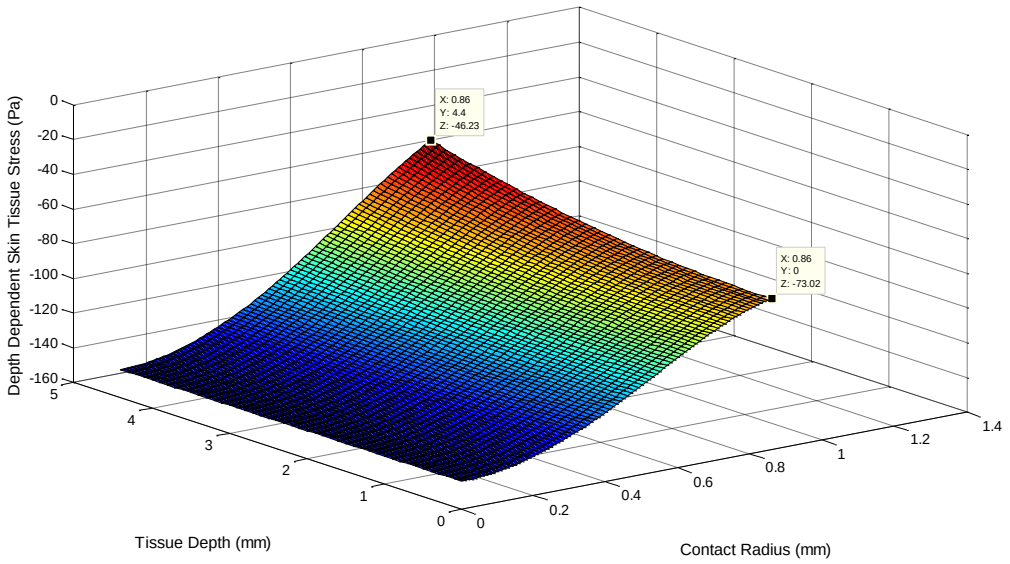

Figure 35. Tissue stress variation with radius and tissue thickness in term neonates using a geometric circular segment strain distribution. At a tissue depth of Z = 0 and radius R = contact radius, T_{ZZ} = -73.02 Pa. At a tissue depth of Z = H and radius R = contact radius, T_{ZZ} = -46.23 Pa.

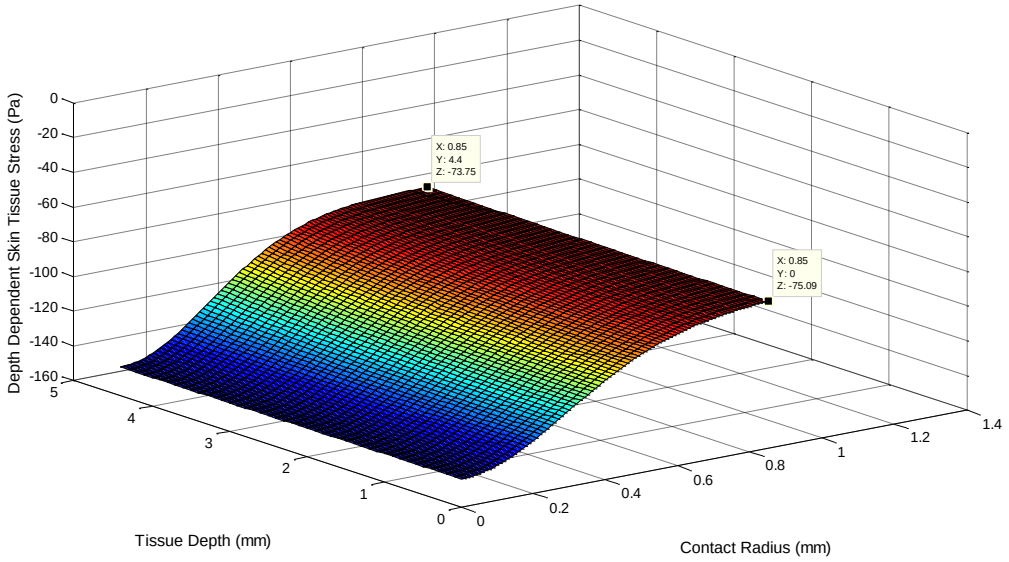

Figure 36. Tissue stress variation with radius and tissue thickness in term neonates using a Gaussian strain distribution. At a tissue depth of Z = 0 and radius R = contact radius, T_{ZZ} = -75.09 Pa. At a tissue depth of Z = H and radius R = contact radius, T_{ZZ} = -73.75 Pa.

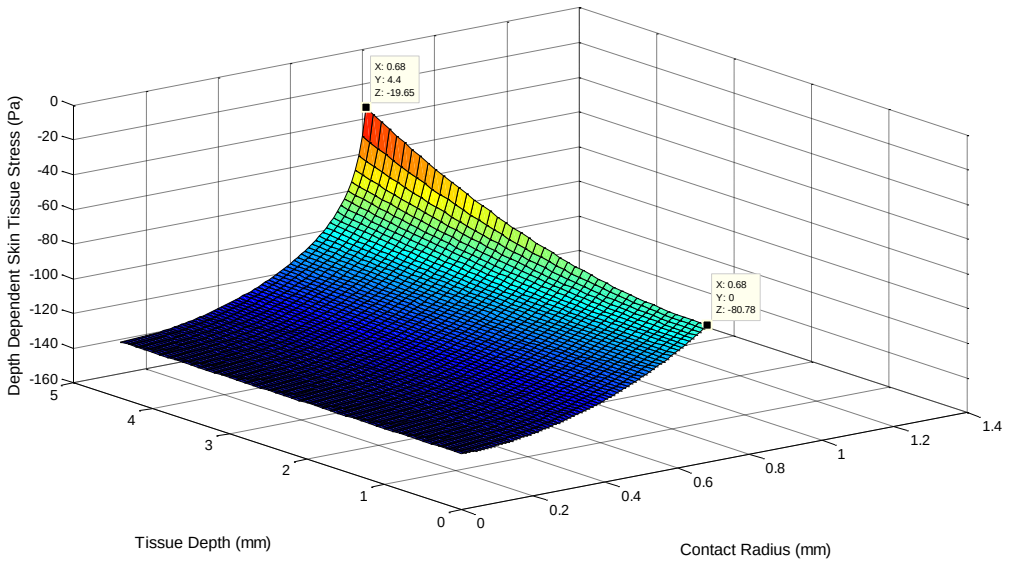

Figure 37. Tissue stress variation with radius and tissue thickness in term neonates using a Hertz strain distribution. At a tissue depth of Z = 0 and radius R = contact radius, T_{ZZ} = -80.78 Pa. At a tissue depth of Z = H and radius R = contact radius, T_{ZZ} = -19.65 Pa. The steep slope at Z = H demonstrates the singularity contained within the flawed model that will be discussed in a later section.

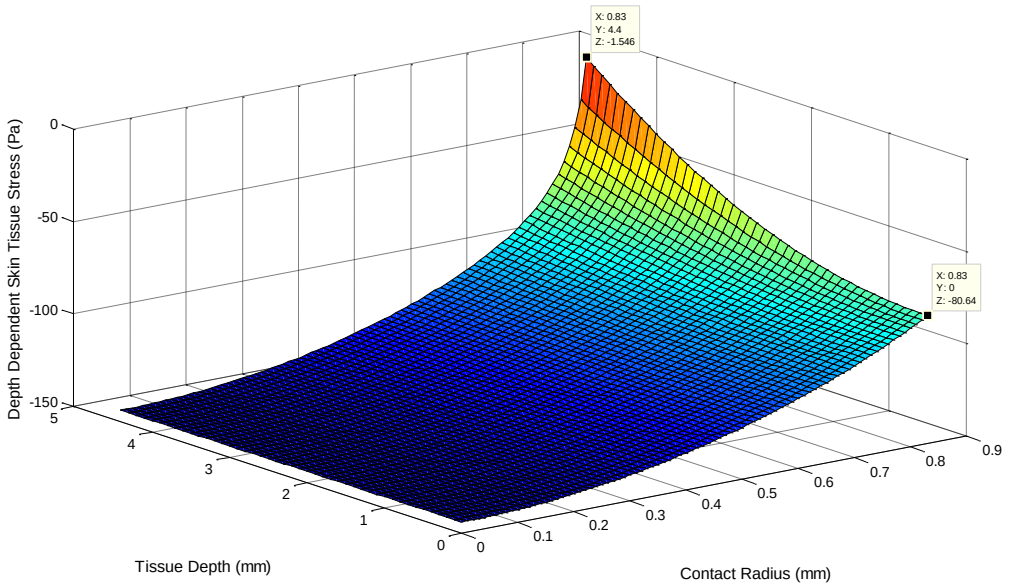

Figure 38. Depth dependence of quasi-static tissue stress under oxygen cannula in term neonates using a Hertz – Parallel Axis Cylinder contact strain distribution.

5.4.3 Sensitivity Analysis

5.4.3.1 Occipital Pressure Ulcer Model

The initial hydrostatic tissue pressure (p_0) and initial solid volume fraction (φ_0^S) were found to be the most sensitive parameters in the geometric circular segment, Gauss, and Hertz models. Although not always above the reference line, the bulk modulus (κ) and expansion coefficient ($\boldsymbol{\eta}$) were nearly sensitive in each model as well. Sphere radius (R_s) and tissue thickness (H) were the least sensitive parameters in each model.

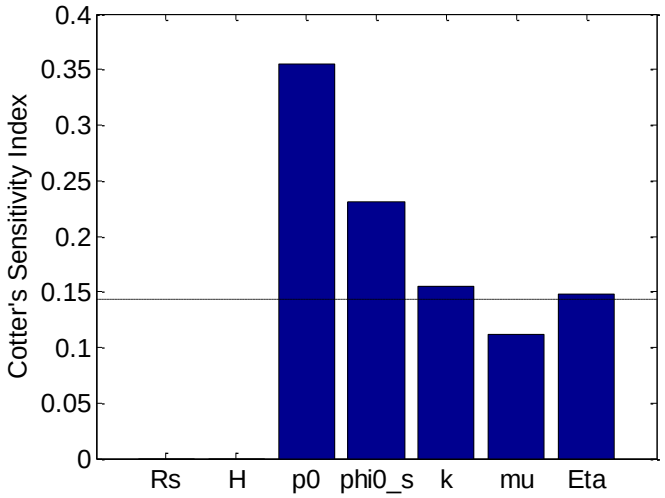

Figure 39. Cotter's sensitivity indices for the geometric circular segment occipital predictive model. The dashed line represent $1/n_p$ and any sensitivity index that falls above this line is considered a sensitive parameter. Initial hydrostatic tissue pressure (p_0), initial solid volume fraction (φ_0^s), bulk modulus (κ), and expansion ratio ($\boldsymbol{\eta}$) were determined to be sensitive parameters.

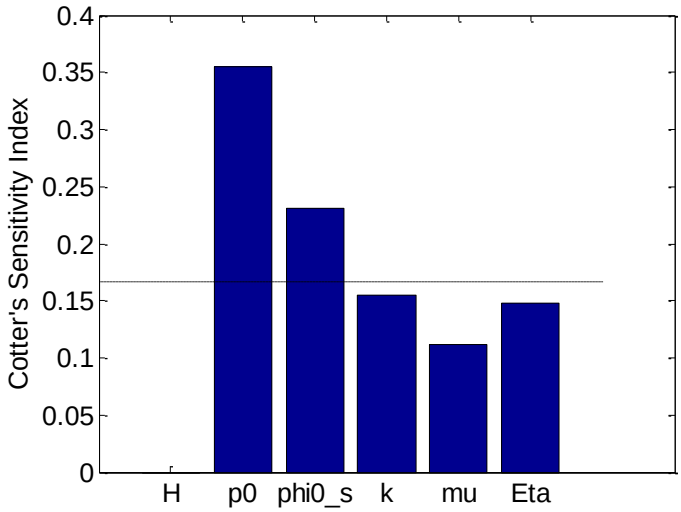

Figure 40. Cotter's sensitivity indices for the Gaussian occipital predictive model. The dashed line represent $1/n_p$ and any sensitivity index that falls above this line is considered a sensitive parameter. Initial hydrostatic tissue pressure (p_0) and initial solid volume fraction (φ_0^s) were determined to be sensitive parameters.

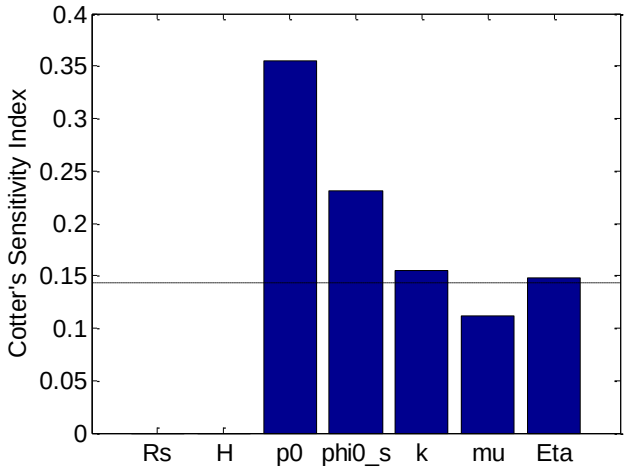

Figure 41. Cotter's sensitivity indices for the Hertz occipital predictive model. The dashed line represent $1/n_p$ and any sensitivity index that falls above this line is considered a sensitive parameter. Initial hydrostatic tissue pressure (p_0), initial solid volume fraction (φ_0^s), bulk modulus (κ), and expansion ratio ($\boldsymbol{\eta}$) were determined to be sensitive parameters.

5.4.3.1 Oxygen Cannula Pressure Ulcer Model

The initial hydrostatic tissue pressure (p_0), initial solid volume fraction(φ_0^s), and shear modulus (μ) were found to be the most sensitive parameters in the geometric circular segment, Gauss, and Hertz models.

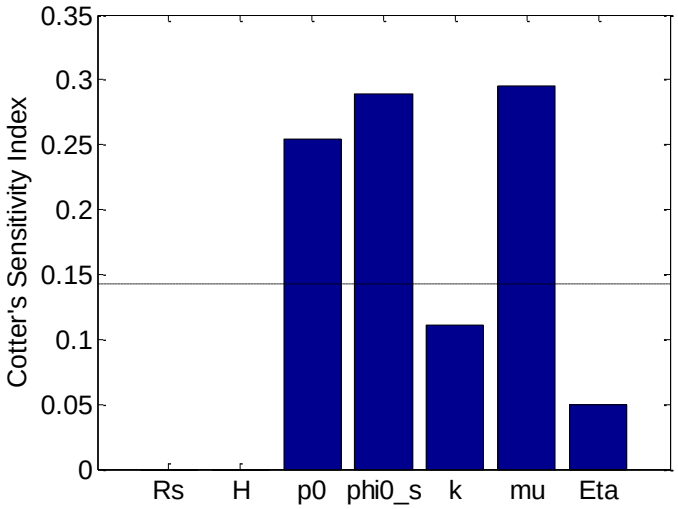

Figure 42. Cotter's sensitivity indices for the geometric circular segment oxygen cannula predictive model. The dashed line represent $1/n_p$ and any sensitivity index that falls above this line is considered a sensitive parameter. Initial hydrostatic tissue pressure (p_0), initial solid volume fraction (φ_0^s), and shear modulus (μ) were determined to be sensitive parameters.

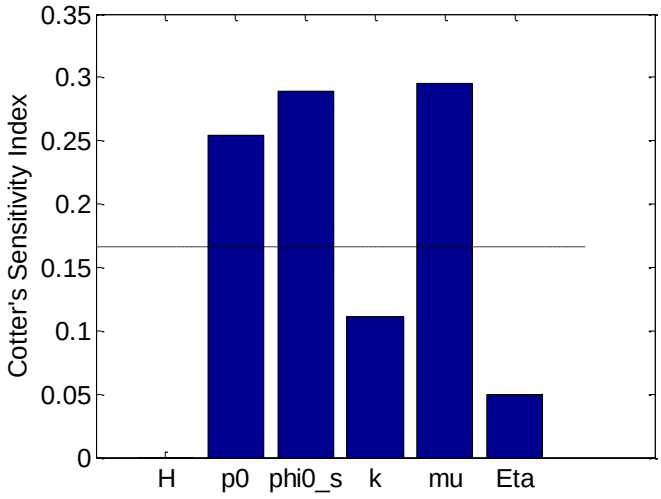

Figure 43. Cotter's sensitivity indices for the Gaussian oxygen cannula predictive model. The dashed line represent $1/n_p$ and any sensitivity index that falls above this line is considered a sensitive parameter. Initial hydrostatic tissue pressure (p_0), initial solid volume fraction (φ_0^s), and shear modulus (μ) were determined to be sensitive parameters.

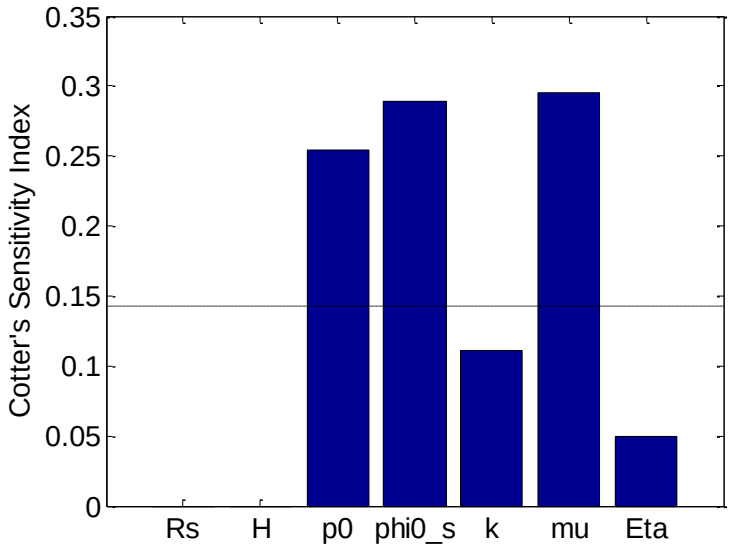

Figure 44. Cotter's sensitivity indices for the Hertz oxygen cannula predictive model. The dashed line represent $1/n_p$ and any sensitivity index that falls above this line is considered a sensitive parameter. Initial hydrostatic tissue pressure (p_0), initial solid volume fraction (φ_0^S), and shear modulus (μ) were determined to be sensitive parameters.

5.5 Discussions

5.5.1 Model Mechanics

Tissue deformation has been shown to play a significant role in the etiology of PrUs. Therefore, it is necessary to be able to predict tissue deformation accurately and efficiently. The geometric circular segment, Gaussian, and Hertz models developed herein provide an analytical means of estimating quasi-static tissue deformation with minimal input parameters.

Each model has unique features and predictive capabilities. The circular segment model is arguably the foundational model, predicting explicitly theoretical spherical deformation. The model is capable of predicting stress distribution across the contact area

radius. Most importantly, the geometric circular segment model is used to calibrate the Gaussian spread (σ) parameter required for the Gaussian model.

The Gaussian model proved to be the most accurate predictor of maximum stress in both the pre-term and term groups with 0% and 0.02% error, respectively. Unique to the Gauss model is its ability to compute stress distribution beyond the contact radius. This model feature is useful when predicting stress distributions on soft tissues in which the deformation does not return to zero at the contact radius edge, but rather at some distance beyond the contact. It is important to note that the Gaussian model, even when curve fit via the Gaussian spread parameter to the geometrical circular segment model, will always underestimate stress outside of the maximum value as the intrinsic shape of the Gaussian curve cuts into the theoretical circular segment (Figure 28 and Figure 33).

Of the three models, the Hertz model is the least accurate model, which is likely due to the singularity that arises in the Cauchy stress derivation. As the distribution nears the contact radius, the $F_{ZR}(F_{32})$ term in the deformation gradient nears a finite-time singularity, commonly referred to as "blow up". Singularities as such are relatively uncommon in mechanics models and are seen more frequently in mass transfer models [225]. Finite-time singularities cannot be avoided or removed. The effect of the singularity on the stress distribution output is best demonstrated in Figure 32 and Figure 37, in which the stress variation with tissue depth shows that tissue stress rapidly increases (towards the singularity) at the contact radius. This singularity is likely the result of the original assumption regarding the Hertz-type strain input which assumed that the strain profile at the tissue surface was the same form as the Hertz theory stress distribution. While the strain and stress distributions may look similar within the contact

area radius, it is at and beyond the contact radius that they differ. Stress beyond the contact area radius does go to zero; whereas, strain should not return to zero at the contact area radius. Furthermore, there are four assumptions that govern the use of Hertz contact theory:

1. Surfaces are continuous and non-conforming (initial contact is a point or a line)
2. Strains are small
3. Solids are elastic
4. Surfaces are frictionless

In the case of skin tissue, the surfaces are conforming with an initial contact surface area, strains are large, and surfaces are not frictionless. Moreover, these assumptions all require that the contact radius is much smaller than the radius ($a<<R$) which is not the case in skin deformation. Too many of the fundamental assumptions regarding Hertz contact theory have been violated in the skin tissue model. For these reasons, the proceeding chapters will not consider the Hertz-type strain input for any further models.

5.5.2 Local Ischemia and PrU Etiology

The predicted stress profiles of the quasi-static analysis also provide insights into the radius of capillary occlusion in the tissue. Capillary occlusion is widely accepted to occur at 32mmHg (4.3kPa) [226]. Using this assumption, the capillary occlusion threshold was surpassed in both pre-term and term neonates for a contact radius of R = 5.9mm and R =6.88mm, respectively, using the Gaussian strain profile. On average, both pre-term and term infants experienced occipital pressures that exceed capillary occlusion through a contact radius of approximately 12% of their skull radius. As such, according

to the pressure-time threshold curve of Reswick and Rogers [18], the occiput of neonates must be repositioned approximately every 5.5 hours at a minimum to prevent PrU development.

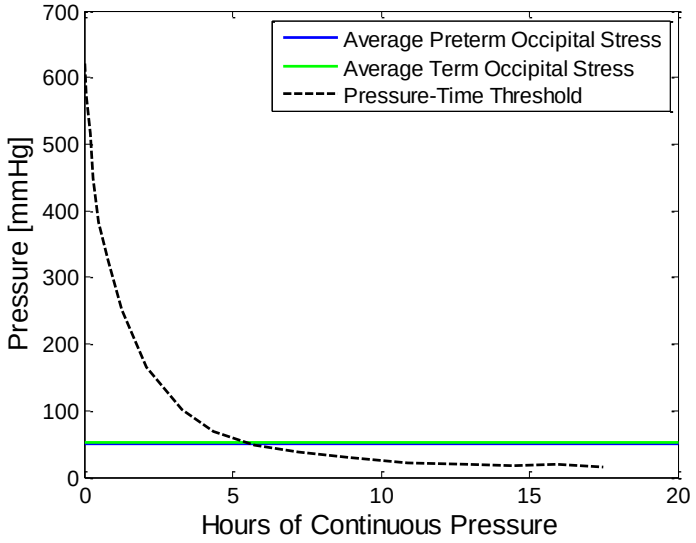

Figure 45. Average maximum occipital interface pressure of term and pre-term neonates as compared to the Reswick and Rogers [18] pressure-time threshold curve. This suggests the occiput of neonates should be repositioned at least every 5.5 hours for PrU prevention.

More generally, the quasi-static models were used to elucidate a trend in capillary occlusion versus tissue stress. For a direct comparison to the pressure-time threshold, the interface stress range was varied from 0-700mmHg (0-93kPa) (Figure 46). Blood volume fraction (φ^b) was computed using a Gaussian strain input. Assuming that complete capillary occlusion occurs at $\varphi^b = 0$, the corresponding interface pressure is 290mmHg (39kPa). The average maximum interface occipital stress experienced by neonates (52mmHg) is well below this threshold. However, at low interface pressures, the blood volume fraction is highly sensitive to changes in pressure between 0-150mmHg, a range in which the average maximum neonatal occipital interface stress falls. Although

neonates are not experiencing complete capillary occlusion (based on the assumption that complete capillary occlusion occurs at $\varphi^b = 0$, not a pressure threshold of 32mmHg), there is an extent of compromised blood flow with a decreased blood volume fraction. Compromised blood flow inhibits normal nutrient transport between the tissue constituents, and over time could lead to tissue breakdown. Partial capillary occlusion could contribute to the length of time that it takes a PrU to develop, as the tissue slowly degrades over time as nutrient needs are not met.

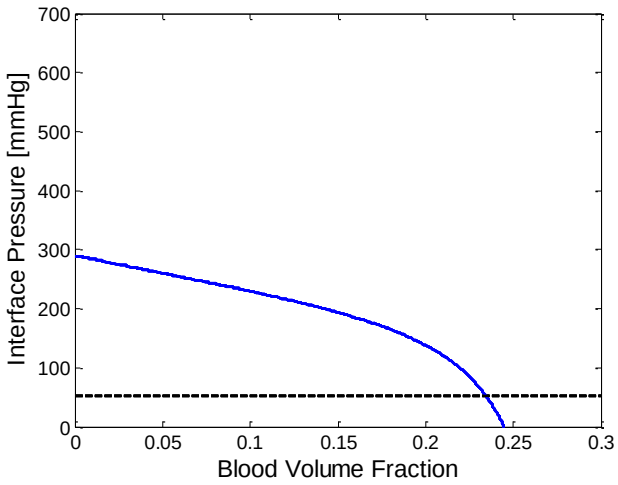

Figure 46. As a direct comparison to the classic pressure-time threshold, blood volume fraction was computed for interface pressure ranging from 0-700mmHg using a Gaussian strain input. Assuming that complete capillary occlusion occurs at $\varphi^b = 0$, the corresponding interface pressure is 290mmHg (39kPa). The reference line denotes the average maximum term neonate occipital interface pressure and is well below capillary occlusion. Since φ^b cannot be negative, tissue and model breakdown is assumed at pressures greater than 290mmHg.

5.5.3 Compromised Interstitial Fluid Flow and PrU Etiology

For the quasi-static model, zero constituent velocity was assumed, and therefore, there is no fluid movement in the tissue. While there is intrinsic interstitial fluid flow within the soft tissues, there is no deformation driven interstitial fluid flow. This is a

limitation of the quasi-static models, and consequently, the models will be developed with a time dependent assumption in the following chapter.

5.5.4 Mechanical Stress Distribution in the ECM and PrU Etiology

Since the Gaussian model provided the most accurate predictions of maximum stress, it was used to determine the maximum strain output. For the O-PrUs, the maximum strain for pre-term and term neonates was the same at 0.48 m/m. This means that despite pre-term infants being exposed to lower stress levels than their term counterparts (due to lower birth weights), they experience the same amount of tissue deformation. This is due to the compromised skinfold tissue thickness characteristic of pre-term neonates. Pre-term neonates often have compromised tissue thickness due to deficient adipose, underdeveloped dermal layers, or altogether missing layers, such as the stratum corneum [40]. The predisposition of pre-term infants to larger tissue deformation puts pre-term neonates at a higher risk for PrUs. This model provides the potential for a non-invasive bedside metric for predicting PrU occurrence. Given interface pressure and tissue thickness as inputs to the model, the maximum strain level can be computed and potentially correlated with PrU threshold strain.

Predictions of tissue level static strain may also be used to understand the cell mechanics at the microstructural level. Cells under static mechanical loading exhibit different migration, phenotype, and proliferation characteristics. When cells sense mechanical strains through cell surface receptors (integrins and ion channels), they adjust their expressions and adapt their environment to these changes. Generally, strains enhance the synthesis of ECM components [227]. Predicted strain levels may be used to understand the effect of the strain on the tissues at the cellular level.

5.5.5 Sensitivities and Model Limitations

The sensitivity analysis between the O-PrU models and OC-PrU models were slightly different. Across all models, the initial hydrostatic tissue pressure (p_0) and initial solid volume fraction (φ_0^s) were found to be sensitive parameters. However, for the OC-PrU models, the shear modulus (μ) was also a very sensitive parameter. All three of these parameters are either highly debated or largely unknown for skin tissue. Initial hydrostatic tissue pressure measurements vary widely, with some investigators not even agreeing on the sign of the term [228]. Other investigators have attempted to determine the best function for hydrostatic tissue pressure, with assumptions ranging from zero to a constant to complex deformation dependent functions [59,63,182]. The initial solid volume fraction for neonatal skin is simply not well documented in literature, although it is known that solid volume fraction continues to increase from birth to the age of 1 when in plateaus to that of an adult [206]. Adult solid volume fractions are typically below 0.3 [229]. Shear modulus ranges within the adult population are likewise lacking in literature and non-existent within the neonatal population.

As such, limitations of the model begin with the sensitivity of already difficult to define parameters. The inaccuracies associated with these parameters leads to inaccuracies in the predictive capability of the models. The model is also limited by its restriction to the epidermis, dermis, and hypodermis in tissue thickness measurement. A refinement of the model might expand the tissue thickness to include muscle, especially given that muscle tissue deformation is highly linked to the occurrence of DTI [3,212] .

CHAPTER 6. TIME DEPENDENCE AND FLUID FLOW MODELING

6.1 Introduction

Time-varying loading of biological tissues has been demonstrated to maintain or increase local fluid flow characteristics and thereby promote healthy nutrient transport in loaded tissues [230,231]. This phenomenon has been thoroughly investigated in the context of bone, for which a low magnitude, whole body vibration has been shown to have osteogenic affects in bone [232,233] via increased fluid transport through the bone tissue [194]. Several animal [234,235] and human [236,237] experimental models have successfully shown whole body vibration as an effect means to slow bone density loss and promote bone formation.

Likewise, in soft biological tissues, time-varying loading has also been investigated, although not as thoroughly as in bone, as a means of accelerating wound healing at the micro- and macroscale levels. Weinheimer-Haus demonstrated in an *in vivo* study of mice that applying a 45Hz low intensity vibration for 30 minutes a day increases angiogenesis and granulation tissue formation, accelerates wound-closure and re-epithelialization, reduces neutrophil accumulation, and increases macrophage accumulation [238]. Leduc *et. al* applied multidirectional vibration to newly formed scars and showed accelerated regeneration of severed veins and lymph vessels [239]. Peer *et. al* demonstrated in an *in* vivo study of athletes with ankle sprain or hamstring strain

injuries that a 20Hz muscle stimulation applied for 10 minutes improved flexibility and reduced perceived stiffness [240].

More recently, time-varying loading is being investigated as a means of increasing local skin blood flow as a means of prophylactic PrU prevention and PrU treatment. The mechanism by which time-varying loading prevents and treats PrUs is two-fold: 1.) The onset and severity of PrUs is prevented by cyclically relieving local pressure maximums, such that the deformed tissue is not continuously subjected to a pressure greater than that of capillary occlusion (32mmHg / 4.3kPa) and 2.) Skin blood and interstitial fluid flow maintains normal physiologic values during tissue deformation due to the intrinsic ability of vibration to increase fluid flow. Nakagami [231] demonstrated in an *in vivo* model of hairless mice that a frequency of 47Hz produced significant increases in skin blood flow. Arashi *et. al* showed with an *in vivo* study of hospital patients that a frequency of 47Hz applied for 15 minutes 3 times a day for up to 7 days facilitated the healing of Stage I PrUs and Stage III and Stage IV PrUs with necrotic tissues [241]. In an in vivo rat model, Sari showed that vibration therapy significantly inhibited deterioration of DTI [242]. Although more investigative is necessary, early studies have shown the potential of vibration to be a novel, non-invasive, low-cost, effective adjunctive therapy in PrU protocols [243].

In this chapter, the two dimensional, compressible model of skin tissue developed in Chapter 5 is provided with time-varying homogeneous and non-homogeneous strain input. The time varying input simulates the effects of a vibrating support surface on skin tissue fluid flow towards the understanding of the use of such devices as prophylactic and adjunctive treatment modalities for PrUs.

6.2 Theory

In order to describe the mechano-physiological processes of load-bearing human cutaneous and subcutaneous tissue, a mixture theory based model is developed and interfaced with uniform and modified Hertzian contact mechanics input. Human skin tissue is a complex system, composed of several distinct layers (epidermis, dermis, and hypodermis) and structures (follicles, vasculature, sebaceous glands, etc.). Each layer contains many different components including collagen and elastin in a gel continuum of mucopolysaccharides with a principle mass of collagen [40]. Previous models of load-bearing skin tissue typically consider biphasic continua with a single solid and single fluid component, such that all fluids are lumped into the fluid constituent [59]. For the purposes of this study, along with the solid extracellular matrix (ECM) constituent, two fluids will be considered, interstitial fluid (IF) and blood. Therefore, the three constituents of the triphasic mixture are extracellular matrix (s), interstitial fluid (f), and blood (b). The tissue is assumed to be compressible, homogeneous, and isotropic and is subjected to time varying loading.

Each constituent is regarded as a continuum having its own properties, kinematics, and balance laws. As such, each constituent has its own mass, volume, apparent, and true density, M^{α}, V^{α}, ρ^{α} and ρ_T^{α}, where $\alpha = s, f, b$. Apparent density and true density are related by the volume fraction, φ^{α} such that $\rho^{\alpha} = \varphi^{\alpha}\rho_T^{\alpha}$. The volume fraction of each constituent is given by $\varphi^{\alpha} = V^{\alpha}/V$ such that at any given time $\sum_{\alpha} \varphi^{\alpha} = 1$.

6.2.1 Solid Particle Kinematics

The solid particle position, x_i^s, can be described in terms of the reference configuration, X_i^s, such that

$$\begin{cases} {x_1}^s = {X_1}^s - \eta\varepsilon_3 {X_1}^s \\ {x_2}^s = {X_2}^s - \eta\varepsilon_3 {X_2}^s \\ {x_3}^s = {X_3}^s + \varepsilon_3 {X_3}^s \end{cases} \quad (6.1\text{-}6.3)$$

where $\boldsymbol{\eta}$ is the expansion ratio and ε_3 is the strain profile. Applying a coordinate transformation for the axisymmetric assumption results in a solid particle position described by

$$\begin{cases} r^s = R^s - \eta\varepsilon_Z R^s \\ \theta^s = \Theta^s \\ z^s = Z^s + \varepsilon_Z Z^s \end{cases} . \quad (6.4\text{-}6.6)$$

The rate of deformation tensor in cylindrical coordinates is then given by

$$\underline{F}^s = \underline{I} + \nabla u = \begin{bmatrix} 1 + \frac{\partial u_R}{\partial R} & 0 & \frac{\partial u_R}{\partial Z} \\ 0 & 1 + \frac{U_R}{R} & 0 \\ \frac{\partial u_Z}{\partial R} & 0 & 1 + \frac{\partial u_Z}{\partial Z} \end{bmatrix} \quad (6.7)$$

resulting in the following equation for Cauchy stress in the loading direction

$$T_{ZZ}^T = -p + \varphi^s \kappa J^s (J^s - 1) + \frac{\varphi^s \mu}{J^s}\left\{\left[(1 + \frac{\partial u_Z}{\partial Z})^2 + (\frac{\partial u_Z}{\partial R})^2\right] - \frac{1}{3}\left[(1 + \frac{\partial u_R}{\partial R})^2 + (1 + \frac{U_R}{R})^2 + (\frac{\partial u_Z}{\partial R})^2 + (1 + \frac{\partial u_Z}{\partial Z})^2\right]\right\}. \quad (6.8)$$

The final form of the equation depends on the selected format for the strain profile.

6.2.1.1 Axisymmetric Spherical Loading

For a case study of neonatal occipital PrUs, the occiput was modeled as an axisymmetric, rigid spherical indenter lying on an elastic half-space of tissue. The contact

area radius was presumed to be small enough that the radius of curvature of the skin on the skull is negligible. The strain profile at the loading surface was described using three different strain profiles, including uniform, geometrical circular segment, and Gaussian profiles.

6.2.1.1.1 Uniform Strain Profile

The strain profile induced by the occiput on the surface of the skin was modeled as a uniform, time dependent strain, such that

$$\varepsilon_Z = -\gamma + \gamma A(\cos(\omega t) - 1). \tag{6.9}$$

6.2.1.1.2 Geometrical Circular Segment Strain Profile

The strain profile induced by the occiput on the surface of the skin was modeled using the axisymmetric geometric equations for the arc of circular segment.

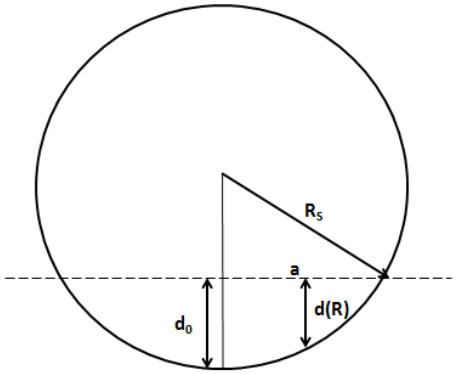

Figure 47. The geometric relationships between sphere radius (R_s), contact radius (a), and maximum indentation (d_o) are used to develop the geometric circular segment strain profile function.

The derived strain profile is a function of tissue thickness (H), radius of the sphere (R_S), position in R, and maximum deformation (d_0) such that

$$\varepsilon_z = -\frac{d(R)}{H} + \frac{d(R)}{H} A(\cos(\omega t) - 1) \tag{6.10}$$

$$d(R) = \sqrt{R_S^2 - R^2} - \sqrt{R_S^2 - a^2} \tag{6.11}$$

$$a^2 = R_S^2 - (R_s - d_0)^2 \tag{6.12}$$

$$d_0 = d(R = 0). \tag{6.13}$$

6.2.1.1.3 Gaussian Strain Profile

The strain profile on the surface of the skin was also modeled using a Gaussian distribution, such that

$$\varepsilon_Z = -\gamma e^{\left(\frac{-R^2}{2\sigma^2}\right)} + \gamma e^{\left(\frac{-R^2}{2\sigma^2}\right)} A(\cos(\omega t) - 1) \tag{6.14}$$

$$\gamma = -\varepsilon_Z(R = 0). \tag{6.15}$$

The spread of the Gaussian distribution (σ) was determined by a curve fit with the preceeding circular segment strain profile.

6.2.1.2 Plane Strain Cylindrical Loading

For a case study of neonatal oxygen cannula PrUs, the oxygen cannula was modeled as rigid cylinder lying on an elastic half-space of tissue in plane strain. The deformation of the cannula itself was assumed negligible. The strain profile at the loading surface was described using a Gaussian strain profile.

The solid particle position, x_i^s, can be described in terms of the reference configuration, X_i^s, such that

$$\begin{cases} {x_1}^s = {X_1}^s \\ {x_2}^s = {X_2}^s - \eta\varepsilon_3 {X_2}^s \\ {x_3}^s = {X_3}^s + \varepsilon_3 {X_3}^s \end{cases} \quad (6.16\text{-}6.18)$$

where $\boldsymbol{\eta}$ is the expansion ratio and ε_3 is the strain profile. The rate of deformation tensor is then given by

$$\underline{F^s} = \frac{x_i^s}{X_A^s} = \begin{bmatrix} 1 & 0 & 0 \\ 0 & \frac{x_2^s}{X_2^s} & 0 \\ 0 & \frac{x_3^s}{X_2^s} & \frac{x_3^s}{X_3^s} \end{bmatrix} \quad (6.19)$$

resulting in the following equation for Cauchy stress in the loading direction

$$T_{33}^T = -p + \varphi^s \kappa J^s (J^s - 1) + \frac{\varphi^s \mu}{J^s}\left\{\left[(\frac{x_3^s}{X_2^s})^2 + (\frac{x_3^s}{X_3^s})^2\right] - \frac{1}{3}\left[1 + (\frac{x_2^s}{X_2^s})^2 + (\frac{x_3^s}{X_2^s})^2 + (\frac{x_3^s}{X_3^s})^2\right]\right\} \quad (6.20)$$

The final form of the equation depends on the selected format for the strain profile. The strain profile induced by an oxygen cannula on the surface of the skin was modeled using a Gaussian distribution, such that

$$\varepsilon_3 = -\gamma e^{(\frac{-X_2^2}{2\sigma^2})} + \gamma e^{\left(\frac{-X_2^2}{2\sigma^2}\right)} A(\cos(\omega t) - 1) \quad (6.21)$$

$$\gamma = -\varepsilon_3(X_2 = 0). \quad (6.22)$$

The spread of the Gaussian distribution (σ) was determined by a curve fit with the preceeding circular segment strain profile.

6.2.2 Balance of Mass

The governing equations employed in mixture theory are the balance of mass and the conservation of linear momentum for the α-constituent. The balance of mass for the α- constituent is

$$\frac{D^{\alpha}\rho^{\alpha}}{Dt} + \rho^{\alpha}\nabla \cdot \underline{v}^{\alpha} = \hat{q}^{\alpha} \tag{6.23}$$

where $\frac{D^{\alpha}h}{Dt} = \frac{\partial h}{\partial t} + \frac{\partial h}{\partial x_i} v_i^{\alpha}$ is the material derivative, $\boldsymbol{v}^{\alpha}$ is the velocity of the α-constituent and $\hat{q}^{\alpha} = \rho_T^{\alpha}\hat{r}^{\alpha}$ is the rate of mass production per unit volume. Expanding the equation and applying the mass production constrain $\sum_{\alpha}\hat{r}^{\alpha} = 0$ and neglecting mass exchanges between the constituents yields the balance of mass of the mixture

$$\frac{\partial \varphi^{s}}{\partial t} + \nabla \cdot \left(\varphi^{s}\underline{v}^{\boldsymbol{s}}\right) + \frac{\partial \varphi^{f}}{\partial t} + \nabla \cdot \left(\varphi^{f}\underline{v}^{\boldsymbol{f}}\right) + \frac{\partial \varphi^{b}}{\partial t} + \nabla \cdot \left(\varphi^{b}\underline{v}^{\boldsymbol{b}}\right) = 0. \tag{6.24}$$

6.2.3 Conservation of Linear Momentum

The conservation of linear momentum for the α-constituent is

$$\rho^{\alpha}\frac{D^{\alpha}\boldsymbol{v}^{\alpha}}{Dt} = \nabla \cdot \underline{T}^{\alpha} + \rho^{\alpha}\underline{b}^{\alpha} + \underline{\pi}^{\alpha} \tag{6.25}$$

where $\underline{T}^{\alpha}$is the Cauchy stress tensor, $\underline{b}^{\alpha}$s body force, and $\underline{\pi}^{\alpha}$is the inter-constituent interaction term. The α-constituent Cauchy stresses are defined as such

$$\begin{cases} \underline{T}^{s} = -\varphi^{s}p\underline{I} + \varphi^{S}\hat{\underline{T}}^{s} \\ \underline{T}^{f} = -\varphi^{f}p\underline{I} \\ \underline{T}^{b} = -\varphi^{b}p\underline{I} \end{cases} \tag{6.26-6.28}$$

where p is the hydrostatic tissue pressure, and $\hat{\underline{T}}^{s}$ is the compressible neo-hookean solid constitutive equation

$$\hat{\underline{T}}^{s} = \kappa J^{s}(J^{s} - 1)\underline{I} + \frac{\mu}{J^{s^{2}/3}} dev(\underline{B}^{s}). \tag{6.29}$$

Viscous contributions of the fluid are assumed to be accounted for in the solid-fluid interaction term [179]. The resulting total Cauchy stress of the mixture when the constraint on the volume fraction, $\sum_\alpha \varphi^\alpha = 1$, is applied is

$$\underline{T}^T = \underline{T}^s + \underline{T}^f + \underline{T}^b = -p\underline{I} + \underline{\hat{T}}^s. \tag{6.30}$$

The inter-constituent interaction terms model the drag between two constituents, and as such, $\underline{\pi}^\alpha$ must satisfy the condition that $\sum_\alpha \underline{\pi}^\alpha = 0$ [179]. The interaction terms of the mixture are therefore defined as

$$\begin{cases} \underline{\pi}^s = \frac{\mu^f}{K_{sf}}(\underline{v}^f - \underline{v}^s) \\ \underline{\pi}^f = -\frac{\mu^f}{K_{sf}}(\underline{v}^f - \underline{v}^s) + \underline{\xi} \\ \underline{\pi}^b = -\underline{\xi} \end{cases} \tag{6.31-6.33}$$

where ξ accounts for the unknown interaction between the interstitial fluid and the blood. The unknown interactions may originate from viscous interactions (drag) between the interstitial fluid and the blood, a Starling-type pressure gradient, or interconstituent nutrient transport resulting in a solute-type interaction. No interaction term is included for the blood and the solid, as interstitial fluid bounds the two constituents. Assuming that the body forces are negligible, the balance of linear momentum for the α-constituents becomes

$$\begin{cases} \rho^s \frac{D^s \boldsymbol{v}^s}{Dt} = \nabla \cdot \underline{T}^s + \frac{\mu^f}{K_{sf}}(\underline{v}^f - \underline{v}^s) \\ \rho^f \frac{D^f \boldsymbol{v}^f}{Dt} = \nabla \cdot \underline{T}^f - \frac{\mu^f}{K_{sf}}(\underline{v}^f - \underline{v}^s) + \underline{\xi} \\ \rho^b \frac{D^b \boldsymbol{v}^b}{Dt} = \nabla \cdot \underline{T}^b - \underline{\xi} \end{cases} \tag{6.34-6.36}$$

The final form of the solid constituent conservation of linear momentum equation depends on the form of the input strain as derived in the preceeding sections.

6.2.4 Assumptions and Boundary Conditions

In order to solve the system of equations model specific assumptions and boundary conditions must be applied. The primary assumptions are 1.) no change in $\mathbf{E_Z}$ ($\mathbf{E_3}$) deformation such that $v_z^s = v_z^f = v_z^b$ ($v_3^s = v_3^f = v_3^b$) and 2.) $\varphi_0^f = 2.5\varphi_0^b$ [244,245]. The primary boundary conditions are 1.) axisymmetry at R = 0 ($X_2 = 0$), 2.) prescribed strain profile at the loading surface, 3.) $v_z^f = v_z^b = 0$ ($v_3^f = v_3^b = 0$) at the impervious epidermal surface, and 4.) the radial Cauchy stress at R = R_0 is equal to initial hydrostatic tissue pressure.

6.3 Methods

6.3.1 Prediction of Fluid Velocity

Interstitial fluid velocity was predicted for each strain profile. The models were provided with average literature values previously presented for skin thickness (*H*), initial solid volume fraction (φ_0^s), occiput/oxygen cannula radius (R_s), and calibrated bulk modulus (κ), shear modulus (μ), and expansion ratio ($\boldsymbol{\eta}$). The true density of the ECM and the hydraulic conductivity, two new parameters introduced by the time dependent model, are taken to be literature averages at $1375\frac{kg}{m^3}$ and $9x10^{-13}\frac{m^2}{Pa \cdot s}$, respectively [246-248]. The maximum strain values predicted from the quasi-static pressure distribution models were used as input into the time dependent model. The magnitude of the vibration (*A*) was varied from 100-700με to adequately span the range of tissue microdeformation shown to promote cell proliferation and wound healing (400-600με)

[249]. Similarly, the frequency of the input was varied from 10-80Hz to adequately span the low frequency range.

Given the prediction precision of the uniform strain model in predicting maximum quasi-static stress (<0.1% error) as well as the ability of the model to verify with non-homogeneous interstitial fluid velocity predictions (<9% error), the blood velocity was predicted using a uniform strain profile.

All model outputs reported were calculate at tissue radius $R = \frac{R_s}{2}$ and a tissue depth of $Z = \frac{H}{2}$.

6.3.2 Sensitivity Analysis

A Cotter's sensitivity analysis was used to determine the relative sensitivity of the model output (maximum interstitial fluid velocity) to n_p respective inputs. The methodology followed that of section 3.6. The parameters of interest for each individual sensitivity analysis depend on the form of the strain input. The ranges for each parameter are determined from data within literature and calibration results, both of which are previously reported.

Table 14. A Cotter's sensitivity analysis was used to determine the relative sensitivity of the model output (maximum interstitial fluid velocity) to input parameters. The parameters of interested depend on the selection of strain input. The parameter ranges were determined from literature values and calibration results previously reported.

	Occipital PrU		Oxygen Cannula PrU	
Parameter	Pre-Term Neonates	Term Neonates	Pre-Term Neonates	Term Neonates
OCF [cm]	18.3-35.6	30.3-37.9	18.3-35.6	30.3-37.9
H [mm]	3.99-4.81	2.41-6.12	3.99-4.81	2.41-6.12
Interface Pressure [kPa]	2-11.6	1.73-12.13	.114-.140	.129-.157
Initial Solid Volume Fraction	0.096-0.166	0.096-0.17	0.096-0.17	0.096-0.17
Expansion Ratio	0.45-0.55	0.45-0.55	0.45-0.55	0.45-0.55
Shear Modulus [kPa]	0.66-3.3	0.66-3.3	0.66-3.3	0.66-3.3
Bulk Modulus [kPa]	227.7-230	227.7-230	227.7-230	227.7-230
Hydraulic Conductivity [m^2/Pas]	0.18-1800x10^-15	0.18-1800x10^-15	0.18-1800x10^-15	0.18-1800x10^-15
True Density of the Solid [kg/m^3]	1338-1420	1338-1420	1338-1420	1338-1420

6.4 Results

6.4.1 Prediction of Fluid Velocities Under Occipital Loading

Both the geometric circular segment and Gaussian strain profiles were used to predict interstitial fluid velocity. Reported values for interstitial fluid velocity range from $0.6\frac{\mu m}{s}$ to $9.7\frac{\mu m}{s}$ [250-253]. At low amplitude and frequency input, closest to quasi-static, the interstitial fluid velocity is on the same order of magnitude as is reported in literature (A = 100με, f = 10, $v_r^f = 8\frac{\mu m}{s}$). As the magnitude and frequency increase, the predicted interstitial fluid velocity surpasses literature values.

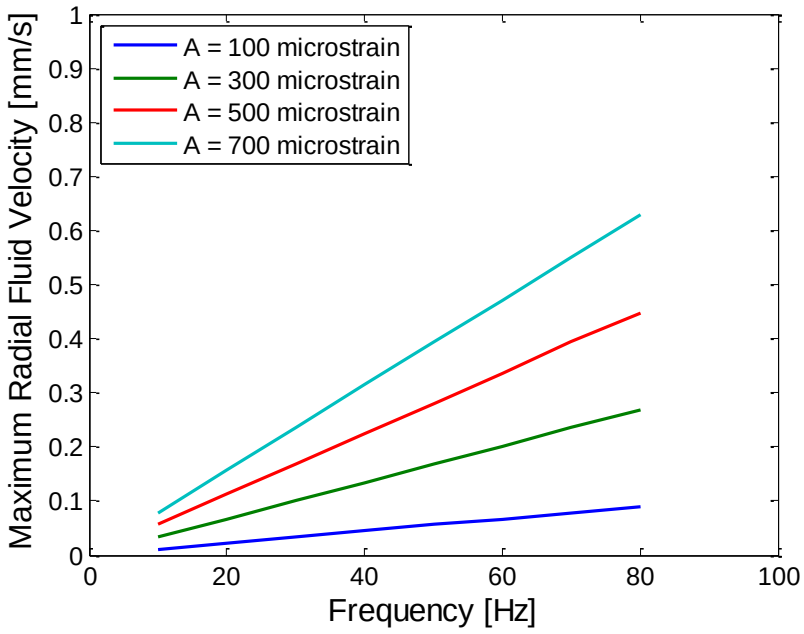

Figure 48. Predicted radial fluid velocity for term neonates using a uniform strain with varying input amplitude and frequency. At A = 100με and f = 10Hz, the maximum fluid velocity is $11\,\frac{\mu m}{s}$.

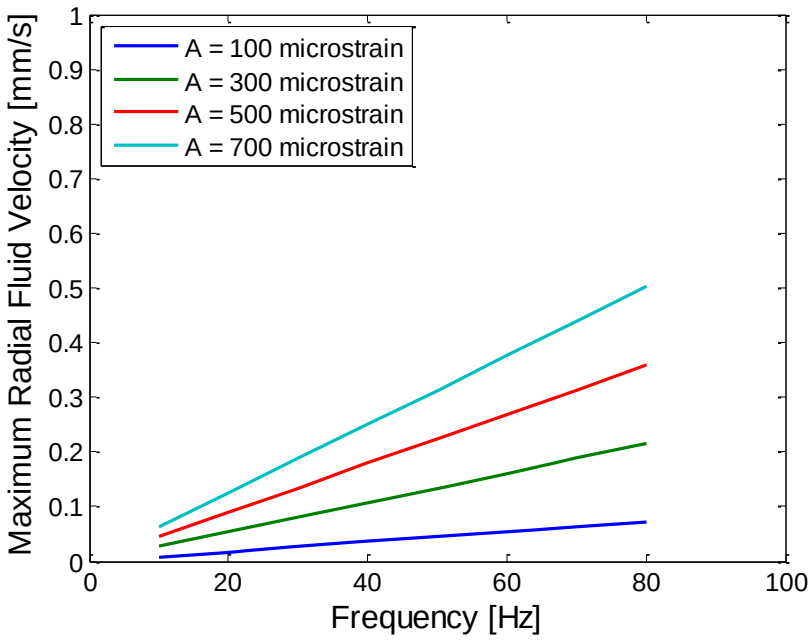

Figure 49. Predicted radial fluid velocity for term neonates using a geometric circular segment strain with varying input amplitude and frequency. At A = 100με and f = 10Hz, the maximum fluid velocity is5.5 $\frac{\mu m}{s}$.

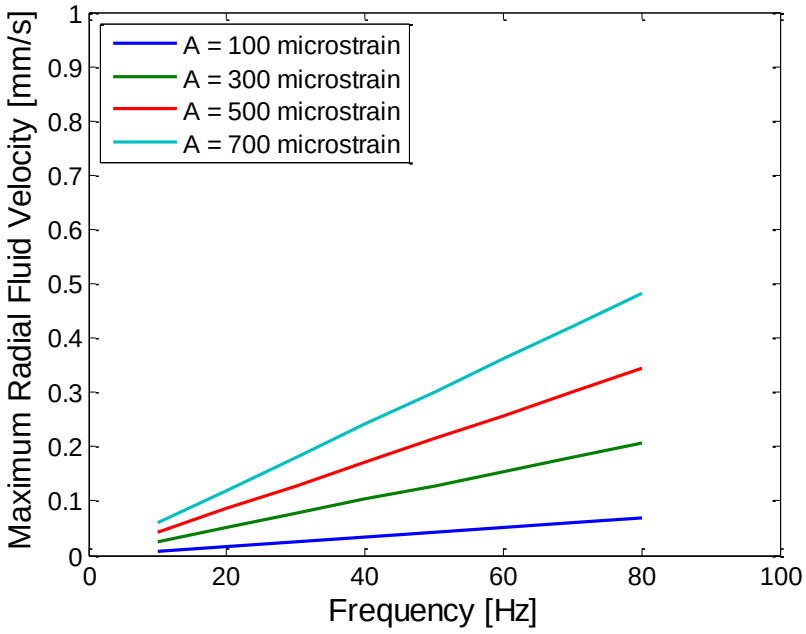

Figure 50. Predicted radial fluid velocity for term neonates using a Gaussian strain with varying input amplitude and frequency. At A = 100με and f = 10Hz, the maximum fluid velocity is $8\frac{\mu m}{s}$.

The geometric circular segment model was used to predict the velocity profiles within the contact area radius. For these models, amplitude A was held constant at 300με. Model output shows that inputs of increasing skull radius are more sensitive to changes in frequency.

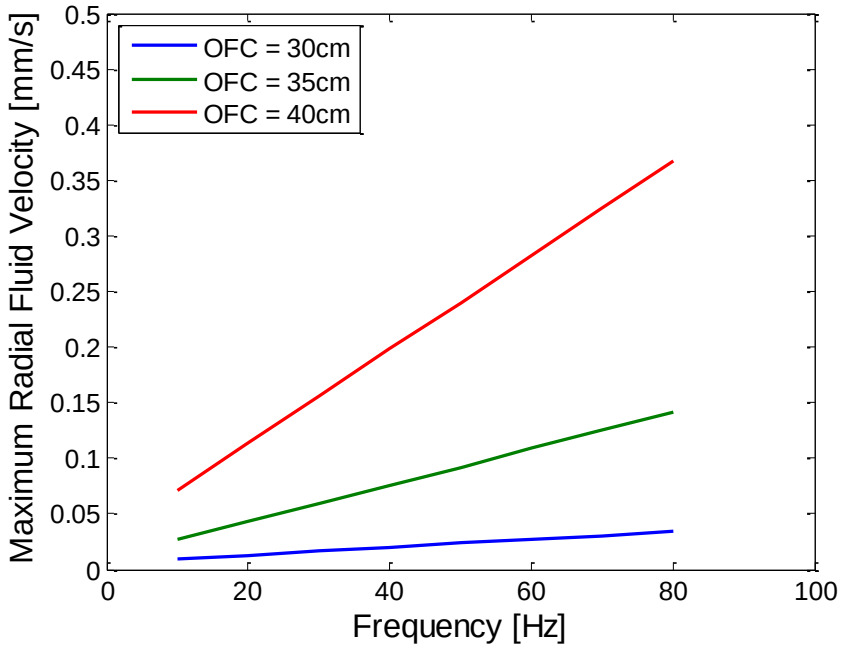

Figure 51. The geometric circular segment model was used to predict the maximum interstitial fluid velocity in term neonates with varying sphere radius input. Vibration amplitude was held constant at A = 300με. Inputs of increasing sphere radius are more sensitive to changes in frequency.

The uniform strain input model was employed to predict radial blood velocity. Reported values for neonatal capillary blood velocity are not very different from adults and range from 0.04 to $1.2\frac{mm}{s}$ [254,255]. At low amplitude and frequency input, closest to quasi-static, the interstitial fluid velocity is on the same order of magnitude as is reported in literature (A = 100με, f = 10, $v_r^f = 0.06\frac{mm}{s}$). The predicted blood velocity remains on the same order of magnitude as the reported literature values for all ranges of input amplitude (*A*) and frequency (*f*).

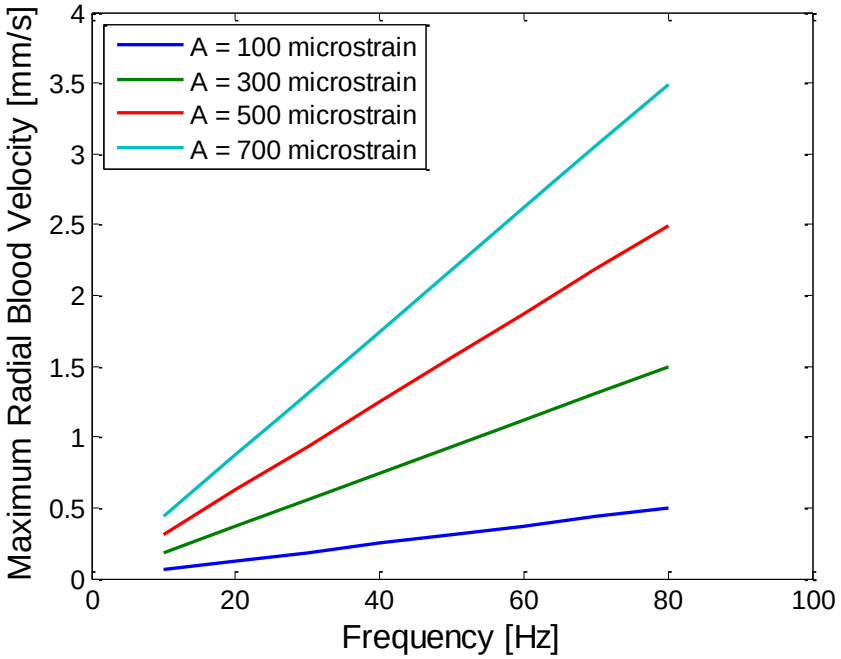

Figure 52. Predicted radial blood velocity for term neonates using a uniform strain with varying input amplitude and frequency. At A = 100με and f = 10Hz, the maximum fluid velocity is $0.06\frac{mm}{s}$.

6.4.2 Prediction of Fluid Velocities Under Oxygen Cannula Loading

The Gaussian model has the unique ability to predict fluid velocity well beyond the input radius. For these models, amplitude A was held constant at 300με. Model output shows that interstitial fluid velocity is drastically higher beyond the edge of the input radius.

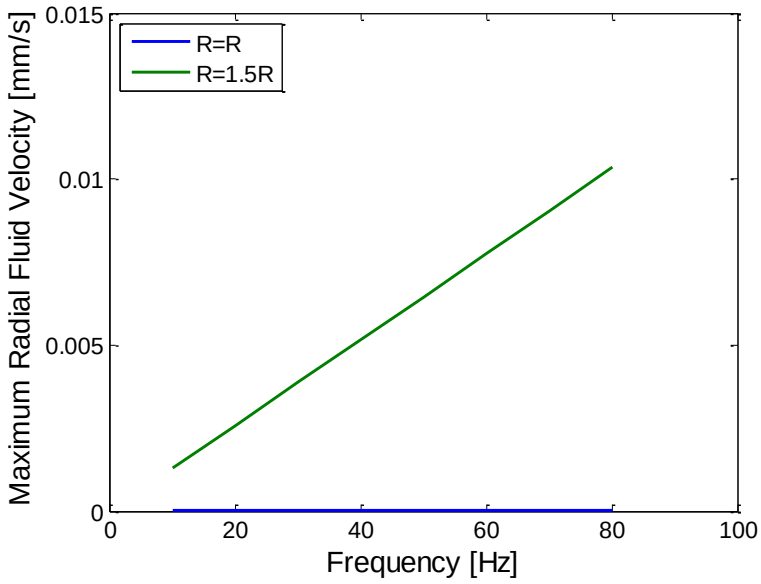

Figure 53. The Gaussian model was used to predict the maximum interstitial fluid velocity in term neonates well beyond the input radius. Vibration amplitude was held constant at A = 300με. The interstitial fluid velocity at half radius beyond the radius of the input is drastically higher and more sensitive to changes in frequency.

6.4.3 Sensitivity Analysis

The sensitivity analysis determined that tissue thickness (H), expansion ratio (η), and sphere radius (R_s) were sensitive parameters for the geometric circular segment model. Whereas, the expansion ratio (η) was the only sensitive parameter for the Gaussian model.

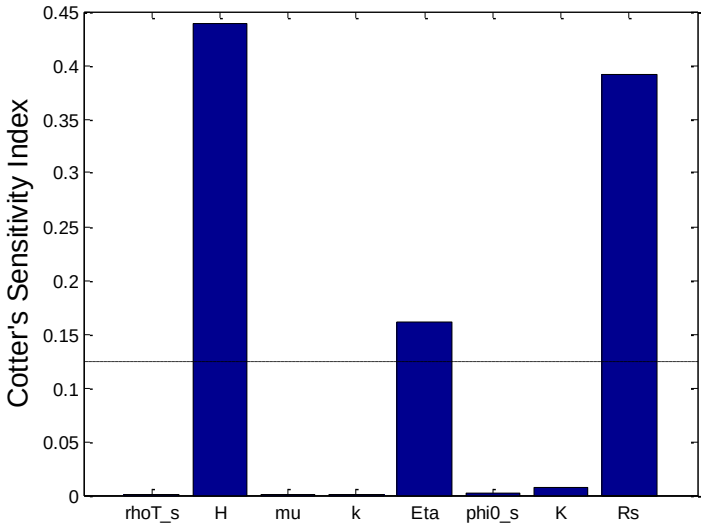

Figure 54. Cotter's sensitivity indices for the geometric circular segment occipital predictive model. The dashed line represent $1/n_p$ and any sensitivity index that falls above this line is considered a sensitive parameter. Amplitude and frequency were held constant at A = 300με and f = 40Hz. Tissue thickness (H), expansion ratio (η), and sphere radius (R_s) were found to be sensitive parameters.

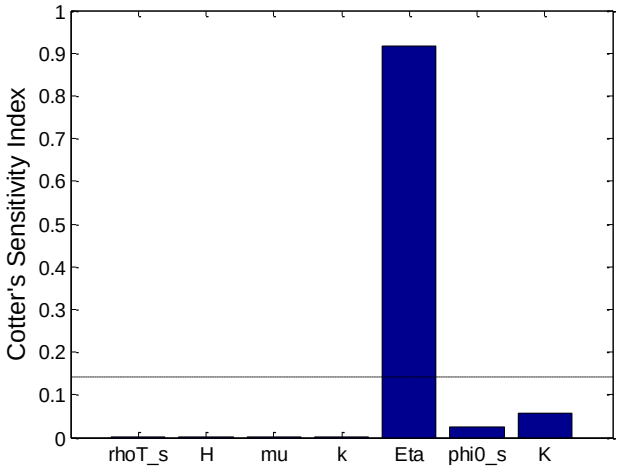

Figure 55. Cotter's sensitivity indices for the Gaussian occipital predictive model. The dashed line represent $1/n_p$ and any sensitivity index that falls above this line is considered a sensitive parameter. Amplitude and frequency were held constant at A = 300με and f = 40Hz. Expansion ratio (η) is the only sensitive parameter.

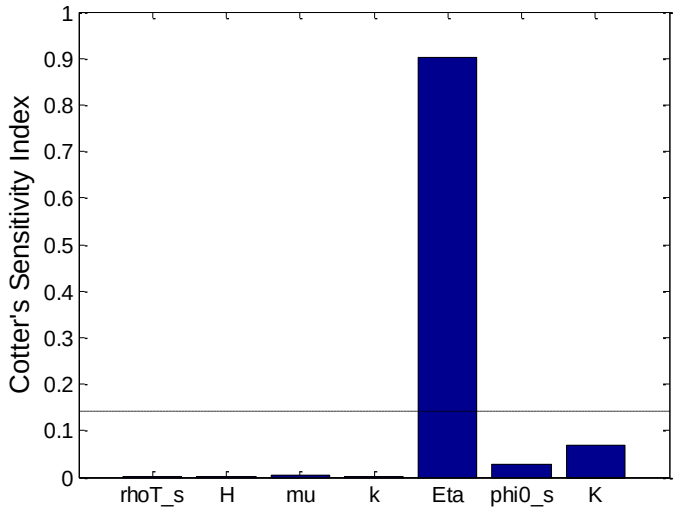

Figure 56. Cotter's sensitivity indices for the Gaussian oxygen cannula predictive model. The dashed line represent $1/n_p$ and any sensitivity index that falls above this line is considered a sensitive parameter. Amplitude and frequency were held constant at A = 300με and f = 40Hz. Expansion ratio (η) is the only sensitive parameter.

6.5 Discussions

6.5.1 Model Mechanics

The uniform, geometric circular segment, and Gaussian models were used to predict fluid velocities under time-varying loading conditions. The uniform model provides a good benchmark for model verification and the geometric circular segment and Gaussian models each provide unique output capabilities towards the understanding of fluid velocity variation.

The geometric circular segment model has the ability to predict the velocity profile throughout the contact area radius. Inputs of increasing radius (where radius is either the skull radius or the oxygen cannula radius) were shown to be more sensitive to changes in frequency (Figure 51). Thus, infants with a larger OFC would require lower frequency time-varying loading to induce the same amount of velocity increase as an infant with a

smaller OFC. In clinical applications, this becomes an important analytical tool when dealing with infants with much larger skull radii as in dolicocephaly, brachycephaly, and hyperbrachycephaly as discussed in Chapter 3.

Since the Gaussian model uses a statistical spread as opposed to a geometric representation, its output is not limited to within the bounds of the contact area radius. Therefore, the Gaussian model has the unique capability of modeling fluid well beyond the contact area radius. This is especially useful in modeling soft tissue deformations in which the strain does not return to zero at the edge of the contact area radius, but rather at some distance beyond the edge. Interstitial fluid velocities at 1.5R were shown to be significantly greater than those at the contact radius edge (Figure 53).

6.5.2 Local Ischemia and PrU Etiology

The time dependent models demonstrated significant increases radial blood velocity during time-varying loading. The affect of apparent strain magnitude and frequency on radial fluid flow velocity was determined. At low values of apparent strain and frequency, the predicted radial blood velocity was on the same order of magnitude as *in vivo* unloaded tissue fluid velocity measurements in literature.

Ischemia, a direct results of excessive pressure loading, has often been hypothesized as a mechanism of PrU etiology [188,210,256,257]. Time-varying loading has a demonstrated ability to increase local radial blood velocities in a controlled manner via selection of apparent strain amplitude and frequency of input. Therefore vibratory support surfaces have the theoretical ability to act as both a prophylactic prevention of PrUs and an adjunctive therapy for the treatment of PrUs by maintaining normal blood

flow characteristics during loading given an appropriate selection of apparent strain amplitude and input frequency. The theory of time-varying loading as an accelerator of PrU healing has already been document in two *in vivo* experiments of hospital patients [231,241]. Further investigation into the optimized amplitude and frequency is necessary.

6.5.3 Compromised Interstitial Fluid Flow and PrU Etiology

The time dependent models also demonstrated significant increases radial interstitial fluid velocity during time-varying loading. The affect of apparent strain magnitude and frequency on radial interstitial fluid velocity was determined. At low values of apparent strain and frequency, the predicted interstitial fluid velocity was on the same order of magnitude as *in vivo* unloaded tissue interstitial fluid velocity measurements in literature.

Compromised interstitial fluid flow, another direct result of excessive pressure loading has also been hypothesized as a mechanism of PrU etiology [63,258,259]. A compromise in interstitial fluid flow causes a decrease in nutrient transport between constituents as well as a slowed lymphatic system. Time-varying loading has a demonstrated ability to increase local interstitial fluid velocities in a controlled manner via selection of apparent strain amplitude and frequency of input. As with increasing radial blood velocity, this reinforces the theory that controlled time-varying input has great potential as a prophylactic prevention and treatment for PrUs.

6.5.4 Mechanical Stress Distribution and PrU Etiology

As with static loading of tissues, time-varying loading causes changes at the microcellular level. Cell morphology, phenotype, proliferation, differentiation, and syntehsis are affected under time-varying loading [260-262]. Time-varying strains have a even greater effect on collagen and elastin synthesis than static loading [227]. A secondary benefit to applying a time-varying load to pressure loaded tissue is the potential to promote normal cell behavior via controlled microstructural strain. The predicted quasi-static strain levels and apparent strain magnitude of the time-varying loading may be used to determine the effect of time-varying loading on the tissues at the cellular level.

6.5.5 Sensitivities and Model Limitations

The geometric circular segment model for occipital PrUs resulted in three sensitive parameters, tissue thickness (H), expansion ratio (η), and sphere radius (R_s). Likewise, the Gaussian model of oxygen cannula PrUs resulted in a single sensitive parameter, the expansion ratio (η). The limitations regarding these parameters were discussed in Chapter 5 and still hold for the time dependent model.

Limitations in the time dependent triphasic mixture theory can be addressed in further iterations of the model. In order to solve the set of equations analytically, several assumptions were made as discussed previously. Discretization of the model would eliminate the need for one or more of the assumptions required in this solution which could potentially improve the predictive capabilities of the model.

The model could also benefit for more complex functions for both the hydrostatic tissue pressure and the interaction terms. Building a depth and radius dependent function for hydrostatic tissue pressure both eliminate an unknown from the set of equations and provide a more intuitive model of hydrostatic tissue pressure. Finally, the more complex interaction terms could be incorporated to account for viscous effects between the solid and the blood constituents. Increases in complexity of both the hydrostatic pressure and interaction terms could potentially improve the predictive capabilities of the model.

CHAPTER 7. SUMMARY AND FUTURE WORK

Localized ischemia, impaired interstitial fluid flow, and sustained mechanical loading of cells have all been hypothesized as mechanisms of PrU etiology. Time-varying loading has been shown experimentally to increase fluid flow in human skin *in vivo*. Therefore there is a need for an analytical model to investigate the local fluid flow characteristics of skin tissue under time-varying loading. Moreover, models of neonatal PrUs are non-existent within literature. The objectives of this dissertation were to predict quasi-static stress distributions and time dependent velocity changes of tissues under static and time-varying loading conditions towards a better understanding of PrU etiology and prevention within the neonatal population.

Incompressible and compressible hyperelastic, neo-hookean quasi-static models were calibrated and validated using *in vivo* human skin compression data. Ultimately, the RMSE was minimized (0.2kPa) with the compressible model, and as such, the resultant material properties were utilized. Calibrated material properties were on the same order of magnitude as the few other data points reported in literature. Four different strain profiles were investigated to model neonatal O-PrUs and OC-PrUs including uniform, geometric circular segment, Gaussian, and Hertz strain profiles. The Gaussian profile was able to predict experimental maximum interface pressure data with the least error (<0.02%). Stress profiles and maximum strain were predicted for pre-term and term O-

PrUs and OC-PrUs. Predicted strain values were used to gain insight on stress thresholds for capillary occlusion and compared to the classic pressure-time threshold curve. By convention, 32mmHg (4.3kPa) is considered the threshold for capillary occlusion. Assuming complete capillary occlusions corresponds to $\varphi^b = 0$, model output suggests capillary occlusion is at a much higher stress.

Building upon the quasi-static model, a time dependent model was validated and calibrated to monitor fluid flow characteristics under time-varying loading conditions. Three different strain inputs were used, including uniform, circular segment, and Gaussian. The apparent strain magnitude and frequency of the input were varied from 100-700με and 10-80Hz, respectively. Interstitial fluid velocity was predicted using uniform, circular segment, and Gaussian models. Blood velocity was predicted using the uniform model.

In all models, interstitial fluid velocity and blood velocity were shown to increase significantly with increasing input frequency and amplitude. At the lowest amplitude and frequency, interstitial fluid velocity and blood velocity were on the same order of magnitude as reported in literature. Variation of the geometric circular segment model with skull radius demonstrated that larger skull sizes are more sensitive to changes in frequency. Investigation of fluid velocities beyond the skull radius using the Gaussian model showed significantly higher fluid velocities at 1.5R.

Towards the development of prophylactic and treatment protocols for clinical PrU management, the next steps are four-fold: 1.) to extend the model to include individual skin layers (separate models for epidermis, dermis, hypodermis, and muscle) 2.) to correlate maximum tissue strain to PrU occurrence, and 3.) to optimize the required

apparent strain amplitude and frequency inputs for a wide range of tissue parameter inputs (*i.e.* tissue thickness, initial solid volume fraction, bulk and shear modulus) such that the device is effective on a diverse range of patients (from neonates to elderly) and 4.) convert inputs into device design criteria.

Arguably the most useful feature of the model is the ability to vary input parameters to represent different patient populations from neonates to the elderly to those with spinal cord injuries. For example, in stark contrast to neonates, elderly patients have stiffer skin (higher shear modulus) and less fluid content (higher initial solid volume fraction). The model may be modified with these inputs to optimize design criteria specifically for the elderly population. Therefore, future work will ultimately result in a greater understanding of the response of skin tissue to time-varying loading across all patient populations if input parameters for each population set are utilized in optimization algorithms.

While patient specific optimization is possible, design across specific patient populations is more reasonable in the medical field. However, future iterations of device design might also include a feedback system which adjusts the amplitude and frequency of vibration in real-time to attain normal physiologic blood flow velocities. This results in a pseudo-patient specific design as the real-time input parameters are adjusted based on patient response to the device. The use of a feedback system eliminates the need for patient specific skin tissue properties, which may be expensive or invasive to acquire.

In conclusion, this study has demonstrated the ability to analytically predict quasi-static stress profiles as well as predict fluid velocity increases in cyclically loaded soft tissues by employing quasi-static mechanics and mixture theory models. Consequently,

this study builds a strong foundation for use in the development of vibrational support surfaces for use in prophylactic protocols and adjunctive treatment modalities for PrU management.

LIST OF REFERENCES

LIST OF REFERENCES

[1] Dorner, B., Posthauer, M. & Thomas, D. *The Role of Nutrition in Pressure Ulcer Prevention and Treatment: National Pressure Ulcer Advisory Panel White Paper* (National Pressure Ulcer Advisory Panel, 2009).

[2] *NPUAP Pressure Ulcer Stages/Categories*, <http://www.npuap.org/resources/educational-and-clinical-resources/npuap-pressure-ulcer-stagescategories/> (2014).

[3] Bouten, C., Oomens, C., Baaijens, F. & Bader, D. The Etiology of Pressure Ulcers: Skin Deep or Muscle Bound? *Arch Phys Med Rehabil* **84**, 616-619 (2003).

[4] Mak, A., Zhang, M. & Tam, E. Biomechanics of Pressure Ulcer in Body Tissues Interacting with External Forces During Locomotion. *Annu. Rev. Biomed. Eng.* **12**, 29-53 (2010).

[5] Cuddigan, J., Berlowitz, D. & Ayello, E. Pressure Ulcers in America: Prevalence, Incidence, and Implications for the Future: An Executive Summary of the National Pressure Ulcer Advisory Panel Monograph. *Advances in Skin and Wound Care* **14**, 208-215 (2001).

[6] *Evidence-based Practice Center Systematic Review Protocol Pressure Ulcer Treatment Strategies: A Comparative Effectiveness Review* (Agency for Healthcare Research and Quality, Online, 2011).

[7] Kuhn, B. & Coulter, S. Balancing the Pressure Ulcer Cost and Quality Equation. *Nursing Economics* **10**, 353-359 (1992).

[8] Whittington, K., Patrick, M. & Roberts, J. A National Study of Pressure Ulcer Prevalence and Incidence in Acute Care Hospitals. *Journal of Wound, Ostomy, and Continence Nursing* **27**, 209-215 (2000).

[9] David, G., Gunnarsson, C., Waters, H., Horblyuk, R. & Kaplan, H. Economic Measurement of Medical Errors Using a Hospital Claims Database. *Value in Health* **16**, 305-310 (2013).

[10] Reddy, M., Gill, S. & Rochon, P. Preventing Pressure Ulcers: A Systematic Review. *Journal of the American Medical Association* **296**, 974-984 (2006).

[11] Shreve, J. *et al.* The Economic Measurement of Medical Errors. (Society of Actuaries' Health Section, 2010).

[12] Milstein, A. Ending Extra Payment for "Never Events" - Stronger Incentives for Patients' Safety. *New England Journal of Medicine* **360**, 2388-2390 (2009).

[13] Bolton, J., Girolami, S. & Hurlow, J. The AAWC Pressure Ulcer Guidelines. *The American Journal of Nursing* **113**, 58-63 (2013).

[14] Gorecki, C. *et al.* Development of a conceptual framework of health-related quality of life in pressure ulcers: A patient-focused approach. *International Journal of Nursing Studies* **47**, 1525-1534 (2012).

[15] Graves, N., Birrell, F. & Whitby, M. Effect of Pressure Ulcers on Length of Hospital Stay. *Infection Control and Hospital Epidemiology* **26**, 293-297 (2005).

[16] Priebe, M., Martin, M., Wuermser, L., Castillo, T. & McFarlin, J. in *Spinal Cord Medicine: Principles and Practice* (Demos Medical Publishing, Inc.).

[17] Redelings, M., Lee, N. & Sorvillo, F. Pressure Ulcers: More Lethal Than We Thought? *Advances in Skin and Wound Care* **18**, 367-372 (2005).

[18] Reswick, J. & Rogers, J. in *Bedsore biomechanics.* (University Park Press).

[19] Sacks, A. Theoretical prediction of a time-at-pressure curve for avoiding pressure ulcers. *Journal of Rehabilitation Research and Development* **26**, 27-34 (1989).

[20] Reddy, M. *et al.* Treatment of Pressure Ulcers A Systematic Review. *Journal of the American Medical Association* **300**, 2647-2662 (2008).

[21] Levine, S., Sinno, S., Levine, J. & Saadek, P. Current Thoughts for the Prevention and Treatment of Pressure Ulcers: Using the Evidence to Determine Fact or Fiction. *Annals of Surgery* **257**, 603-608 (2013).

[22] Ostadabbas, S., Yousefi, R., Nourani, M., Faezipour, M. & Tamil, L. in *IEEE International Conference of Bioinformatics and Biomedicine.*

[23] McInnes, E., Jammali-Blasi, A., Bell-Syer, S., Dumville, J. & Cullum, N. Preventing pressure ulcers-Are pressure-redistributing support surfaces effective? A Cochrane systematic review and meta-analysis. *International Journal of Nursing Studies* **49**, 345-359 (2012).

[24] Still, M. *et al.* The Turn Team: A Novel Strategy for Reducing Pressure Ulcers in the Surgical Intensive Care Unit. *J Am Coll Surg* **216** (2013).

[25] Smith, M. *et al.* Pressure Ulcer Treatment Strategies A Systematic Comparative Effectiveness Review. *Annals of Internal Medicine* **159** (2013).

[26] Efraim, J. Assessment and Management of Pressure Ulcers in the Elderly: Current Strategies. *Drugs and Aging* **27**, 311-325 (2010).

[27] Coleman, S. *et al.* Patient risk factors for pressure ulcer development: Systematic review. *International Journal of Nursing Studies* **50**, 974-1003 (2013).

[28] Krause, J. Skin sores after spinal cord injury: relationship to life adjustment. *Spinal Cord* **36** (1998).

[29] Walter, J. *et al.* A database of self-reported secondary medical problems among VA spinal cord injury patients: its role in clinical care and management. *J Rehabil Res Dev* **39**, 53-61 (2002).

[30] Garber, S. & Rintala, D. Pressure ulcers in veterans with spinal cord injury: a retrospective study. *J Rehabil Res Dev* **40**, 433-441 (2003).

[31] Allman, R. Pressure ulcers among the elderly. *N Engl J Med* **320**, 850-853 (1989).

[32] Cox, J. Predictors of Pressure Ulcers in Adult Critical Care Patients. *American Journal of Critical Care* **20**, 364-375 (2011).

[33] Zollo, M., Gostisha, M., Berens, R., Schmidt, J. & Weigle, C. Altered Skin Integrity in Children Admitted to a Pediatric Intensive Care Unit. *Journal of Nursing Care Quality* **11**, 62-67 (1996).

[34] Schindler, C. *et al.* Protecting Fragile Skin: Nursing Interventions to Decrease Development of Pressure Ulcers in Pediatric Intensive Care. *Am J Crit Care* **20**, 26-34 (2011).

[35] Curley, M., Quigley, S. & Lin, M. Pressure ulcers in pediatric intensive care: incidence and associated factors. *Pediatr Crit Care Med* **4**, 284-290 (2003).

[36] Willock, J., Harris, C., Harrison, J. & Poole, C. Identifying the characteristics of children with pressure ulcers. *Nursing Times* **101**, 40-43 (2005).

[37] Zollo, M., Gostisha, M., Berens, R., Schmidt, J. & Weigle, C. Altered skin integrity in children admitted to a pediatric intensive care unit. *J Nurs Care Qual* **11**, 62-67 (1996).

[38] McLane, K., Bookout, K., McCord, S., McCain, J. & Jefferson, L. The 2003 National Pediatric Pressure Ulcer and Skin Breadown Prevalence Survey A Multisite Study. *Journal of Wound, Ostomy, and Continence Nursing* **31**, 168-178 (2004).

[39] Visscher, M. *et al.* A Quality-Improvement Collaborative Project to Reduce Pressure Ulcers in PICUs. *Pediatrics* **131** (2013).

[40] Lund, C., Kuller, J., Lane, A., Wright Lott, J. & Raines, D. Neonatal Skin Care: The Scientific Basis for Practice. *Neonatal Network* **18** (1999).

[41] Kanitakis, J. Anatomy, histology and immunohistochemistry of normal human skin. *Eur J Dermatol* **12**, 390-401 (2002).

[42] Marieb, E. & Hoehn, K. in *Human Anatomy and Physiology* Vol. 155 (Benjamin Cummings, 2010).

[43] Blank, I. & Scheuplein, R. Transport into and within the skin. *Br J Dermatol* **81**, 4-10 (1969).

[44] Behl, C. *et al.* Hydration and percutaneous absorption III: Influences of stripping and scalding on hydration alteration of the permeability of hairless mouse skin to water and n-alcholos. *J Pharm Sci* **71**, 229-234 (1982).

[45] Elias, P. Epidermal lipids, barrier function and desquamation. *J Invest Dermatol* **80**, 44s-49s (1983).

[46] Bommannan, D., Potts, R. & Guy, R. Examination of Stratum Corneum Barrier Function In Vivo by Infrared Spectroscopy. *Journal of Investigative Dermatology* **95**, 403-408 (1990).

[47] Lanir, Y. & Fung, Y. Two-Dimensional Mechanical Properties of Rabbit Skin-II Experimental Results. *J Biomechanics* **7**, 171-182 (1974).

[48] Bader, D. Mechanical characteristics of skin and underlying tissues in vivo. *Biomaterials* **4**, 305-308 (1983).

[49] Zahouani, H. *et al.* Characterization of the mechanical properties of a dermal equivalent compared with human skin in vivo by indentation and static friction tests. *Skin Research and Technology* **15** (2009).

[50] Pailler-Mattei, C., Bec, S. & Zahouani, H. In vivo measurements of the elastic mechanical properties of human skin by indentation tests. *Medical Engineering and Physics* **30** (2008).

[51] Agache, P., Monneur, C., Leveque, J. & De Rigal, J. Mechanical Properties and Young's Modulus of Human Skin in Vivo. *Arch Dermatol* **269**, 221-232 (1980).

[52] Tobin, D. Biochemistry of human skin - our brain on the outside. *Chem Soc Rev* **35**, 52-67 (2006).

[53] Geerlings, M., van Breeman, L. & Peters, G. In vitro indentation to determine the mechanical properties of epidermis. *j biomech* **44**, 1176-1181 (2011).

[54] Yuan, Y. & Verma, R. measuring microelastic properties of stratum corneum. *Colloids Surf B* **48**, 6-12 (2006).

[55] Jachowicz, J., McMullen, R. & Pretypaul, D. Indentometric analysis of in vivo skin and comparison with artificial skin models. *Skin Research and Technology* **13**, 299-309 (2007).

[56] Pailler-Mattei, C., Nicoli, S., Pirot, F., Vargiolu, R. & Zahouani, H. A new approach to describe the skin surface physical properties in vivo. *Colloids Surf B* **68**, 200-206 (2009).

[57] Pailler-Mattei, C. *et al.* Contribution of stratum corneum in determining bio-tribological properties of the human skin. *Wear* **263**, 1038-1043 (2007).

[58] Diridollou, S., Black, D., Lagarde, J. & Gall, Y. Sex- and site-dependent variations in the thickness and mechanical properties of human skin in vivo. *International Journal of Cosmetic Science* **22**, 421-435 (2000).

[59] Mak, A., Huang, L. & Wang, Q. A Biphasic Poroelastic Analysis of the Flow Dependent Subcutaneous Tissue Pressure and Compaction Due to Epidermal Loadings: Issues in Pressure Sore. *Journal of Biomechanical Engineering* **116**, 421-429 (1994).

[60] Bennett, L., Kavner, D., Lee, C. & Trainor, F. Shear vs Pressure as Causative Factors in Skin Blood Flow Occlusion. *Arch Phys Med Rehabil* **60**, 309-314 (1979).

[61] Bader, D. & Grant, C. Changes in Transcutaneous Oxygen Tension as a Result of Prolonged Pressures at the Sacrum. *Clin Phys Physiol Meas* **9**, 33-40 (1988).

[62] Michel, C. & Gillott, H. in *Pressure Sores: Clinical Practice and Scientific Approach* (ed DL Bader) 153-163 (The macMillan Press, 1990).

[63] Reddy, N. Interstitial Fluid Flow as a Factor in Decubitus Ulcer Formation. *J of Biomechanics* **14**, 879-881 (1981).

[64] Reddy, N. in *Tissue Nutrition and Viability* (ed AR Hargens) (Springer-Verlag, 1986).

[65] Reddy, N. in *Pressure Sores: Clinical Practice and Scientific Approach* (ed DL Bader) 203-220 (The macMillan Press, 1990).

[66] Sacks, A., O'Neill, H. & Perkash, I. Skin Blood Flow Changes and Tissue Deformations produced by Cylindrical Indentors. *J Rehab Research and Development*, 1-6 (1985).

[67] Braden, B. & Bergstrom, N. A conceptual shcema for the study of the etiology of pressure sores. *Rehabilitation Nursing* **12**, 8-12, 16 (1987).

[68] Whittington, K. & Briones, R. National Prevalence and Incidence Study: 6-Year Sequential Acute Care Data. *Adv Skin Wound Care* **17**, 490-494 (2004).

[69] *The Financial Impact of Pressure Ulcers: A review of the direct and indirect costs associated with pressure ulcers* (Leaf Healthcare, Inc, Pleasanton, CA).

[70] in *Pressure Ulcers in the Aging Population A Guide for Clinicians* (eds D. thomas & G. Compton) (Humana Press, 2014).

[71] Terms and Definitions Related to Support Surfaces. (2007).

[72] Nixon, J., McElvenny, D., Mason, S., Brown, J. & Bond, S. A sequential randomized controlled trial comparing a dry visco-elastic polymer pad and standard operating table mattress in the prevention of post-operative pressure sores. *Int J Nurs Stud.* **35**, 193-203 (1998).

[73] Jolley, D., Wright, R. & McGowan, S. Preventing pressure ulcers with the Australian Medical Sheep-skin: an open-label randomized controlled trial. *Med J Aust* **180**, 324-327 (2004).

[74] Russell, L., Reynolds, T. & Park, C. Randomized clinical trial comparing 2 support surfaces: results of the Prevention of Pressure Ulcers Study. *Adv Skin Wound Care* **16**, 317-327 (2003).

[75] Gray, D. & Smith, M. Comparison of a new foam mattress with the standard hospital mattress. *J Wound Care* **9**, 29-31 (2000).

[76] Hofman, A. *et al.* Pressure sores and pressure-decreasing mattresses: controlled clinical trial. *Lancet* **343**, 568-571 (1994).

[77] Santy, J., Butler, M. & Whyman, J. A comparison study of 6 types of hospital mattresses to determine which most effectively reduces the incidence of pressure sores in elderly patients with hip fractures in a District General Hospital: report to Norther & Yorkshire Regional Health Authority. (1994).

[78] Ewing, M., Garrow, C., Pressley, T., Ahsley, C. & Kinsella, N. Further experiences in the use of sheep-skin as an aid in nursing. *Med J Aust* **16**, 139-141 (1964).

[79] Conine, T., Daechsel, D. & Hershler, C. Pressure sore prophylaxis in elderly patients using slab foam or customized contoured foam wheelchair cushions. *Occup Ther J Res* **13**, 101-116 (1993).

[80] Baker, S., Smith, B., Donohue, P. & Gleason, C. Skin care management practices for premature infants. *J Perinatol* **19**, 426-431 (1999).

[81] Maguire, D. Skin protection and breakdown in the ELBW. A national survey. *Clin Nurse Res* **8** (1999).

[82] Lund, C. Prevention and management of infant skin breakdown. *Nurs Clin North Am* **34** (1999).

[83] Vanderwee, K., Grypdonck, M. & DeFloor, T. Effectiveness of an alternating pressure air mattress for the prevention of pressure ulcers. *Age Ageing* **34**, 261-267 (2005).

[84] Anderson, K., Jenson, O., Kvorning, S. & Bach, E. Decubitus prophylaxis: a prospective trial on the efficiency of alternating-pressure air-mattresses and water-mattresses. *Acta Derm Venereal* **63**, 227-230 (1983).

[85] Norton, D., McLaren, R. & Exton-Smith, A. *An investigation of geriatric nursing problems in hospital*. (Churchill Livingstone Edinburgh, 1975).

[86] Bergstrom, N. Repositioning as a Pressure Ulcer Prevention Strategy: A Multi-site Clinical Trial. (National Pressure Ulcer Advisory Panel).

[87] Bergstrom, N. *et al.* Turning for Ulcer ReductioN: A Multisite Randomized Clinical Trial in Nursing Homes. *Journal of the American Geriatrics Society* **61** (2013).

[88] Defloor, T., De Bacquer, D. & Grypdonck, M. The effect of various combinations of turning and pressure reducing devices on the incidence of pressure ulcers. *Int J Nurs Stud.* **42**, 37-36 (2005).

[89] Bourdel-Marchasson, I., Barateau, M. & Rondeau, V. A multi-center trial of the effects of oral nutritional supplementation in critically ill older inpatients. *Nutrition* **16**, 1-5 (2000).

[90] Berlowitz, D. & Wilking, S. Risk factors for pressure sores. A comparison of cross-sectional and cohort-derived data. *Journal of the American Geriatrics Society* **37**, 1043-1050 (1989).

[91] Bergstrom, N., Braden, M., Laguzza, A. & Holman, V. A prospective study of pressure sore risk among institutionalized elderly. *Journal of the American Geriatrics Society* **40**, 747-758 (1992).

[92] Breslow, R. Nutritional status and dietary intake of patients with pressure ulcers: review of research literature 1943 to 1989. *Decubitus* **4**, 16-21 (1991).

[93] Finucane, T. Malnutrition, tube feeding and pressure sores: data are incomplete. *Journal of the American Geriatrics Society* **43**, 447-451 (1995).

[94] Strauss, E. & Margolis, D. Malnutrition in patients with pressure ulcers: morbidity, mortality, and clinically practical assessments. *Advances in Wound Care* **9**, 37-40 (1996).

[95] Langer, G. & Fink, A. Nutritional interventions for preventing and treating pressure ulcers (Review). *The Cochrane Library* (2014).

[96] Willock, J. Interrater reliability of the Glamorgan Scale: overt and covert data. *British Journal of Nursing* **22** (2013).

[97] Jankowski, I. & Nadzam, D. Identifying Gaps, Barriers, and Solutions in Implementing Pressure Ulcer Prevention Programs. *The Joint Commission Journal on Quality and Patient Safety* **37**, 253-264 (2011).

[98] Braden, B. & Bergstrom, N. Predictive validity of the Braden scale for pressure sore risk in a nursing home population. *Research Nursing Health* **17**, 459-470 (1994).

[99] Prevention and Treatment of Pressure Ulcers: Quick Reference Guide. (European Pressure Ulcer Advisory Panel and National Pressure Ulcer Advisory Panel, 2009a).

[100] Treatment of pressure ulcers: Quick Reference Guide. (European Pressure Ulcer Advisory Panel and National Pressure Ulcer Advisory Panel, 2009b).

[101] Ovington, L. Essential fatty acids lubricate skin, prevent pressure sores. *Wound Care* **43**, 48-52,54 (1998).

[102] Torra i Bou, J., Segovia Gomez, T., Verdu Soriano, J. & al., e. The effectiveness of a hyperoxygentated fatty acid compound in preventing pressure ulcers. *J Wound Care* **14**, 117-121 (2005).

[103] Declair, V. The usefulness of topical application of essential fatty acids (EFA) to prevent pressure ulcers. *Ostomy/Wound Management* **43**, 48-52, 54 (1997).

[104] Sibbald, R., Williamson, D., Orsted, H. & al., e. Preparing the wound bed-debridement, bacterial balance, and moisture balance. *Ostomy Wound Manage* **46**, 14-35 (2000).

[105] Russell, L. *et al.* Randomized comparison trial of the RIK and the Nimbus 3 mattresses. *Br J Nurs* **12**, 254, 256-259 (2003).

[106] Nixon, J., Granny, G. & Iglesias, C. Randomized, controlled trial of alternating pressure mattresses compared with alternating pressure overlays for the prevention of pressure ulcers: PRESSURE (Pressure Relieving Support Surfaces) trial. *BMJ* **332**, 1413-1415 (2006).

[107] Rosenthal, M. *et al.* Healing of advanced pressure ulcers by a generic total contact seat: 2 randomized comparisons with low air loss bed treatments. *Arch Phys Med Rehabil* **84**, 1733-1742 (2003).

[108] Ferrell, B., Osterweil, D. & Christenson, P. A randomized trial of low-air-loss beds for treatment of pressure ulcers. *Journal of the American Medical Association* **269**, 494-497 (1993).

[109] Branom, R. "Constatn force technology" vs low-air-loss therapy in the treatment of pressure ulcers. *Ostomy Wound Manage* **47**, 38-46 (2001).

[110] Mulder, G., Taro, N., Seeley, J. & Andrews, K. A study of pressure ulcer response to low air loss beds vs conventional treatment. *J Geriatr Dermatol* **2**, 87-91 (1994).

[111] Allman, R. *et al.* Air-fluidized beds or conventional therapy for pressure sores: a randomized trial. *Ann Intern Med* **107**, 641-648 (1987).

[112] Evans, D., Land, L. & Geary, A. A clinical evaluation of the Nimbus 3 alternating pressure mattress replacement system. *J Wound Care* **9**, 181-186 (2000).

[113] Desneves, K. Treatment with supplementary arginine, vitamin C and zinc in patients with pressure ulcers: A randomized controlled trial. *Clinical Nutrition* **24**, 979-987 (2005).

[114] Lee, S. Pressure ulcer healing with a concentrated, fortified, collagen protein hydrolysate supplement: a randomized controlled trial. *Adv Skin Wound Care* **19**, 92-96 (2006).

[115] ter Riet, G., Kessels, A. & Knipschild, P. Randomized clinical trial of ascorbic acid in the treatment of pressure ulcers. *J Clin Epidemiol* **48**, 1453-1460 (1995).

[116] Taylor, T., Rimmer, S., Day, B., Butcher, J. & Dymock, I. Ascorbic acid supplementation in the treatment of pressure sores. *Lancet* **2**, 544-546 (1974).

[117] Stechmiller, J., Childress, B. & Cowan, L. Arginine supplemenation and wound healing. *Nutr Clin Pract* **20**, 52-61 (2005).

[118] Barbul, A., Lazarou, S., Efron, D., Wasserkrug, H. & Efron, G. Arginine enhances wound healing and lymphocyte immune response in humans. *Surgery* **108**, 331-337 (1990).

[119] Kirk, S. *et al.* Arginine stimulates wound healing and immune function in elderly human beings. *Surgery* **1993** (1993).

[120] Benati, G., Delvecchio, S., Cilla, D. & Pedone, V. Impact on pressure ulcer healing of an arginine-enriched nutritional solution in patients with severe cognitive impairment. *Arch Gerontol Geriatr*, 43-47 (2001).

[121] Sayag, J., Meaume, S. & Bohbot, S. Healing properties of calcium alginate dressings. *J Wound Care* **5**, 357-362 (1996).

[122] Gerding, G. & Browning, J. Oxyquinoline-containing ointment vs standard therapy for stage I and stage II skin lesions. *Dermatol Nurs* **4**, 289-298 (1992).

[123] Rees, R., Robson, M., Smiell, J. & Perry, B. Becaplermin gel in the treatment of prssure ulcers: a phase II randomized, double-blind, placebo-controlled study. *Wound Repair Regen* **7**, 141-147 (1999).

[124] Landi, F., Aloe, L. & Russo, A. Topical treatment of pressure ulcers with nerve growth factor: a randomized clinical trial. *Ann Intern med* **139**, 635-641 (2003).

[125] Ubbink, D. T., Westerbos, S. J., Evans, D., Land, L. & Vermeulen, H. Topical negative pressure for treating chronic wounds. *The Cochrance database of systemic reviews* **3** (2008).

[126] Moues, C., Heulle, F. & Hovius, S. A review of topical negative pressure therapy in wound healing: sufficient evidence? *The American Journal of Surgery* **201**, 544-556 (2011).

[127] Luther, K. & McCulloch, J. Promotion of Wound Healing with Electrical Stimulation. *Advances in Skin and Wound Care* **9**, 42-45 (1996).

[128] Akbari Sari, A., Flemming, K., Cullum, N. & Wollina, U. Theraputic ultrasound for pressure ulcers. *The Cochrance database of systemic reviews* (2006).

[129] Aziz, Z., Flemming, K., Cullum, N. & Manesh, A. Electromagnetic therapy for treating pressure ulcers. *The Cochrance database of systemic reviews* (2010).

[130] Lucas, C., Coenen, C. & De Haan, R. The Effect of Low Level Laser Therapy (LLLT) on Stage III Decubitus Ulcers (Pressure Sores); a Prospective Randomised Single Blind, Multicentre Pilot Study. *Lasers in Medical Science* **15**, 94-100 (2000).

[131] Durovic, A., Maric, D., Jevtic, M. & Durdevic, S. The effects of polarized light therapy in pressure ulcer healing. *Vojnosanit Pregl.* **65** (2008).

[132] Ho, C., Bensitel, T., Wang, X. & Bogie, K. Pulsatile Lavage for the Enhancement of Pressure Ulcer Healing: A Randomized Controlled Trial. *Phys Ther* **92**, 38-48 (2012).

[133] Andusky, A. & Ohry, A. Decubitus direct current treatment (DDCT) of pressure ulcers: results of a randomized double-blinded placebo controlled study. *Arch Gerontol Geriatr* **41**, 261-269 (2005).

[134] Tally, A., Sivaraman Nair, K., Murali, T. & John, A. Efficacy of multiwavelength light therapy in the treatment of pressure ulcers in subjects with disorders of the spinal cord: a randomized double-blind controlled trial. *Arch Phys Med Rehabil* **85**, 1657-1661 (2004).

[135] CA, S., Cooper-Vastola, S., Perez, F., Viehbeck, M. & Byrne, D. The effects of non-thermal pulsed electromagnetic energy on wound healing of pressure ulcers in spinal cord-injured patients: a randomized, double-blind study. *Ostomy Wound Manage* **41**, 42-51 (1995).

[136] Comorosan, S. *et al.* The effect of Diapulse therapy on the healing of decubitus ulcer. *Rom J Physiol* **30**, 41-45 (1993).

[137] Dehlin, O., Elmstahl, S. & Gottrup, F. Monochromatic phototherapy in elderly patients: a new way of treating chronic pressure ulcers? *Aging Cli Exp Res.* **15**, 259-263 (2003).

[138] Lund, C. & Osborne, J. Validity and reliability of the neonatal skin condition score. *Journal of Obstetric Gynecologic Neonatal Nursing* **33**, 320-327 (2004).

[139] Razmus, I., Lewis, L. & Wilson, D. Pressure Ulcer Development in Infants: State of the Science. *Journal for Healthcare Quality* **30**, 36-42 (2008).

[140] Kravchenko, I. & Maibach, H. in *Beonatal Skin: Structure and Function* (eds SB Hoath & HI Maibach) 285-298 (Marcel Dekker, 2003).

[141] Chiou, Y. & Blume-Peytavi, U. Stratum Corneum Maturation. *Skin Pharmacol Physiol* **17**, 57-66 (2004).

[142] Kalia, Y., Nonato, L., Lund, H. & Guy, R. Development of skin barrier function in premature infants. *J Invest Dermatol* **111**, 320-326 (1998).

[143] Rutter, N. & Hull, D. Water loss from the skin of term and preterm babies. *Arch Dis Child* **54**, 858-868 (1979).

[144] Harpin, V. & Rutter, N. Barrier properties of newborn skin *J Pediatr* **103**, 419-425 (1983).

[145] Visscher, M., Chatterjee, R., Munson, K., Pickens, W. & Hoath, S. Changes in diapered and nondiapered infant skin over the first month of life. *Pediatr Dermatol* **17**, 45-51 (2000).

[146] Murray, J., Noonan, C., Quigley, S. & Curley, M. Medical Device-Related Hospital-Acquired Pressure Ulcers in Children: An Integrative Review. *Journal of Pediatric Nursing* **28** (2013).

[147] Curley, M., Razmus, I., Roberts, K. & Wypij, D. Predicting pressure ulcer risk in patients: The Braden Q Scale. *Nursing Research* **52**, 22-33 (2003).

[148] Boesch, R. *et al.* Prevention of tracheostomy-related Pressure Ulcers in Children. *Pediatrics* **129**, e792-e797 (2011).

[149] Razmus, I., Roberts, K. & Curley, M. Pressure ulcers in critically ill children: Incidence and associated factors. *Critical Care Medicine* **29** (2001).

[150] Neidig, J., Kleier, C. & Oppliger, R. Risk factors associated with pressure ulces in the pediatric patient following open-heart surgery. *Progress in Cardiovascular Nursing* **4**, 99-106 (1989).

[151] Wu, G., Jaeger, L., Bazer, F. & Rhoads, J. Arginine deficiency in preterm infants: biochemical mechanisms and nutritional implications. *J Nutr Biochem* **15**, 442-451 (2004).

[152] Turnage-Carrier, C., McLane, K. & Gregurich, M. Interface Pressure Comparison of Healthy Premature Infants with Various Neonatal Bed Surfaces. *Advances in Neonatal Care* **8**, 176-184 (2008).

[153] Solis, I., Krouskop, T., Trainer, N. & Marburger, R. Supine Interface Pressure in Children. *Arch Phys Med Rehabil* **69** (1988).

[154] Waterlow, J. Pressure sore risk assessment in children. *Paediatric nursing* **9**, 21-24 (1997).

[155] McCord, S. *et al.* Negative pressure therapy is effective to manage a variety of wounds in infants and children. *Wound Repair Regen* **15**, 296-301 (2007).

[156] McPherson, G. & Kriewall, T. The elastic modulus of fetal cranial bone: A first step toward understanding of the biomechanics of fetal head molding. *Journal of Biomechanics* **13**, 9-16 (1980).

[157] Sweeney, J. & Gutierrez, T. Musculoskeletal Implications of Preterm Infant Positioning in the NICU. *Journal of Perinatal and Neonatal Nursing* **16**, 58-70 (2002).

[158] van Lindert, E. *et al.* Validation of cephalic index measurements in scaphocephaly. *Childs Nerv Systm* **29**, 1007-1014 (2013).

[159] Likus, W. *et al.* Cephalic Index in the First Three Years of Life: Study of Children with Normal Brain Development Based on Computed Tomography. *The Scientific World Journal*, 1-6 (2014).

[160] *Craniosynostosis: Diagnosis, Evaluation, and Management*. 2 edn, 480 (Oxford University Press, 2000).

[161] McManus, B. & Capistran, P. A case presentation of early intervention with dolichocephaly in the NICU: collaboration between the primary nursing team and the developmental care specialist. *Neonatal Network* **27**, 307-315 (2008).

[162] *Dolichocephaly*, <http://elementsofmorphology.nih.gov/index.cgi?tid=e09c1185a1ef3e38> (2014).

[163] Graham, J. *et al.* Deformational brachycephaly in supine-sleeping infants. *The Journal of Pediatrics* **146**, 253-257 (2005).

[164] *Before and after treatment results*, <http://www.cranialtech.com/index.php?option=com_content&view=category&layout=blog&id=43&Itemid=72> (2011).

[165] Baker, D. & Berdon, W. Special trauma problems in children. *Radiol Clin North Am* **4**, 289-305 (1966).

[166] Cotter, S. A screening design for factorial experiments with interactions. *Biometrika* **66**, 317-320 (1979).

[167] Schuff, M., Gore, J. & Nauman, E. A mixture theory model of fluid and solute transport in the microvasculature of normal and malignant tissues. II: Factor sensitivity analysis, calibrtion, and validation. *J. Math. Biol.* **67**, 1307-1337 (2013).

[168] Cook, D., Julias, M. & Nauman, E. Biological variability in biomechanical engineering research: significance and meta-analysis of current modeling practices. *J Biomech* **47**, 1241-1250 (2014).

[169] Prange, M. *et al.* Mechanical Properties and Anthropometry of the Human Infant Head. *Stapp Car Crash Journal* **48**, 279-299 (2004).

[170] Bertino, E. *et al.* Neonatal Anthropometric Charts: the Italian Neonatal Study Compared with Other European Studies. *JPGN* **51**, 353-361 (2010).

[171] Cole, T., Williams, A. & Wright, C. Revised birth centiles for weight, length and head circumference in the UK-WHO growth charts. *Annals of Human Biology* **38**, 7-11 (2011).

[172] Donnelly, J., Walsh, J., Byrne, J., Molloy, E. & McAuliffe. Impact of maternal diet on neonatal antrhopometry: a randomized controlled trial. *Pediatric Obesity* (2014).

[173] Teletar, B., Comert, S., Vitrinel, A. & Erginoz, E. Anthropometric measurements of term neonates from a state hospital in Turkey. *Eastern Mediterranean health Journal* **15**, 1412-1419 (2009).

[174] Ludwig, D. & Currie, J. The association between pregnancy weight gain and birthweight: a within-family comparison. *The Lancet* **376**, 984-990 (2010).

[175] Marcellus, L. Determination of Positional Skin-Surface Pressures in Premature Infants. *Neonatal Network* **23** (2004).

[176] Chow, W. & Odell, E. Deformations and Stresses in Sodt Body Tissues of a Sitting Person. *Journal of Biomechanical Engineering* **100**, 79-87 (1978).

[177] Lanir, Y. Constitutive Equations for Fibrous Connective Tissues. *J Biomechanics* **16**, 1-12 (1983).

[178] Mow, V., Kuei, S., Lai, W. & Armstrong, C. Biphasic Creep and Stress Relaxation of Articular Cartilage Compression: Theory and Experiements. *Journal of Biomechanical Engineering* **120**, 73-84 (1980).

[179] Oomens, C. & van Campen, D. A Mixture Approach to the Mechanics of Skin. *J Biomechanics* **20**, 877-885 (1987).

[180] Agam, L. & Gefen, A. Toward real-time detection of deep tissue injury risk in wheelchair users using Hertz contact theory. *Journal of Rehabilitation Research and Development* **45**, 537-550 (2008).

[181] Gefen, A. How do microclimate factores affect the risk for superficial pressure ulcers: A mathematical modeling study. *Journal of Tissue Viability* **20**, 81-88 (2011).

[182] Hung, A., Mithraratne, K., Sagar, M. & Hunter, P. Multilayer Soft Tissue Continuum Model: Towards Realistic Simulation of Facial Expressions. *World Academy of Science, Engineering, and Technology* **3**, 112-116 (2009).

[183] Makhsous, M. *et al.* Finite Element Analysis for Evaluation of PRessure Ulcer on the Buttock: Development and Validation. *IEEE Transactions on Neural Systems and Rehabiliation Engineering* **15**, 517-525 (2007).

[184] Shaked, E. & Gefen, A. Modeling the effects of moisture-related skin-support friction on the risk for superficial pressure ulcers during patient repositioning in bed. *Fronteirs in Bioengineering and Biotechnology* **1**, 1-7 (2013).

[185] Solovyev, A., Mi, Q., Tzen, Y., Brienza, D. & Vodovotz, Y. Hybrid Equation/Agent-Based Model of Ischemia-induced Hyperemia and Pressure Ulcer Formation Predicts Greater Propensity to Ulcerate in Subjects with Spinal Cord Injury. *Computational Biology* **9** (2013).

[186] Stern, J., Ziraldo, C., Vodovotz, Y. & An, G. in *Complex Systems and Computational Biology Approaches to Acute Inflammation* (eds Y Vodovotz & G An) 209-226.

[187] Ziraldo, C., Mi, Q., An, G. & Vodovotz, Y. Computational Modeling of Inflammation and Wound Healing. *Advances in Wound Care* **2**, 527-537 (2013).

[188] Kosiak, M. Etiology and Pathology of Ischemic Ulcers. *Archives of Physical Medicine and Rehabiliation* **40**, 62-69 (1959).

[189] Sangeorzan, B., Harrington, R., Wyss, C., Czerniecki, J. & Matsen, F. Circulatory and Mechanical Response of Skin to Loading. *J Ortho. Research* **7**, 425-431 (1989).

[190] Snashell, P., Lucas, J., Guz, A. & Floyer, M. Measurement of Interstitial Fluid Pressure by Means of a Cotton Wick in Manand Animals: An analysis on the origin of the presssure. *CLinical Science* **41** (1971).

[191] Husain, T. An Experimental Study of Some Pressure Effects on Tissues with Reference to the Bed-sore Problem. *J Path & Bact* **66**, 347-358 (1953).

[192] Reger, S., McGovern, T. & Chung, K. in *Pressure Sores: Clinical Practice and Scientific Approach* (ed DL Bader) 177-190 (1990).

[193] Shilo, M. & Gefen, A. Identification of capillary blood pressure levels at which capillary collapse is likely in a tissue subjected to large compressive shear deformations. *Computer Methods in Biomechanics and Biomedical Engineering* **15**, 59-71 (2012).

[194] Dickerson, D., Sander, E. & Nauman, E. Modeling the mechanical consequences of vibratory loading in the vertebral body: microscale effects. *Biomechan Model Mechanobiol* **7**, 191-202 (2008).

[195] Salzetein, R., Pollack, S., Mak, A., Petron, N. & Brankov, G. Electromechanical Potentials in Cortical Bone Part I: A Continuum Approach. *J Biomechanics* **20**, 681-692 (1987).

[196] Torzilli, P. & Mow, V. On the Fundamental Fluid Transport Mechanisms Through Normal and Pathological Articular Cartilage During Function, Part II: The Analysis, Solution, and Conclusions. *J Biomechanics* **9**, 587-606 (1976).

[197] Taber, L., Yang, M., Keller, B. & Clark, E. in *1991 Advances in Bioengineering* (ed R Vanderby) 623-626 (ASME, 1992).

[198] Malvern, L. *Introduction to the Mechanics of a Continuous Medium*. (Prentice-Hall, Inc., 1969).

[199] Black, M. A modified radiographic method for measuring skin thickness. *British Journal of Dermatology* **81** (1969).

[200] Shuster, S., Black, M. & McVitie, E. The influence of age and sex on skin thickness, skin collagen and density. *British Journal of Dermatology* **93** (1975).

[201] van Beekvelt, M. C. P., Borghuis, M. S., van Engelen, B. G. M., Wevers, R. A. & Colier, W. N. J. M. Adipose tissue thickness affects in vivo quantitative near-IR spectroscopy in human skeletal muscle. *Clinical Science* **101**, 21-28 (2001).

[202] Himes, J., Roche, A. & Siervogel, R. M. Compressibility of skinfolds and the measurement of subcutaneous fatness. *The American Journal of Clinical Nutrition* **32**, 1734-1740 (1979).

[203] Nathanson, S. D. & Nelson, L. Interstitial fluid pressure in breast cancer, benign breast conditions and breast parenchyma. *Annals of Surgical Oncology* **1**, 333-338 (1994).

[204] Guyton, A. C. *Textbook of Medical Physiology*. (W. B. Saudners, 2000).

[205] Leunig, M. *et al.* Angiogenesis, microvascular architexture, microhemodynamics, and interstitial fluid pressure during early growth of human adenocarcinoma. *Cancer Research* **52**, 6553-6560 (1992).

[206] Silver, F., Seehra, G., Freeman, J. W. & DeVore, D. Viscoelastic properties of young and old human dermis: a proposed molecular mechanism for elastic energy storagae in collagen and elastin. *Journal of Applied Polymer Science* **86**, 1978-1985 (2002).

[207] *Computational Biophysics of the Skin*. (Pan Stanford Publishing, 2014).

[208] Tilleman, T., Tilleman, M. & Neumann, M. The Elastic Properties of Cacerous Skin: Poisson's Ratio and Young's Modulus. *Israel Medical Association Journal* **12**, 753-755 (2004).

[209] Brandis, K. (Anaesthesia Education Website).

[210] Dinsdale, S. Decubitus ulcers: role of pressure and friction in causation. *Arch Phys Med Rehabil* **55**, 147-152 (1974).

[211] Hobson, D. Comparative effects of posture on pressure and shear at the body-seat interface. *Journal of Rehabilitation Research and Development* **29**, 21-31 (1992).

[212] Linder-Ganz, E. Mechanical compression-induced pressure sores in rat hindlimb: muscle stiffness, histology , and computational models. *J Appl Physiol* **96**, 2034-2049 (2004).

[213] Reddy, N., Patel, H., Cochran, G. & Brunski, J. Model Experiments to Study the Stress Distributions in a Seated Buttock. *J. Biomechanics* **15**, 493-504 (1982).

[214] Todd, B. & Thacker, J. in *RESNA International*. 222-224.

[215] Linder-Ganz, E., Yarnitzky, G., Yizhar, Z., Siev-Ner, I. & Gefen, A. Real-Time Finite Element Monitoring of Sub-Dermal Tissue Stresses in Individuals with Spinal Cord Injury: Toward Prevention of Pressure Ulcers. *Annals of Biomedical Engineering* **37**, 387-400 (2009).

[216] Mclane, K., Krouskop, T., McCord, S. & Fraley, J. Comparison of Interface Pressures in the Pediatric Population Among Various Support Surfaces. *Journal of Wound, Ostomy, and Continence Nursing* **29**, 242-251 (2002).

[217] Farr, V. Skinfold Thickness as an Indication of Maturity of the Newbown. *Arch. Dis. Childh.* **41** (1966).

[218] Gampel, B. The Relation of Skinfold Thickness in the Neonate to Sex, Length of Gestation, Size at Birth, and Maternal Skinfold. *Human Biology* **37**, 29-37 (1965).

[219] Oakley, J., Parsons, R. & Whitelaw, A. Standards for skinfold thickness in British newborn infants. *Archives of Disease in Childhood* **52**, 287-290 (1977).

[220] Sumners, J., Gatchina, M., Findley, R. & Ferguson, K. Evaluation Methods for Intrauterine Growth Using Neonatal Fat Stores Instead of Birth Weigth as Outcome Measures: Fetal and Neonatal Measurements Correlated with Neonatal Skinfold Thickness. *J Clinical Ultrasound* **18**, 9-14 (1990).

[221] Haycock, G., Schwartz, G. & Wisotsky, D. Geometric method for measuring body surface area: A height-weight formula validated in infants, children, and adults. *J Pediatr* **93**, 62-66 (1978).

[222] Brion, L., Fleishman, A. & Schwartz, G. Evaluation of four length-weight formulas for estimating body surface area in newborn infants. *J Pediatr* **107**, 801-803 (1985).

[223] Sivieri, E., Gerdes, J. & Abbasi, S. Effect of HFNC Flow Rate, Canuula Size, and Nares Diameter on Generated Airway Pressures: An In Vitro Study. *Pediatric Pulmonology* **48**, 506-514 (2013).

[224] Ramanathan, R. Nasal respiratory support through the nares: its time has come. *Journal of Perinatology* **30**, S67-S72 (2010).

[225] Galaktionov, V. & Vazquez, J. The Problem of Blow-Up in Nonlinear Parabolic Equations. *Discrete and Continuous Dynamical Systems* **8**, 399-433 (2002).

[226] Russ, G. & Motta, G. Eliminating pressure: is less than 32 mmHg enough for wound healing? *Osomy Wound Manage* **34**, 60-63 (1991).

[227] Gupta, V. & Grande-Allen, J. Effects of static and cyclic loading in regulating extracellular matrix sythesis by cardiovasacular cells. *Cardiovascular Research* **72**, 375-383 (2006).

[228] Guyton, A., Frank, M. & Abernathy, B. A Concept of Negative Interstitial Pressure Based on Pressurs in Implanted Perforated Capsules. *Circulation Research* **12**, 399-414 (1963).

[229] Nakagawa, N., Matsumoto, M. & Sakai, S. In vivo measurement of the water content in the dermis by confocal Raman spectroscopy. *Skin Research and Technology* **16**, 137-141 (2010).

[230] Maloney-Hinds, C. & Petrofsky, J. The effect of 30 Hz vs. 50 Hz passive vibration and duration of vibration on skin blood flow in the arm. *Med Sci Monit* **14**, 112-116 (2008).

[231] Nakagami, G. *et al.* Effect of vibration on skin blood flow in an in vivo microcirculatory model. *Bioscience Trends* **1**, 161-166 (2007).

[232] Rubin, C. *et al.* Mechanical strain, induced noninvasively in the high-frequency domain, is anabolic to cancellous bone, but not cortical bone. *Bone* **30**, 445-452 (2002).

[233] Rubin, C. *et al.* Quantity and quality of trabecular bone in the femur are enhanced by a strongly anabolic, noninvasive mechanical intervention. *J Bone Miner Res* **17**, 349-357 (2002).

[234] Judex, S., Donahue, L. & Rubin, C. Genetic predisposition to low bone mass is paralleled by an enhanced sensitivity to signals anabolic to the skeleton. *Faseb J* **16**, 1280-1282 (2002).

[235] Judex, S. *et al.* Adaptations of trabecular bone to low magnitude vibrations result in more uniform stress and strain under load *Ann Biomed Eng* **31**, 12-20 (2003).

[236] Rubin, C. *et al.* Prevention of postmenopausal bone loss by a low-magnitude, high-frequency mechanical stimuli: a clinical trial assessing compliance, efficacy, and safety. *J Bone Miner Res* **19**, 343-351 (2004).

[237] Ward, K. *et al.* Low magnitude mechanical loading is osteogenic in children with disabling conditions. *J Bone Miner Res* **19**, 360-369 (2004).

[238] Weinheimer-Haus, E., Judex, S., Ennis, W. & Koh, T. Low-Intensity Vibraiton Improves Angiogenesis and Wound Healing in Diabetic Mice. *PLoS ONE* **9** (2014).

[239] Leduc, A., Lievens, P. & Dewald, J. The influence of multidirectional vibrations on wound healing and on regeneratoin of blood- and lymph vessels. *Lymphology* **14**, 179-185s (1981).

[240] Peer, K., Barkley, J. & Knapp, D. The Acute Effects of Local Vibration Therapy on Ankle Sprain and Hamstring Strain Injuries. *The Physician and Sports Medicine* **37**, 31-38 (2009).

[241] Arashi, M. *et al.* Vibration therapy accelerates healing of State I pressure ulcers in older adult patients. *Adv Skin Wound Care* **23** (2010).

[242] Sari, Y. *et al.* Vibration inhibits deterioration in rat deep-tissue injury through HIF1-MMP axis. *Wound Repair Regen* (2015).

[243] Velez-Diaz-Pallares, M. *et al.* Nonpharmacologic Interventions to Heal Pressure Ulcers in Older Patients: An Overview of Systematic Reviews *Journal of the American Medical Directors Association* (2015).

[244] Boer, P. *et al.* Blood to interstitial fluid volume ration in chronic hypokalaemic states. *European Journal of Clinical Investigation* **15**, 276-280 (1985).

[245] Boer, P. Estimated lean body mass as an index for normalizatoin of body fluid volumes in humans. *Am J Physiol* **247**, 632-636 (1984).

[246] Fels, I. Hydration and Density of Collagen and Gelatin. *Journal of Applied Polymer Science* **8**, 1813-1824 (1964).

[247] Gu, J., Mao, W., Lai, X. & Mow, V. in *Orthopaedic Research Society.*

[248] Schuff, M. *Multiphysics Models of Fluid and Solute Transport in the Microvasculature of Normal and Malignant Breast Tissues with Application to the Detection and Treatment of Breast Cancer* Doctor of Philosophy thesis, Purdue University, (2010).

[249] Huang, C. Effect of negative pressure on wound therapy on wound healing. *Curent Problems in Surgery* **51**, 301-331 (2014).

[250] Yao, W., Li, Y. & Ding, G. Interstitial Fluid Flow: The Mechanical Environment of Cells and Foundation of Meridians. *Evidence-Based Complementary and Alternative Medicine* **2012**, 1-9 (2012).

[251] Chary, S. & Jain, R. K. Direct measurement of interstitial convection and diffusion of albumin in normal and neoplastic tissues by fluoresence photobleaching. *Proc Natl Acad Sci USA* **86**, 5385-5389 (1989).

[252] Ng, C., Hinz, B. & Swartz, M. Interstitial fluid flow induces myofibroblast differentiation and collagen alignment in vitro. *Journal of Cell Science* **118**, 4731-4739 (2005).

[253] Fischer, M. *et al.* Flow velocity of single lymphatic capillaries in human skin. *American Journal of Physiology - Heart and Circulatory Physiology* **270** (1996).

[254] Norman, M., Herin, P., Fagrell, B. & Zetterstrom, R. Capillary Blood Cell Velocity in Full-Term Infants as Determined in Skin by Videophotometric Microscopy. *Pediatric Research* **23**, 585-588 (1988).

[255] Norman, M., Fagrell, C. & Herin, P. Effects of neonatal Polycythemia and Hemodilution on Capillary Perfusion. *The Journal of Pediatrics* **121**, 103-108 (1992).

[256] Daniel, R., Priest, D. & Wheatley, D. Etiologic factors in pressure sors: an experimental model. *Arch PHys Med Rehabil* **62**, 492-498 (1982).

[257] Kosiak, M. Etiology of decubitus ulcers. *Arch PHys med Rehabil* **42**, 19-29 (1961).

[258] Miller, G. & Seale, J. Lymphatic clearence during compressive loading. *Lymphology* **14**, 161-166 (1981).

[259] Barbenel, J. Pressure management. *Prosthet Orthot Int* **15**, 225-231 (1991).

[260] Atance, J., Bader, D. & Lee, D. Mechanical conditioning influences the metabolic response of cell-seeded constructs. *Cells Tissues Organs* **175**, 140-150 (2003).

[261] Grossi, A., Yadav, K. & Lawson, M. Mechanical stimulation increases proliferation, differentiation and protein expression in culture: stimulation effects are substrate dependent. *J Biomech* (2007).

[262] Petroll, W., Vishwanath, M. & Ma, L. Corneal fibroblasts respond rapidly to changes in local mechanical stress. *Invest Ophthalmol Vis Sci* **45**, 3466-3474 (2004).

APPENDICES

Appendix A. Experimental Setup by Bader et. al

Calibrations of the solid constituent material model utilized *in vivo* human skin tissue compression data collected by Bader *et al.*[48]. The study acquired indentation data using a counter-balance beam with load applied directly to the tissue surface via 20mm plane-ended indenter (assumed to be cylindrical). Indentation tests were conducted on the anterior forearm resting on a fixed base. Data was collected from two subject groups: healthy 20-26 year olds and healthy or hospitalized 57-79 year olds.

Tissue deformation was tracked using a potentiometric linear displacement transducer. Skin thickness was measured using Harpenden skinfold calipers. A constant load was applied for two minutes and the tissue was allowed to recover for two minutes for three cycles.

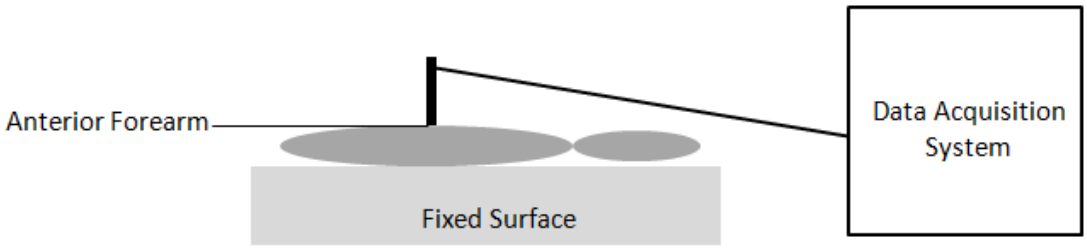

Figure 57. Experimental test set up developed by Bader *et al.* for *in vivo* compression testing of human skin. The load was applied via a 20mm plane-ended indenter to the anterior aspect of the forearm in a fixed position.

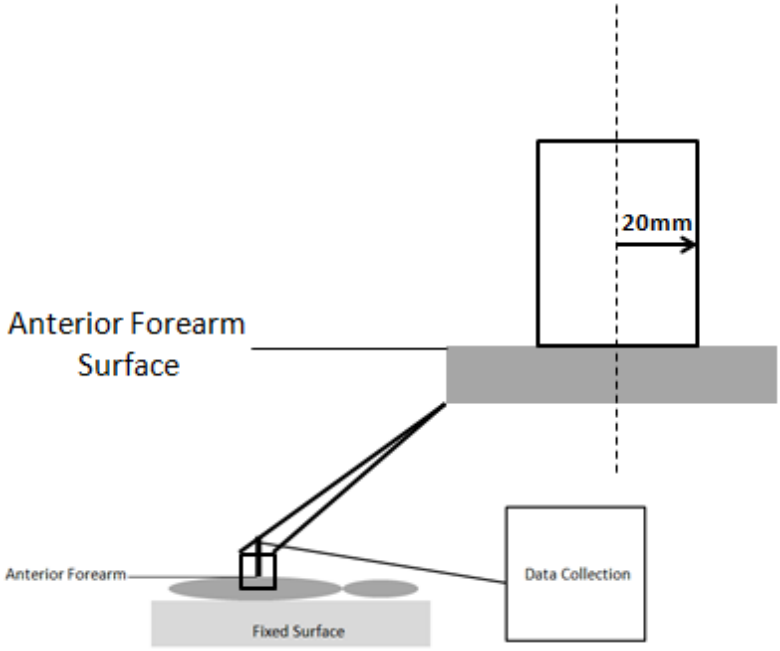

Figure 58. Experimental test set up developed by Bader *et al.* for *in vivo* compression testing of human skin. The load was applied via a 20mm plane-ended indenter to the anterior aspect of the forearm in a fixed position.

Appendix B. Procedure for Gaussian Curve Fit

A Gaussian distribution was used to model the strain profile of skin indentation under both axisymmetric spherical and cylindrical plane strain loading conditions. The general form of a Gaussian distribution strain profile is defined by

$$\varepsilon = -\gamma e^{\frac{-(x-\mu)^2}{2\sigma^2}} \tag{A.1}$$

where γ is the maximum strain at x = 0, μ is the mean, and σ is the is the standard deviation (spread). For an axisymmetric model, $\mu = 0$. Therefore, the only parameter requiring calibration is σ, the spread.

Both loading conditions can be geometrically modeled as the arc of a circular segment (Figure 59).

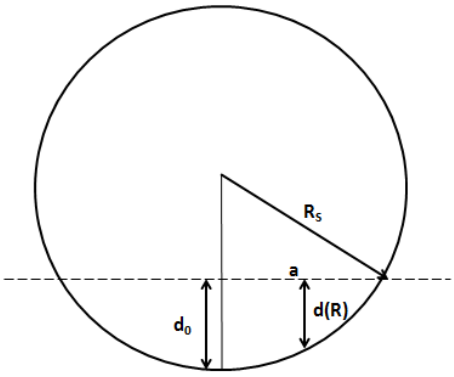

Figure 59. The geometric relationships between sphere radius (R_s), contact radius (a), and maximum indentation (d_o) are used to develop the geometric circular segment strain profile function.

The strain profile of the arc of a circular segment is defined by

$$\varepsilon_z = -\frac{d(R)}{H} \tag{A.2}$$

where H is the tissue thickness and

$$d(R) = \sqrt{R_S^2 - R^2} - \sqrt{R_S^2 - a^2} \tag{A.3}$$

$$a^2 = R_S^2 - (R_s - d_0)^2 \quad \text{(A.4)}$$

$$d_0 = d(R = 0). \quad \text{(A.5)}$$

With a geometrical representation of the strain profile known, a curve fit of the Gaussian distribution via parameter estimation of the spread (σ) provides a method of developing a Gaussian strain distribution.

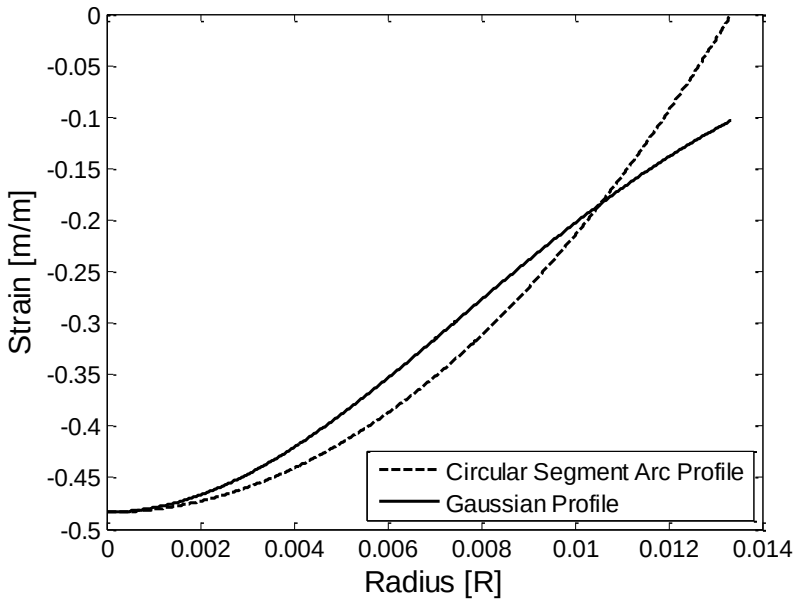

Figure 60. Representative plot demonstrating the output of a curve fit between the geometric circular segment strain profile and Gaussian strain profile via parameter estimation of the spread (σ). This particular strain profile modeled a neonatal occipital PrU and resulted in σ=0.0076.

Appendix C. Derivation of Circular Segment Strain Profile

The arc of a circular segment was used to model the strain profile of skin indentation under both axisymmetric spherical and cylindrical plane strain loading conditions. The general form of a circular segment strain profile is defined by

$$\varepsilon_z = -\frac{d(R)}{H} \tag{C.1}$$

where *d(R)* is the tissue displacement as a function of radius and *H* is the tissue thickness. The tissue displacement, *d(R)*, was derived from basic geometrical relationships for the arc of a circular segment (Figure 61).

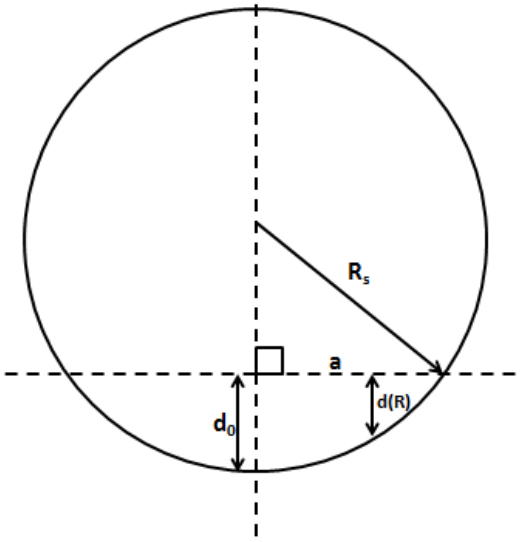

Figure 61. The tissue displacement, *d(R)*, was derived as a function of the contact radius, *a*, from the basic geometrical relationships governing the arc of a circular segment.

The maximum tissue deformation was defined as $d_0 = d$ when R = 0 and the contact radius, *a*, is determined using the Pythagorean Theorem, such that

$$a^2 = R_S^2 - (R_s - d_0)^2 \tag{C.2}$$

The tissue displacement as a function of radius, *R*, and contact radius, *a*, is defined by

$$d(R) = y - (R_s - d_0) \tag{C.3}$$

where $(R_s - d_0) = \sqrt{R_S^2 - a^2}$ from Equation (C.2) and $y = \sqrt{R_S^2 - R^2}$ (Figure 62) such that the final form of the tissue displacement is determined by

$$d(R) = \sqrt{R_S^2 - R^2} - \sqrt{R_S^2 - a^2} \tag{C.4}$$

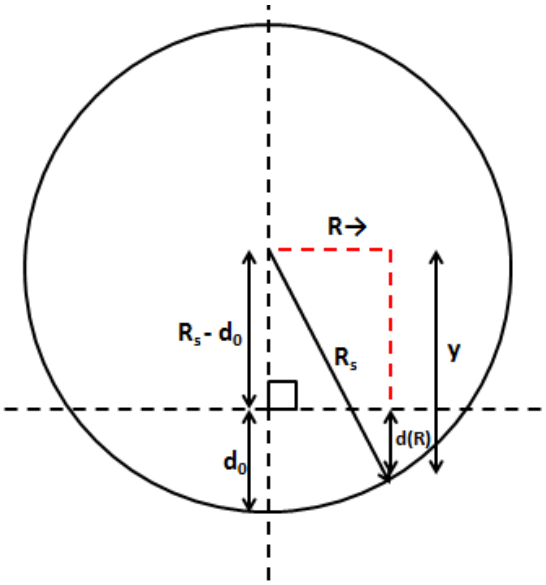

Figure 62. The tissue displacement, *d(R)*, was derived as a function of the contact radius, *a*, from the basic geometrical relationships governing the arc of a circular segment. The Pythagorean Theorem is utilized on the highlighted triangle to determine the length *y*, which is then used to determine the final function for *d(R)*.

VITA

VITA

Anne Zakrajsek joined the Human Injury Research and Regenerative Technologies (HIRRT) laboratory at Purdue University in 2008 to participate in undergraduate research. Her research focused on the development of an intramedullary rod for forearm fracture fixation in conjunction with Dr. Greg Merrell at the Indianapolis Hand Center. Her senior design project, advised by the HIRRT lab, involved the design of a novel therapeutic method for pressure ulcer prevention. This project won the first place Malott Innovation Award and resulted in a patent (Therapeutic method and apparatus using mechanically induced vibration US 8764688 B1). Anne continued in the HIRRT lab to pursue graduate studies in 2010. Her master's project focused on the design and development of a novel padding material intended for use in football helmets in conjunction with a translational research project funded by the Alfred E. Mann Institute for Biomedical Engineering. This work resulted in three pending patent applications and one co-authored peer-reviewed journal article. Maintaining her passion for design, her doctoral work developed an analytical model of skin tissue *in vivo* for use in optimizing the design criteria of the therapeutic method developed during undergraduate senior design. She is currently working with Adapt-IF Technologies, a start-up non-profit organization that designs and delivers custom assistive technology devices.